Identification and Modeling of the Dynamic Behavior of the Direct Path Component in ToA-Based Indoor Localization Systems

A Dissertation

Submitted to the Faculty

of the

WORCESTER POLYTECHNIC INSTITUTE

in partial fulfillment of the requirements for the

Degree of Doctor of Philosophy

in

Department of Electrical and Computer Engineering

by

Mohammad Heidari

May 2008

APPROVED:

Prof. Kaveh Pahlavan, Advisor	Prof. Allen H. Levesque, ECE Dept.
Prof. Berk Sunar, ECE Dept.	Dr. Bardia Alavi, Committee Member

Prof. Fred J. Looft, Head, ECE Dept.

To my Wife

Acknowledgements

I am greatly thankful and indebted to Professor Kaveh Pahlavan, not only for his guidance and support in academics and research but also for enlightening me with true philosophy of life. He has endowed me with the insight, wisdom, and righteousness through his short didactic stories which are life lessons to be revived. My work and accomplishments were only possible because of his help and encouragement. Simply, He has been more than an advisor to me.

I would also like to thank my dissertation committee members, Professor Fred Looft, Professor Allen Levesque, Professor Berk Sunar, and Dr. Bardia Alavi for their invaluable comments and suggestions.

I am also very grateful to my fellow WPI friends, Dr. Bardia Alavi, Dr. Nayef Ali Alsindi, and Mr. Hamid Ghadyani for their continuous help, support, friendship, and splendid working atmosphere they provided.

I would also thank the Draper Laboratories and WPI Institute Fellowship and Assistantship for funding my research.

Simply, I could not have reached where I am today without my father, Mr. Ahmad Heidari, my mother, Mrs. Vahedeh Houshivar, my sister, Mrs. Hannaneh Heidari, and my brother Mr. Hamed Heidari. To them I dedicate this work. And ... Words can not express my gratitude to my wife, Mrs. Elahe Rastgoo, whose love and sacrifice is the source of my motivation to continue.

Abstract

A well-known challenge in estimating the distance of the antenna pair in time-of-arrival (ToA) based RF localization systems is the problem of obstruction of the direct path (DP) between transmitter and receiver. The absence of DP component in received channel profile creates undetected direct path (UDP) conditions. UDP condition, in turn, will cause occurrence of unexpected large ranging errors which pose serious challenge to precise indoor localization. Analysis of the behavior of the ranging error in such conditions is essential for the design of precise ToA-based indoor localization systems. This dissertation discusses two open problems in ToA-based indoor localization systems.

The first contribution of this dissertation discusses the problem of modeling of dynamic behavior of ranging error. We propose a novel analytical framework for analysis of dynamic spatial variations of ranging error observed by a mobile user based on an application of Markov chain. The model relegates the behavior of ranging error into four main categories associated with four states of Markov process. Parameters of distributions of ranging error in each Markov state are extracted from empirical data collected from a measurement-calibrated ray tracing algorithm simulating a typical office environment. The analytical derivation of parameters of the Markov model employs the existing path-loss models for first detected path and total multipath received power in the same office environment. Results of simulated errors from the Markov model and actual errors from empirical data show close agreement.

The second contribution of this dissertation discusses the problem of identification of UDP condition given an unknown channel profile. Existing of UDP condition in a channel profile poses serious degradation to ranging estimate process. Therefore, identification of occurrence of UDP condition is of our subsequent concern. After identification, the second step is to mitigate ranging errors in such conditions. In this dissertation we present two methodologies, based on binary hypothesis testing and an application of artificial neural network design, to identify UDP conditions and mitigate ranging error using statistics extracted from wideband frequency-domain indoor measurements conducted in typical office building.

Contents

Nomenclature **xix**

1 Introduction **1**

1.1 Background 1

1.2 General Description 4

1.3 Motivation of the Research 10

1.4 Main Contributions of the Dissertation 12

1.5 Outline of the Dissertation 14

2 Measurement and Simulation Databases **15**

2.1 Ray Tracing Simulation Database 16

2.1.1 Introduction to Ray Tracing 16

2.1.2 RT Simulation Scenario 18

2.2 Wideband Measurement Database 21

2.2.1 Measurement System 21

2.2.2 Measurement Scenario 25

2.3 Comparison of Ray Tracing Simulation and Empirical Wideband Measurement 26

2.3.1 Effects of Architectural Micro-Metals 31

2.3.2 Effects of Scattered Micro-metals 35

2.3.3 Closeness of RT and Measurement Channel Profiles 36

3 Receiver Location Classification for Modeling the Behavior of Direct Path 44

3.1 Four Classes of Receiver Locations 45

3.2 Ranging error classification based on power 48

3.3 Ranging Error Classification Based on Distance 52

3.3.1 Infrastructure-distance-measurement-based model (IDM) . . . 53

3.4 Statistical Behavior of Ranging Error in Each Class 56

3.4.1 Improvement over IEEE 802.15.3 recommended model 62

4 Modeling of the Dynamic Behavior of Direct Path 64

4.1 Dynamic Modeling of the Behavior of Class of Receiver Location using Markov Chain 65

4.1.1 Ranging states of the Markov model 65

4.1.2 Average transition probabilities 67

4.1.3 Exponential modeling of dwell time 70

4.1.4 Multivariate distribution modeling of the state probabilities . 71

4.2 Modeling of the Spatial Characteristics of Ranging Error within a State using Autocorrelation Properties 73

4.3 Simulation and Results 75

4.3.1 Markov model representation 76

4.3.1.1 Parameters of the Markov Chain 77

4.3.1.2 Ranging error statistics 79

4.3.2 Modeling and analysis of state probabilities 82

5 Binary Hypothesis Testing for UDP Identification 84

5.1 Indoor Localization 85

5.1.1 Least Square Solution to Indoor Localization Problem 86
5.1.2 Time Metrics 89
5.1.2.1 Mean Excess Delay 89
5.1.2.2 RMS Delay Spread 92
5.1.3 Power Metrics 94
5.1.4 Hybrid Time/Power metric 98
5.2 Binary Hypothesis Testing for UDP Identification 102
5.3 Simulations and Results of Localization using ToA measurements . . 106
5.3.1 Simulations 106
5.3.2 Measurements 108

6 Neural Network Architecture for UDP Identification 111
6.1 Neural Network Architecture 112
6.1.1 NNA Parameters 116
6.1.2 Generalization of the Network 118
6.2 Simulation and Results of Localization using ToA measurement . . . 119
6.2.1 Localization Scenario and Effects of Mitigation 119

7 Conclusions and Future Work 125
7.1 Contributions 125
7.1.1 Modeling the Dynamic Behavior of the Direct Path Component 125
7.1.2 UDP Identification 126
7.1.3 Other Contributions 127
7.2 Future Research Directions 127
7.2.1 Comprehensive Dynamic Model for MPCs 128
7.2.2 UDP Identification Generalization 128

A Ray Tracing and Measurement Channel Profile Comparison - Original Floor Plan 129

B Ray Tracing and Measurement Channel Profile Comparison - Modified Floor Plan 135

C Ray Tracing and Measurement Channel Profile Comparison - UWB Measurement 141

References 159

List of Figures

1.1 Basic block diagram of a positioning system 5

1.2 Sample channel profile for a DDP class. Small shift of the detected path to the direct path represents the ranging error 7

1.3 Sample channel profile exhibiting UDP conditions. In such scenarios the large difference between the first detected path and the direct path causes the performance of the localization system to degrade drastically. 8

1.4 Sample channel profile exhibiting UDP conditions 11

2.1 A sample snapshot of the CWINS internal ray tracing software - PlaceTool 18

2.2 Sample snapshot of the CIR of the output of the ray tracing software 19

2.3 Floor plan of the third floor $AKLabs$, WPI - The details of the floor plan include two metallic shafts, all the metallic doors, and several metallic shelves located in the vicinity of the transmitters 19

2.4 Grid representation of all the receiver locations and three transmitter locations - The locations of the transmitter were chosen carefully to generate variety of channel profiles 20

2.5 Measurement System 21

2.6 Block Diagram of the Measurement System 22

2.7 (a) Sample frequency domain measurement from network analyzer - absolute value of the received frequency domain measurement and (b) Corresponding time domain channel profile obtained by the Chirp-Z transformation 24

2.8 Floor plan of the third floor of the *AKLabs* used for conducting wideband measurements - The locations of the metallic shafts are pointed out in the floor plan 25

2.9 Walking route in the same scenario for three different access points - It can be observed that metallic shafts cause instant SUDP for two transmitters 26

2.10 First scenario for comparison of measurement and RT - with emphasis on the effects of metallic objects on ToA measurements 27

2.11 (a) Comparison of channel profiles obtained from measurement and RT software for the metallic door scenario and (b) Comparison of the measurement channel profiles and RT channel profile for the metallic chamber scenario 29

2.12 Comparison of the results of RT versus the channel measurements for the door scenario 30

2.13 Comparison of the results of the RT versus the channel measurements for the chamber scenario 31

2.14 Corridor scenario for comparing the results of RT and measurement channel profiles and their respective ToA measurements 32

2.15 Comparison of measurement and RT channel profiles for the first point in corridor scenario 33

2.16 Comparison of the ranging estimate obtained from measurement and RT channel profiles 33

2.17 Modifications to the original floor plan to include the metallic details of the building 34

2.18 Comparison of the ranging estimate obtained from measurement and RT channel profiles after modifications to the original floor plan of the building under study 35

2.19 Scattered metallic object in the vicinity of the transmitter location . 37

2.20 Comparison of ToA ranging error for measurement channel profiles and channel profiles obtained from RT with the original floor plan which excluded micro-metallic objects and included only two metallic shafts 38

2.21 Comparison of total power of the channel profile for measurement channel profiles and channel profiles obtained from RT with the original floor plan which excluded micro-metallic objects and included only two metallic shafts 38

2.22 Comparison of ToA ranging error for measurement channel profiles and channel profiles obtained from RT with the modified floor plan which included limited micro-metallic objects 39

2.23 (a) Comparison of channel profiles obtained from measurement and RT software for the metallic door scenario and (b) Comparison of the measurement channel profiles and RT channel profile for the metallic chamber scenario 41

2.24 Comparison of ToA range estimate for measurement channel profiles and channel profiles obtained from RT with the modified floor plan which inclusion of metallic details of the building 42

2.25 Comparison of ToA ranging error for measurement channel profiles and channel profiles obtained from RT with the original floor plan which excluded micro-metallic objects and included only two metallic shafts 43

3.1 Classification of UDP conditions, a) A NUDP scenario which avoided obstruction by macro metallic objects and b) SUDP scenario in which a metallic chamber obstructs majority of the receiver locations and creates UDP conditions as the receiver moves along the corridor . . . 47

3.2 Receiver location classification 48

3.3 Indoor receiver classification simulation for a sample location of the transmitter. The location of the metallic chamber close to the transmitter causes lots of SUDP receiver locations. 52

3.4 Indoor receiver classification for the same location of the transmitter based on infrastructure-distance-measurement (IDM) model. The pattern of the areas associated with each class is very similar to those obtained from power based classification 54

3.5 Distribution modeling of the ranging error with normal distribution for a) DDP class of receiver locations and b) NUDP class of receiver locations 58

3.6 Statistical analysis of ranging error observed in SUDP class of receiver location, a) Histogram of ranging error and b) Probability plot of ranging error vs. different distributions. It can be concluded that GEV distribution best models the ranging error observed in such class of receiver location 61

4.1 Markov model presented for dynamic behavior of the ranging error in indoor localization . . . 66
4.2 Crossing rate a random mobile client from one Markov state to another Markov state . . . 68
4.3 ACF of SUDP ranging error for the *random walk* scenario . . . 74
4.4 Dwell time distribution of mobile terminal in SUDP state . . . 79
4.5 Distributions of dwell time for a random mobile terminal in DDP and NUDP states . . . 80
4.6 Comparison of ranging error observed by a mobile user with simulation 82
4.7 Comparison of the CDF of the state probabilities for different states with their respective normal fit . . . 83

5.1 Normality of τ_m for DDP and UDP profiles - Probability plot preview 90
5.2 Normality of τ_m for DDP and UDP profiles - Distribution preview . . 91
5.3 Normality of τ_{rms} for DDP and UDP profiles - Probability plot preview 93
5.4 Weibull distribution modeling of total power for RT database - Probability plot preview . . . 95
5.5 Weibull distribution modeling of power loss for RT database - Distribution preview . . . 96
5.6 Weibull distribution modeling of total power . . . 97
5.7 Weibull distribution modeling of hybrid metric . . . 99
5.8 Weibullity of ξ_{hyb} for DDP and UDP profiles - Distribution preview . 100
5.9 Weibull distribution modeling of hybrid metric . . . 101
5.10 Localization error in sample indoor environment - Simulation . . . 107
5.11 CDF of localization error for sample indoor environment - Simulation 108
5.12 Localization error in sample indoor environment - Measurements . . . 109

5.13 CDF of localization error for sample indoor environment - Measurements 110

6.1 Basic schematic of the artificial neural network used in this study. For training, the network is fed with the extracted RMS delay spread, total power, and hybrid metric of the channel profile as inputs as well as UDP identification flag as output. The process os repeated for few receiver location. Once NNA is trained, the extracted metric of an unknown channel profile is fed to the network and networks simulates the respective output. The process is repeated for all of the transmitters, individually but simultaneously 113

6.2 Accuracy of UDP identification as a function of number of training points used to train the NNA 117

6.3 Localization error in sample indoor environment for two RPs 120

6.4 CDF of localization error for the sample indoor environment for two RPs 122

6.5 Localization error in sample indoor environment for three RPs 122

6.6 CDF of localization error for the sample indoor environment for three RPs 124

A.1 Comparison of the channel profiles obtained from measurement and RT - Original floor plan without adjustments of the door and metallic shelf - Point 1 129

A.2 Comparison of the channel profiles obtained from measurement and RT - Original floor plan without adjustments of the door and metallic shelf - Point 2 130

A.3 Comparison of the channel profiles obtained from measurement and RT - Original floor plan without adjustments of the door and metallic shelf - Point 3 130
A.4 Comparison of the channel profiles obtained from measurement and RT - Original floor plan without adjustments of the door and metallic shelf - Point 4 131
A.5 Comparison of the channel profiles obtained from measurement and RT - Original floor plan without adjustments of the door and metallic shelf - Point 5 131
A.6 Comparison of the channel profiles obtained from measurement and RT - Original floor plan without adjustments of the door and metallic shelf - Point 6 132
A.7 Comparison of the channel profiles obtained from measurement and RT - Original floor plan without adjustments of the door and metallic shelf - Point 7 132
A.8 Comparison of the channel profiles obtained from measurement and RT - Original floor plan without adjustments of the door and metallic shelf - Point 8 133
A.9 Comparison of the channel profiles obtained from measurement and RT - Original floor plan without adjustments of the door and metallic shelf - Point 9 133
A.10 Comparison of the channel profiles obtained from measurement and RT - Original floor plan without adjustments of the door and metallic shelf - Point 10 134

B.1 Comparison of the channel profiles obtained from measurement and RT - Revised floor plan with adjustments of the door and metallic shelf - Point 1 135
B.2 Comparison of the channel profiles obtained from measurement and RT - Revised floor plan with adjustments of the door and metallic shelf - Point 2 136
B.3 Comparison of the channel profiles obtained from measurement and RT - Revised floor plan with adjustments of the door and metallic shelf - Point 3 136
B.4 Comparison of the channel profiles obtained from measurement and RT - Revised floor plan with adjustments of the door and metallic shelf - Point 4 137
B.5 Comparison of the channel profiles obtained from measurement and RT - Revised floor plan with adjustments of the door and metallic shelf - Point 5 137
B.6 Comparison of the channel profiles obtained from measurement and RT - Revised floor plan with adjustments of the door and metallic shelf - Point 6 138
B.7 Comparison of the channel profiles obtained from measurement and RT - Revised floor plan with adjustments of the door and metallic shelf - Point 7 138
B.8 Comparison of the channel profiles obtained from measurement and RT - Revised floor plan with adjustments of the door and metallic shelf - Point 8 139

B.9 Comparison of the channel profiles obtained from measurement and RT - Revised floor plan with adjustments of the door and metallic shelf - Point 9 139

B.10 Comparison of the channel profiles obtained from measurement and RT - Revised floor plan with adjustments of the door and metallic shelf - Point 10 140

C.1 Comparison of the channel profiles obtained from UWB measurement and RT - Revised floor plan with adjustments of the door and metallic shelf - Point 1 141

C.2 Comparison of the channel profiles obtained from UWB measurement and RT - Revised floor plan with adjustments of the door and metallic shelf - Point 2 142

C.3 Comparison of the channel profiles obtained from UWB measurement and RT - Revised floor plan with adjustments of the door and metallic shelf - Point 3 142

C.4 Comparison of the channel profiles obtained from UWB measurement and RT - Revised floor plan with adjustments of the door and metallic shelf - Point 4 143

C.5 Comparison of the channel profiles obtained from UWB measurement and RT - Revised floor plan with adjustments of the door and metallic shelf - Point 5 143

C.6 Comparison of the channel profiles obtained from UWB measurement and RT - Revised floor plan with adjustments of the door and metallic shelf - Point 6 144

C.7 Comparison of the channel profiles obtained from UWB measurement and RT - Revised floor plan with adjustments of the door and metallic shelf - Point 7 144

C.8 Comparison of the channel profiles obtained from UWB measurement and RT - Revised floor plan with adjustments of the door and metallic shelf - Point 8 145

C.9 Comparison of the channel profiles obtained from UWB measurement and RT - Revised floor plan with adjustments of the door and metallic shelf - Point 9 145

C.10 Comparison of the channel profiles obtained from UWB measurement and RT - Revised floor plan with adjustments of the door and metallic shelf - Point 10 146

List of Tables

3.1 Parameters of Normal Distribution Ranging Error of DDP and NUDP Classes 57

3.2 Passing Rate of $K-S$ and Statistical Value of χ^2 Hypothesis Tests at 5% Significance Level Ranging Error for SUDP Class 59

3.3 Parameter of GEV Distribution Ranging Error of SUDP Class 62

5.1 The mean and standard deviation of the normal distribution for the τ_m 91

5.2 The mean and standard deviation of the normal distribution for the τ_{rms} 94

5.3 The a and b parameters of the Weibull distribution for the $-P_{tot} = r$ 96

5.4 The a and b parameters of the Weibull distribution for the $-P_{tot} = r$ 98

5.5 The ϑ and κ parameters of the Weibull distribution for the ξ_{hyb} . . . 100

5.6 The ϑ and κ parameters of the Weibull distribution for the ξ_{hyb} . . . 102

5.7 Accuracy of the Likelihood Hypothesis Test using RT channel profiles 104

5.8 Accuracy of the Likelihood Hypothesis Test using Measurement Channel Profiles 105

6.1 Accuracy of UDP Identification using Likelihood Hypothesis Tests and Neural Network Architecture 115

6.2 Generalization of UDP Identification 118

Nomenclature

Roman Symbols

A	choleski decomposition
$a_{RT,meas}$	scale parameter of the Weibull distribution for total power
B	homogeneous continuous Markov process
b_i	neural network biases
$b_{RT,meas}$	shape parameter of the Weibull distribution for total power
c	electromagnetic wave propagation speed
d	distance
e	eigenvector values
f	distribution function
F	cumulative distribution function
$\mathbf{G}(\mathbf{x})$	Hessian matrix
$G_{1,2}$	NNA transfer functions
$\mathbf{g}(\mathbf{x})$	gradient
g	hidden layer function of neural network
$\mathcal{GEV}$	generalized extreme value distribution)
h	channel impulse response and channel profile
H	binary hypothesis
$\mathbf{H}$	approximation to the inverse of Hessian
i	target of NNA
L	likelihood function
l	boundary length
$\mathcal{MC}$	Markov chain
$\mathcal{N}$	normal (Gaussian) distribution
o	output of NNA
$\mathbf{p}$	state probability random variable
$p_{i,j}$	average transition probability from state i to state j
$\bar{\mathbf{P}}$	average transition probabilities matrix
P_r	probability
P_{DP}	power of the direct path component
P_{tot}	total power of the channel profile

Q	number of training sequence in the NNA cost function
r	power loss
R_x	receiver location
s	pulse shape
S	area of each state
t	time
T	time difference
$\mathfrak{T}$	cluster arrival rate
T_x	Transmitter location
v	velocity of the mobile terminal
X	shadow fading
x	x-coordination of the antenna
$\mathbf{x}$	vector of coordinations of the antenna
y	y-coordination of the antenna
$z \in Z$	complete set of receiver location classes

Greek Symbols

α	path amplitude
α_c	crossing rate
ϕ	path phase
τ	path delay
ε	ranging error
λ	blockage identification flag
η	detection and decision threshold
ξ	class of receiver location - class of ranging error
$\mu_{DDP,NUDP}$	mean of normal distribution for DDP and NUDP classes
$\mu_{m,rms}$	mean of normal distribution for τ_m and τ_{rms}
$\sigma_{DDP,NUDP}$	standard deviation of normal distribution for DDP and NUDP classes
$\sigma_{m,rms}$	standard deviation of normal distribution for τ_m and τ_{rms}
μ_{SUDP}	location parameter of the GEV distribution for SUDP class
κ_{SUDP}	shape parameter of the GEV distribution for SUDP class
σ_{SUDP}	scale parameter of the GEV distribution for SUDP class
θ	ray arrival rate parameter
Θ	cluster arrival rate parameter
ω	instant class of receiver location
Ω	Markov chain - sequence of instant classes
π	initial state PDF
Δ	Grid size
β	Markov parameter
$\boldsymbol{\upsilon}$	eigenvector
γ	exponential parameter of dwell time of Markov chain
ψ	Chapman-Kolmogorov solution
$\boldsymbol{\mu}$	mean vector of state probabilities

$\mathbf{\Sigma}$	covariance matrix of state probabilities
ϖ	autocorrelation function parameter
ρ	tolerance
τ_m	mean excess delay
τ_{rms}	RMS delay spread
χ^2	chi-square hypothesis test
$\kappa_{RT,meas}$	shape parameter of the Weibull distribution of the hybrid metric
$\vartheta_{RT,meas}$	scale parameter of the Weibull distribution of the hybrid metric
Λ	likelihood ratio function
δ	output function of neuran network for UDP identification
ω_i	neural network wights
γ	performance ratio in NNA
Superscripts	
d	DDP superscript
u	UDP superscript
Subscripts	
RT	RT subscript
$meas$	meas subscript
Acronyms	
ACF	AutoCorrelation Function
$AKLabs$	Atwater Kent Laboratories
AoA	Angel of Arrival
BN	Background Noise
CDF	Cumulative Distribution Function
CIR	Channel Impulse Response
$CWINS$	Center for Wireless Information Network Studies
DDP	Detected Direct Path
DP	Direct Path
DR	Dynamic Range
FDP	First Detected Peak
GPS	Global Positioning System
HMM	Hidden Markov Model
IDM	Infrastructure-Distance-Measurement model
IFT	Inverse Fourier Transform
$K-S$	Kolmogorov-Smirnov hypothesis test
LNA	Low Noise Amplifier
LoS	Line of Sight
MND	Multivariate Normal Distribution
MSE	Mean Square Error
$MSEreg$	Regularized Mean Square Error
NC	No Coverage
$NLoS$	Non Line of Sight

NNA	Neural Network Architecture
$NUDP$	Natural Undetected Direct Path
PDF	Probability Distribution Function
$RFID$	Radio Frequency IDentification
RMS	Root Mean Square
RSS	Received Signal Strength
RT	Ray Tracing
SP	Strongest Path
SSE	Sum Square Error
$SUDP$	Shadowed Undetected Direct Path
$TDoA$	Time Difference of Arrival
ToA	Time of Arrival
UDP	Undetected Direct Path
UWB	Ultra-Wide Bandwidth
WPI	Worcester Polytechnic Institute
WSN	Wireless Sensor Network

Chapter 1

Introduction

1.1 Background

Localization using radio signals has attracted increasing attention in the field of tracking and navigation. The first research to address this difficult problem on a worldwide scale resulted in launching a series of satellites for the global positioning system (GPS) [Kap96]. Although widely used today for personal and commercial outdoor applications, it is recognized that GPS does not perform satisfactorily in dense urban and indoor environments which has sparked interest among researchers and practitioners in focusing their efforts on indoor localization systems [Ded05].

With the advancements in signal processing and channel measurements, the indoor localization concept has paved the way for a variety of applications in commercial, health care, public safety, and military domains. In commercial applications, localization has been instrumental in supply-chain and asset management in warehouses. In the health care domain, there are important uses for tracking/locating patients, medications, and instruments in hospitals, as well as tracking people with special needs; such as tracking elderly individuals or individuals with special needs.

In the public safety and military domains, precise localization is of utmost importance to assist fire-fighters and military personnel in accomplishing their missions [Say98, McK05].

Precise indoor localization is also an important part of various personal robotics applications [Jen01] as well as in the more general category of context-aware computing [War97]. More recently, location sensing has found applications in location-based handoffs in wireless networks [Pah00], location-based ad-hoc network routing [Ko98, Jai01] and location-based authentication, as well as security, privacy [Sma02], and radio frequency identification (RFID) assisted localization [Hah04]. These and other applications have stimulated interest in modeling the propagation environment to assess the accuracy of different sensing techniques [Pah98, Kri99], as well as in developing novel technologies to implement the systems [Fon01, Bah00b, Bah00a]. We have already seen implementation of the first generation of indoor positioning products using a variety of technologies [Wer98, Roo02a, Roo02b], the more accurate second generation of products demands extensive research in understanding and modeling of the channel behavior caused by intensive multipath and other sources of error in indoor areas. These models are necessary for the design of meaningful algorithms to remedy the effects of extensive multipath and blockage of the multipath components [Che99, Ala06b], which causes large ranging error in their respective system [Ala06a].

Estimating the location of an individual or an object in an indoor environment can be a difficult task, often producing ambiguous results, due to the harsh wireless propagation environment in most such areas. The indoor radio propagation channel is characterized as site-specific, exhibiting severe multipath and low probability of line of sight (LoS) signal propagation between the transmitter and receiver [Pah05], making accurate indoor localization very challenging and necessitating novel ap-

proaches in their respective model design.

Recently, potential technologies emerged to deal with these indoor challenges, including ultra-wideband (UWB) systems [Mol06, Gez05, Fal06] and wireless sensor networks (WSNs) [Pah06, Ryd06, Mos03, Pat03]. In the former, enhancements in ranging accuracy through the availability of excess system bandwidth makes it possible to resolve the multipath components effectively, thus combating multipath error [Ala06a, Tar06]. The latter approach takes advantage of redundant range measurements between the sensor nodes to further improve the accuracy. Nevertheless, these technologies still suffer in the face of undetected direct path (UDP) condition, which is the major restriction to accurate indoor localization.

Localization techniques, in general, utilize metrics of the received radio signals. Traditional metrics for localization applications are angle of arrival (AoA), received signal strength(RSS), time of arrival (ToA), and time difference of arrival (TDoA). Localization using AoA and TDoA requires complicated and expensive antenna design and synchronization with limited accuracy which makes them unacceptable for use in indoor localization systems. RSS, on the other hand, is a simple metric that can be measured and it is measured and reported by most wireless devices. It uses the existing infrastructure of the wireless networks in indoor environment and hence is inexpensive to install. The two fundamental approaches in using RSS metric for localization purposes are distance estimation and fingerprinting.

In distance estimation the distance of the antenna pair is estimated by using the power-distance relationship. This method, however, results in very unreliable distance estimation and has restricted accuracy. In fingerprinting methods, an off-line phase is first performed based on storing the measured power from different access points for different receiver locations. This is followed by an on-line phase based on matching the new power measurement with elements of the database. It can

be shown that even fingerprinting methods using RSS metric have limited accuracy. ToA of the direct signal between the transmitter and receiver, when available, yields a very accurate estimate of the distance of the antenna pair, making ToA-based localization systems a prudent choice among alternative systems. However, at some receiver locations the direct signal between the transmitter and receiver is either blocked or shifted due to blockage and multipath, necessitating novel approaches to detect those conditions and remedy their respective estimated distances. The work of this dissertation is focused on the behavior of the direct signal and its respective ToA in indoor environments.

1.2 General Description

The rich multipath indoor channel environment is characterized by an impulse response

$$h_{\infty}(t) = X \sum_{l=1}^{L} \sum_{k=1}^{K} \alpha_{k,l} e^{j\phi_{k,l}} \delta(t - \mathcal{T}_l - \tau_{k,l}) \tag{1.1}$$

where $\mathcal{T}_l$ represents the delay of the l^{th} cluster, $\{\alpha_{k,l}\}$, $\{\phi_{k,l}\}$, and $\{\tau_{k,l}\}$ represent the tap weight, phase, and delay of the k^{th} multipath component relative to the l^{th} cluster arrival time, $(\mathcal{T}_l)$, respectively, and X represents the log-normal shadowing [Mol03, Cas02]. The tap weights, $\{\alpha_{k,l}\}$, are determined based on practical path-loss exponents and signal loss of different building materials for reflection and transmission mechanisms in indoor environment [Pah05]. The channel impulse response (CIR) then consists of $\{\alpha_{k,l}\}$s which are within the dynamic range of the system.

The basic concept of a positioning system is illustrated in Fig. 1.1. The location sensing devices measure the distance-related metrics between the mobile client, i.e. receiver and a fixed RP, such as ToA, AoA, RSS, and TDoA. The positioning al-

gorithm processes the reported metrics to estimate the location coordinates of the receiver. The display system exhibits the location of the mobile terminal relative to the user. The accuracy of location estimation is a function of the accuracy of location metrics and the complexity of the positioning algorithm [Pah06].

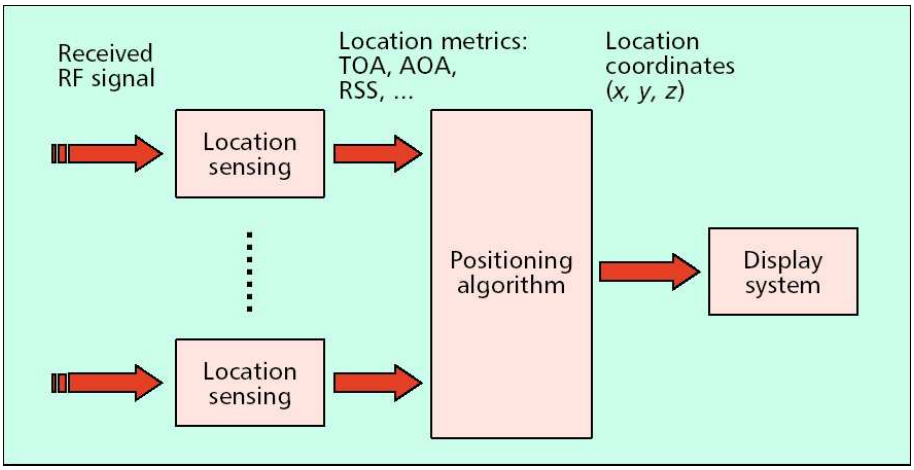

Figure 1.1: Basic block diagram of a positioning system

The ideal CIR is usually referred to as the infinite-bandwidth channel profile since with infinite bandwidth the receiver could theoretically acquire every detectable path. In practice, however, the bandwidth of the system is limited. Filtering the CIR with a limited bandwidth filter results in paths with pulse shapes, the channel profile, which can be represented as

$$h(t) = X \sum_{l=1}^{L} \sum_{k=1}^{K} \alpha_{k,l} e^{j\phi_{k,l}} s(t - \mathcal{T}_l - \tau_{k,l}) \tag{1.2}$$

where $s(.)$ represents the time-domain pulse shape of the filter. In practice, Hanning and raised-cosine filters are widely used today in localization processing. It can be shown that the sufficient bandwidth for accurate indoor localization based on the ToA metric is around 200 MHz [Pah06] for the receiver to be able, with reasonable accuracy, to resolve the multipath and mitigate the ranging error associated with

multipath components.

In ToA-based localization, ToA of the direct path (DP) of the received signal is used to determine the time of flight, τ_{DP}, between the transmitter and the receiver and consequently the distance between the transmitter and the receiver [Kan06].

$$d_{DP} = \tau_{DP} \times c \tag{1.3}$$

where d_{DP} represents the distance of the antenna pair, c represents the speed of electromagnetic waves in free space, and τ_{DP} represents the ToA of the DP.

Applying a peak detection algorithm to the filtered channel profile results in detecting the first detected peak (FDP) and its respective ToA. The ToA of FDP, τ_{FDP}, is then used to approximate the distance of the antenna pair

$$d_{FDP} = \tau_{FDP} \times c \tag{1.4}$$

where d_{FDP} is the estimate of the distance of the antenna pair and τ_{FDP} represents the estimate of the τ_{DP}. The erroneous detection of the DP component results in ranging error, ε_d, which can then be defined as

$$\varepsilon_d = d_{FDP} - d_{DP} \tag{1.5}$$

In the absence of multipath and presence of LoS condition, the estimate of the distance, d_{FDP}, is very close to the true value, d_{DP}, therefore, the error is insignificant. However, in practice there exist three main sources of ranging errors in indoor localization systems. The first source of error is the multipath error which is the shift of FDP from DP due to a combination of bandwidth limitation and presence of rich multipath phenomenon in indoor environments. The ranging error caused by

multipath is inversely proportional to the bandwidth of the measurement system. Indeed in the presence of multipath and of course LoS conditions accurate UWB ToA estimates of the distance are feasible due to their high time domain resolution [Pah06] which allows the ToA-based localization systems to efficiently and properly function under such conditions. However, in the absence of LoS conditions it is possible for UWB systems to suffer large ranging errors depending on the availability of DP. It is worth mentioning that the absence of LoS condition does not necessarily imply that ranging error is bound to be large, as discussed below. Figure 1.2 represents a channel profile under detected direct path (DDP) conditions which illustrates the shift of the FDP from DP because of multipath. The resulting ranging error is shown to be relatively small.

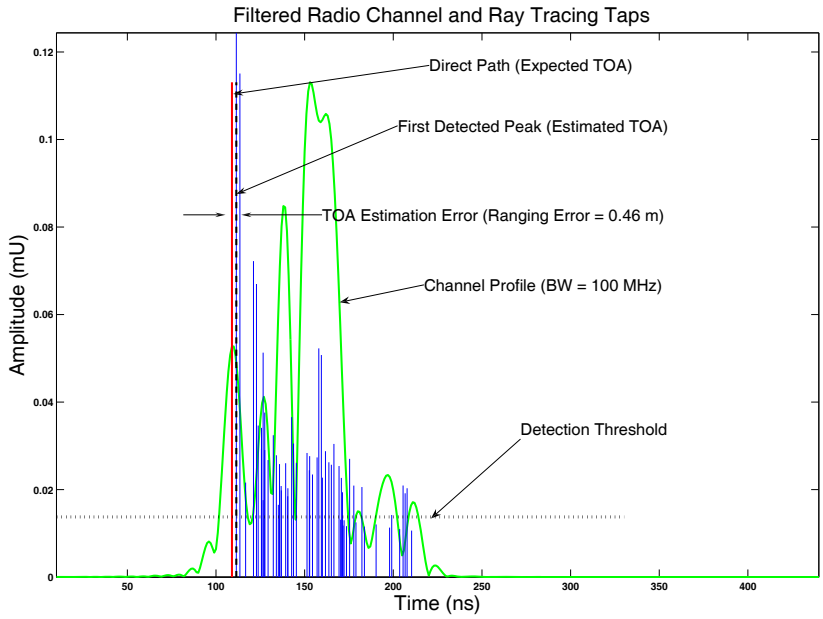

Figure 1.2: Sample channel profile for a DDP class. Small shift of the detected path to the direct path represents the ranging error

The performance of ToA-based localization systems also depends on the availability of DP. Indeed, as mentioned before, in the presence of DP, even in rich mul-

tipath environment, accurate UWB ranging and localization is feasible. However, in non-LoS (NLoS) conditions accurate estimates of the distance of the antenna pair are difficult to obtain. The absence of DP due to blockage is the dominant source of error in such scenarios which is commonly referred to as undetected direct path (UDP) condition. The third source of error is associated with propagation delay and differences of the speed of the radio waves in different media. Figure 1.3 represent a UDP channel profile where it can be observed that FDP is no longer close to DP because of blockage. The resulting ranging error in this case is unexpectedly large.

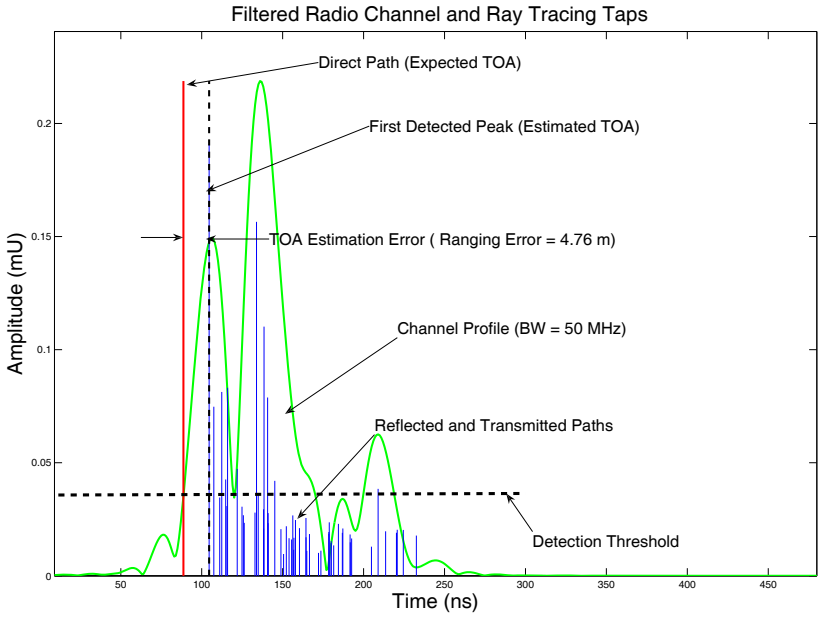

Figure 1.3: Sample channel profile exhibiting UDP conditions. In such scenarios the large difference between the first detected path and the direct path causes the performance of the localization system to degrade drastically.

Previous research classifies the receiver locations into two main classes, DDP and UDP. It is worth mentioning that DDP/UDP classification is a modified version of LoS/NLoS classification. We have also shown that UDP conditions can happen due to different causes and hence can be categorized into different classes as well [Pah06].

The two main classes of UDP consist of natural-UDP (NUDP) and shadowed-UDP (SUDP). SUDP conditions occurs when a large object such as an elevator or a metallic chamber blocks the DP between the transmitter and the receiver. We refer to this first type of UDP condition as shadowed-UDP because the huge metallic object shadows the direct connection between the transmitter and the receiver. Under SUDP conditions, the distance between the transmitter and the receiver could be short, and consequently the total received signal power could be large. The second type of UDP condition, NUDP, occurs in areas of low received power in NLoS environments when due to the large distance between the transmitter and receiver, the power of the DP falls below the detection threshold but there are still other paths arriving with signal strengths above the threshold level. We refer to this class with low received signal power as the natural-UDP condition because it occurs naturally in any indoor area, even in the absence of large metallic objects.

Previous research studies also highlight the fact that in DDP scenarios ranging error is bound to be relatively small as [Ala06a] reports values in the order of $0.1\,m$ ranging error for DDP channel profiles with $100\,MHz$ of bandwidth. Although dependent on the bandwidth of the system, it can be shown that DDP ranging errors follow a normal distribution with zero mean and bandwidth dependent variance. In NUDP class of receiver locations, ranging error is shown to follow normal distribution as well, with a positive mean and larger variance. The average of ranging error in such conditions can be shown to be around $0.5\,m$ for channel profile with $100\,MHz$ of bandwidth. However, SUDP ranging error values are typically large and they do not follow a normal distribution. It can be shown that in an indoor environment even at a short distance of $10\,m$, the localization system can suffer as much as $10\,m$ of ranging error, which drastically degrades the performance of the system.

1.3 Motivation of the Research

Respective channel models addressing the behavior of ToA metric for telecommunication purposes have been developed and are available in the literature. However, these models are aimed primarily at telecommunication applications, while localization applications call for different approaches. In telecommunication applications we are mainly interested in modeling the behavior of the multipath spread of the channel while in ToA-based indoor localization applications we focus on the behavior of the direct path (DP) between the transmitter and the receiver antennas, which identifies the distance between the transmitter and receiver. The difference between the observed ToA of the first path and actual ToA of the DP is referred to as ranging error defined in Eqn. 1.5. The existence of the DP in the received channel profile categorizes the receiver locations into two main classes of DDP and UDP. In DDP scenarios the DP is detectable, resulting in small ranging errors, while in UDP scenarios obstruction of DP generally results in unexpectedly large ranging errors. Therefore, statistical occurrence of the UDP conditions in a typical building is our subsequent concern. As a mobile client travels in an indoor environment, it switches between these two conditions, which imposes drastic changes in ranging error [Pah06].

There are empirical indoor radio propagation channel models available in the literature aiming primarily at telecommunication applications [Sal87, Rap91, Has93b, Has93a]. These models were designed prior to the understanding of the indoor localization problem and hence did not concern the behavior of ranging error in indoor environments. Therefore, they do not provide a close approximation to the empirical observations of the ranging error [Ala06a]. More recently, indoor radio propagation channel models designed for ultra-wide bandwidth (UWB) communications have

paid indirect attention to the indoor localization problem [Mol03, Cas02, Gha04, Gha05] and recent research studies propose UWB measurement system for the design of high-accuracy localization systems [Fal06, Gez05]. However, these indirect models have not paid special attention to occurrence of UDP conditions, which is the main cause of large errors in ranging estimates as illustrated in Fig. 1.4. The first direct empirical model for ranging error is reported in [Ala06b, Ala06a, Den04]. These new direct models, however, do not address the spatial correlation of the ranging error behavior observed by a mobile user.

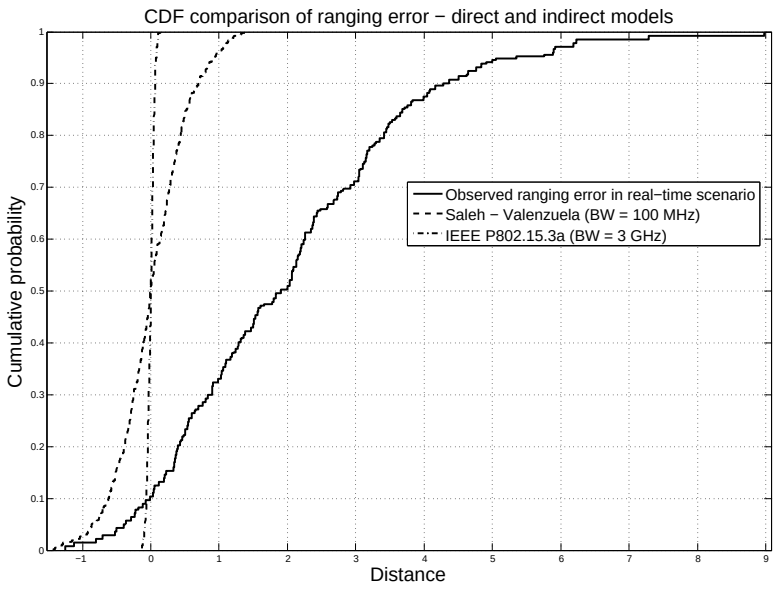

Figure 1.4: Sample channel profile exhibiting UDP conditions

Additionally, in order to deal with these UDP limitations, it is necessary to develop channel identification and mitigation mechanisms. In such schemes, UDP corrupted ToA range measurements must be identified and mitigated before incorporation into the localization process. In the literature, significant amount of work

has been reported on NLoS identification and mitigation in localization systems [Gez03, Con05]. However, their focus is on cellular localization where unbiased range estimation is usually assumed, which is clearly not the case in indoor environments. Recent results reported in [Guv07b, Ven07] propose to analyze the statistics of the propagation channel to infer the ranging condition and mitigate it. Although they introduce a unique approach to tackling the problem, they do not focus on UDP conditions and the work is not based on empirical measurements.

1.4 Main Contributions of the Dissertation

Contributions of this dissertation are mainly focused on the two open problems in the field of ToA-based localization. In the first part of the dissertation we present a new methodology and framework for modeling and simulation of dynamic variations of ranging error observed by a mobile user based on an application of Markov chain models. Markov chains, and particularly the hidden Markov model (HMM), are widely used in the telecommunication field. Previous research studies reported in [Kro97] proposed to exploit HMM in radar target detection. HMM structure can also be employed along with Bayesian algorithms, as shown in [Lad04], to provide a reliable estimate of the location of the mobile terminal and to trace it. Furthermore, recent studies propose to use HMM along with tracking algorithms to provide a footmark of the non-line-of-sight conditions and to present a reliable estimate of the location of the mobile terminal and to track it [Mor07].

We categorize the receiver location and its respective ranging error into four different classes and present clarifications as to the statistical occurrence of each class of ranging error. Furthermore, we provide distributions to model typical values of ranging error observed in each class of receiver location. Next, we link each class

of ranging error to a state of a Markov process which can be used for simulation of spatial behavior of ranging error for a mobile user moving randomly within a building. Finally, we provide a method to statistically extract the average probabilities of residing in a certain state for the building under study. The presented model for dynamic behavior of ranging error is essential for the design and performance evaluation of tracking capabilities of the proposed algorithms for indoor localization. The parameters of the Markov model are analytically derived from the results of the UWB measurement conducted on the third floor of the Atwater Kent Laboratories ($AKLabs$) at the Worcester Polytechnic Institute (WPI). The parameters of distributions of ranging error in each Markov state are extracted from data collected from a measurement-calibrated ray tracing (RT) algorithm simulating the same office environment.

In the second part of the dissertation, we shift our focus to the identification of the UDP conditions and develop two different algorithms, based on real-time UWB measurements, to identify the channel profiles with UDP conditions and then demonstrate their effectiveness in localization by employing them in a real scenario. The first algorithm uses a novel UDP identification and mitigation technique that is based on analyzing the statistics of the propagation channel. Specifically, this technique examines the channel excess delay, power of the first path and the total signal power to infer whether the mobile terminal is ranging in DDP or UDP conditions. Following the identification procedure the range estimate is mitigated through *a priori* knowledge of the ranging error statistics in both conditions. Results based on simulation and measurements show that localization error can be reduced substantially when our identification and mitigation technique is applied.

The second algorithm is an identification method of the UDP conditions based on an application of neural network architecture (NNA). Previously, NNA have

been exploited in the field of localization and tracking. Power measurements from different access points can be used to form an NNA for location estimation [Bat02], while [Ner06] utilizes variety of propagation parameters to form and train the NNA for location purposes. In this dissertation, propagation parameters of the radio signal are used initially to form the likelihood functions, and then, to construct and train the NNA. The database for these algorithms consists of channel profiles obtained from measurement-calibrated RT channel profiles as well as real-time UWB measurements conducted in *AK Labs*.

1.5 Outline of the Dissertation

The dissertation is organized as follows; Chapter 2 summarizes the measurement and simulation campaigns used for modeling the dynamic behavior of the DP and also for identification of the UDP conditions and compares the result of simulation with real-time frequency-domain measurement. Chapter 3 introduces a new framework for receiver location classification and discusses statistical behavior of ranging error associated with each class. Chapter 4 discusses the principles of Markov model, analytical derivation of the parameters of a Markov chain, and modeling the state probabilities. Chapter 5 starts the second part of the dissertation by discussing a new algorithm for UDP identification based on binary hypothesis testing, while Chapter 6 continues the discussion by introducing another algorithm for UDP identification based on neural network design. Finally, Chapter 7 is dedicated to summary of the dissertation and future research directions.

Chapter 2

Measurement and Simulation Databases

This chapter provides detailed description of measurement and ray tracing databases that are used to model dynamic behavior of ranging error and to identify UDP conditions, which are discussed in the following chapters. In the early stages of our research, we used power measurements to calibrate RT software to simulate channel profiles corresponding to different classes of receiver location in an indoor environment. Then, we used real-time wideband measurement to validate the ToA results of RT and to empirically model the dynamic behavior of ranging error. The results of RT simulation and measurement channel profiles are used to extract the estimated distance of the antenna pair for the specified locations of transmitter and receiver and consequently the value of ranging error. The channel profiles were also used to extract other RF propagation metrics for the purpose of identification of UDP conditions. Section 2.1 of this chapter describes the RT simulation setup, parameters of the RT software, and the simulation database. Section 2.2 discusses the measurement system, its related parameters, measurement scenario, and preliminary

results. Finally, Section 2.3 compares the channel profiles obtained from measurement system with similar channel profile generated from RT simulation in terms of occurrence of UDP conditions, ranging error observed in different conditions, power of the channel profile, and other related propagation parameters.

2.1 Ray Tracing Simulation Database

This section describes the process of generating channel profiles with RT software and also explains the effects of different parameters used in the RT software. The RT software used in this research, PlaceTool, was developed in CWINS to extract the channel profile between transmitter and receiver for a given environment. The software is able to simulate the channel for a variety of environments including indoor to indoor and outdoor to indoor. In terms of our research studies, since we only considered indoor to indoor scenarios we have only used the indoor to indoor feature of the RT software.

2.1.1 Introduction to Ray Tracing

RT software fundamentally provides a simulation environment to simulate the channel behavior in different areas [And93]. The basic mechanisms considered in ray tracing include transmission and reflection, diffraction, and scattering.

In indoor environments, usually reflection and transmission mechanisms govern the ray simulations and the effects of diffraction or scattering mechanisms become negligible. Using RT software it is possible to simulate the behavior of the signal, traveling from transmitter (T_x) to receiver (R_x), based on geometrical optic rules. By locating the T_x and R_x pair and their respective positions relative to the floor plan of the building, RT simulates the complete set of possible paths reaching R_x.

The output file includes necessary information such as received path amplitude, time delay, arrival angle, departure angle, phase, number of reflections, and number of transmissions of individual paths. The output only includes paths with significant power to contribute to the total power, while the software filters the other paths out. RT is usually used to produce massive databases of channel impulse responses for statistical analysis of the channel. The primary advantage in using RT is that it saves time and effort as compared with physical measurement. The following are some advantages of using RT over physical channel measurements [Ala06a]:

- Ease of visualization of the channel profile
- Lesser expense of RT tools relative to costly measurement equipment
- Ease of performing simulations
- Feasibility of conducting channel profile measurements in restricted and hard to access locations
- Ability to obtain channel profiles with infinite bandwidth

Although for design and performance evaluation of real-time localization systems measurement results are more preferable and reliable than RT simulations, for early stages of modeling using RT is highly recommended. Figure 2.1 illustrates a snapshot of our RT software [Hol92].

Rays are different paths traveling from the T_x toward the R_x. We used ray-shooting technique for our RT tool. Once all the possible rays have been traced to completion, the channel impulse response is formed [Hol92]. Figure 2.2 shows a sample of a channel impulse response taken from the same pair of T_x-R_x shown above. Detailed explanation about RT can be found in [Pah05].

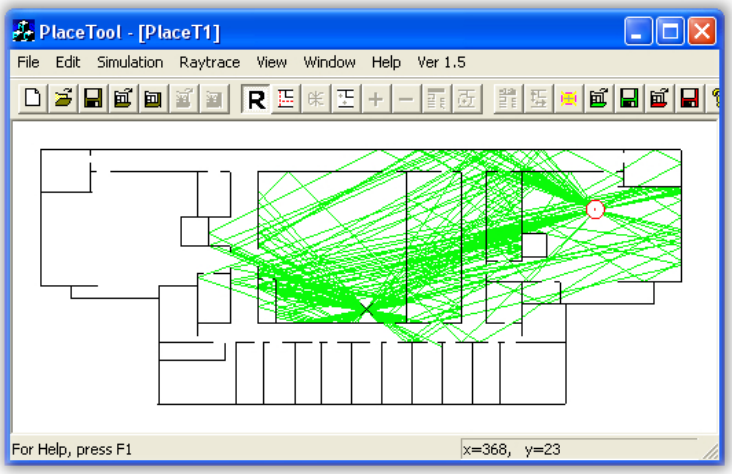

Figure 2.1: A sample snapshot of the CWINS internal ray tracing software - PlaceTool

2.1.2 RT Simulation Scenario

In this section we explain our scenario used for generating the database and describe the simulation procedure and its corresponding results. To generate a large database of the CIRs for a typical indoor environment we used a calibrated floor plan in RT. The floor plan is taken from the rooms of the third floor of $AKLabs$, WPI. The calibration process aimed to fit the results of measurements with the results of RT simulation by adjusting the reflection and transmission coefficients of the walls in the floor plan. Figure 2.3 illustrates this floor plan.

A very dense grid of receiver locations were implemented in the RT software to cover the entire floor plan. Receivers were spaced 30 cm apart in both X and Y direction, resulting in total number of 14000 receiver locations. Extra care was paid to the cases where the receiver location were located on the wall or exactly on the transmitter location in which the RT software could not generate an output. Locations of transmitters were fixed at the red crosses as Fig. 2.4 illustrates. For each transmitter location, 14000 CIRs corresponding to 14000 receiver locations

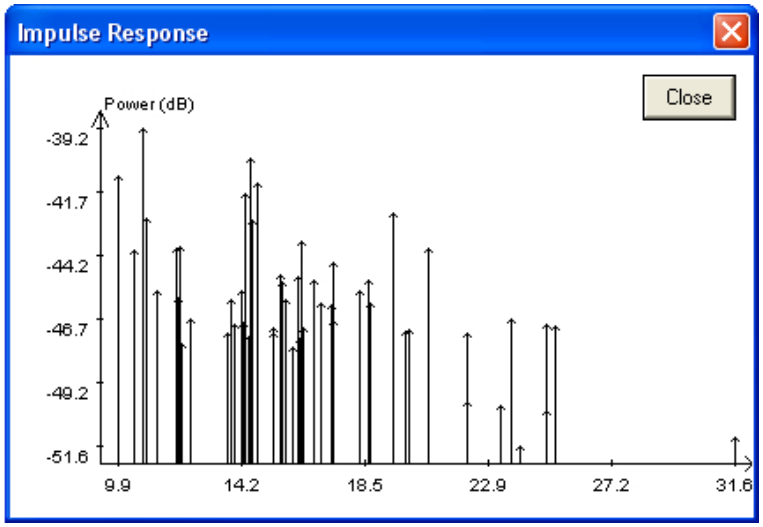

Figure 2.2: Sample snapshot of the CIR of the output of the ray tracing software

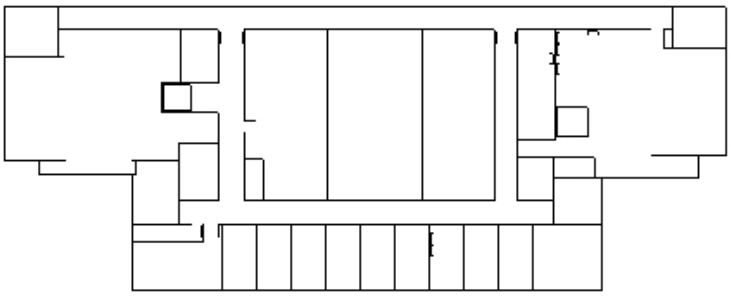

Figure 2.3: Floor plan of the third floor *AKLabs*, *WPI* - The details of the floor plan include two metallic shafts, all the metallic doors, and several metallic shelves located in the vicinity of the transmitters

were generated and stored which resulted in total of approximately 42000 CIRs.

After generating a CIR, it was processed in Matlab® to generate the respective channel profile. The process first started with filtering the CIR with a raised-cosine filter which translated the CIR into a raw channel profile. The next step is to determine the threshold of the channel profile. In the dynamic systems, threshold is a function of both background noise and dynamic range of the system, which is defined by the filter being used.

The use of raised-cosine filter implies a 31 dB dynamic range. However, in real

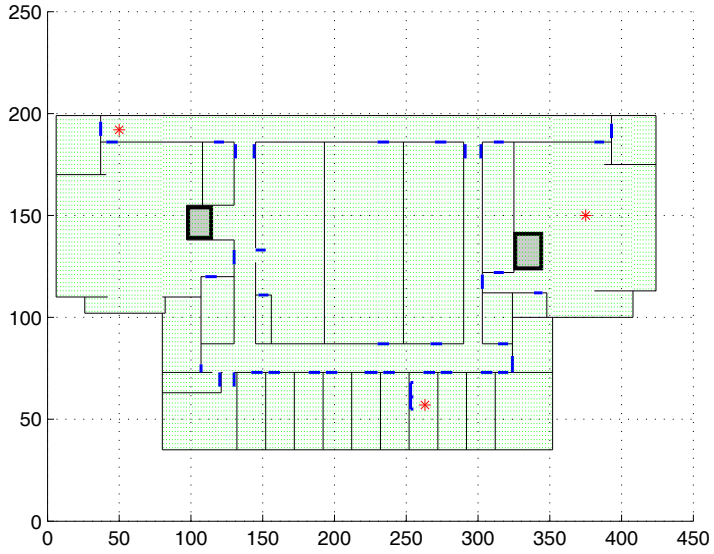

Figure 2.4: Grid representation of all the receiver locations and three transmitter locations - The locations of the transmitter were chosen carefully to generate variety of channel profiles

scenarios path combination can result in a peak before the DP, a false alarm. To avoid this situation, we set the dynamic range to 27 dB. The threshold could then be easily found as $\max(SP_{dB} - DR, BN)$ where SP_{dB} represents the power of the strongest component of the channel profile, DR represents the dynamic range, and BN represents the background noise. Then the channel profile was filtered against the threshold to filter the multipath components with amplitudes less than threshold out. At the final step, we performed a peak detection algorithm to determine the location of the peaks of the channel profiles. The output of the peak detection algorithm was then used to identify the important propagation parameters of the channel profile; estimated distance of the antenna pair, total power, FDP power, mean excess delay, RMS delay spread, and etc. The estimated distance is then used to form the error as discussed in Section 1.2.

2.2 Wideband Measurement Database

2.2.1 Measurement System

One of the most popular techniques to experimentally calculate the ToA is through the use of a frequency-domain measurement system which is described in [How90]. The main component of the measurement system used is an Agilent E8363B vector network analyzer. Figure 2.5 shows the measurement system and its components.

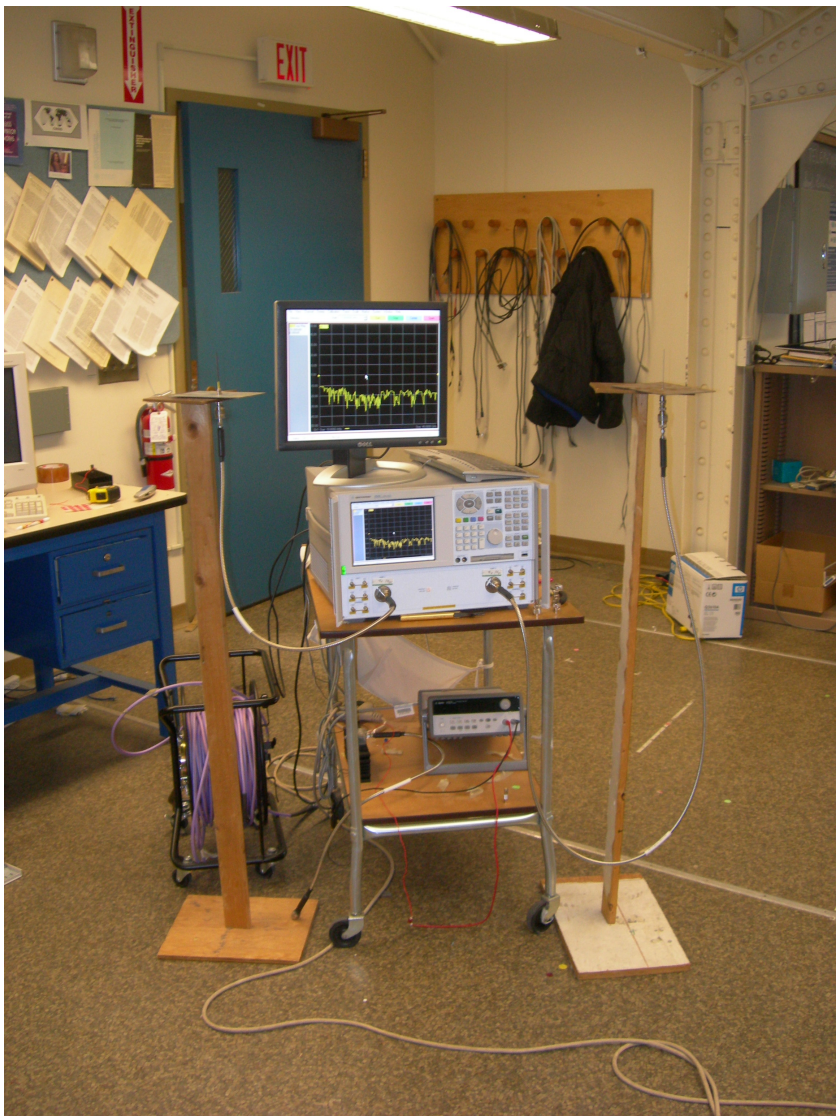

Figure 2.5: Measurement System

Transmitter and receiver are a pair of monopole 1 GHz quarter wave antennas which are connected to the network analyzer by low-loss cables. On receiver side a low-noise amplifier (LNA) is connected between the antenna and the network analyzer. The overall measurement system has a noise level of $-120\,dBm$. We also used a power amplifier in the transmitter side in order to have a larger range of coverage. The undesirable effects of the cables, LNA, antennas, and power amplifier are removed through system calibration. The power amplifier has 30 dB amplification with the frequency range of $10 - 4200\,MHz$, which overall the system was able to measure from $750 - 1250\,GHz$. Figure 2.6 shows the block diagram of this system.

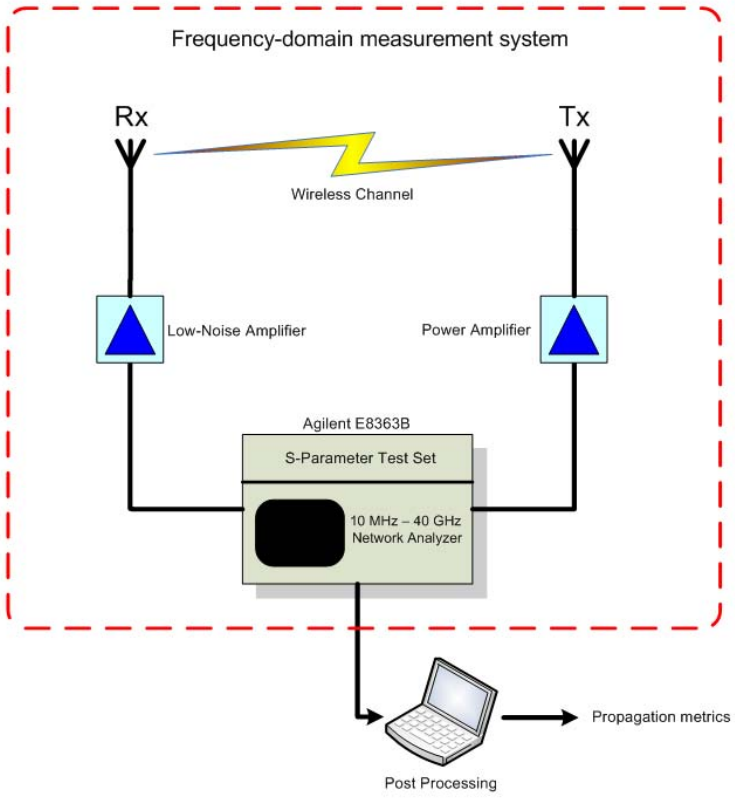

Figure 2.6: Block Diagram of the Measurement System

System calibration involves connecting the cables back-to-back without the antennas. This will remove the delay and attenuation of the cables. The second step

to system calibration is connecting the antennas and performing a 1-meter LoS free space calibration. This removes the delay and gain caused by the antennas. As a result the CIR after calibration in this case would be a single path occurring at $0\,ns$.

The user initializes the network analyzer at the start of each set of measurement where the start and stop sweeping frequencies are selected along with the number of desired samples and collects the data at the completion of each measurement. The transmitted signal passes through the power amplifier before going to the channel. The receiver component attenuates and preamplifies the incoming signal before passing it to the network analyzer. In this campaign, the network analyzer was used to sweep the frequency domain channel from $750 - 1250\,MHz$ with 1601 samples. The magnitude and phase of the measured frequency response were stored for each measurement and used later on for further processing. The frequency domain measurements were conducted by fixing the transmit antenna and moving the receiver around the desired locations. After data collection, the measured frequency domain channel profiles were further processed and the time-domain channel profile was obtained by use of inverse Fourier transform (IFT) in the form of Chirp-Z. Since the noise floor of the measurement system is $-120\,dBm$, and the raised-cosine window has side lobes of 31 dB below the maximum peak of the profile, a threshold is selected according to the larger value of the two. Figure 2.7 shows a sample frequency domain measurement and its corresponding time-domain profile. Notice the frequency selective fading in the frequency domain in Fig. 2.7(a). Also the time-domain profile illustrates the multipath components arriving in Fig. 2.7(b) at different delays with the first path not the strongest which in this case it is an DDP condition. In this figure, the time-domain profile is obtained by application of the Chirp-Z IFT followed by a raised-cosine window.

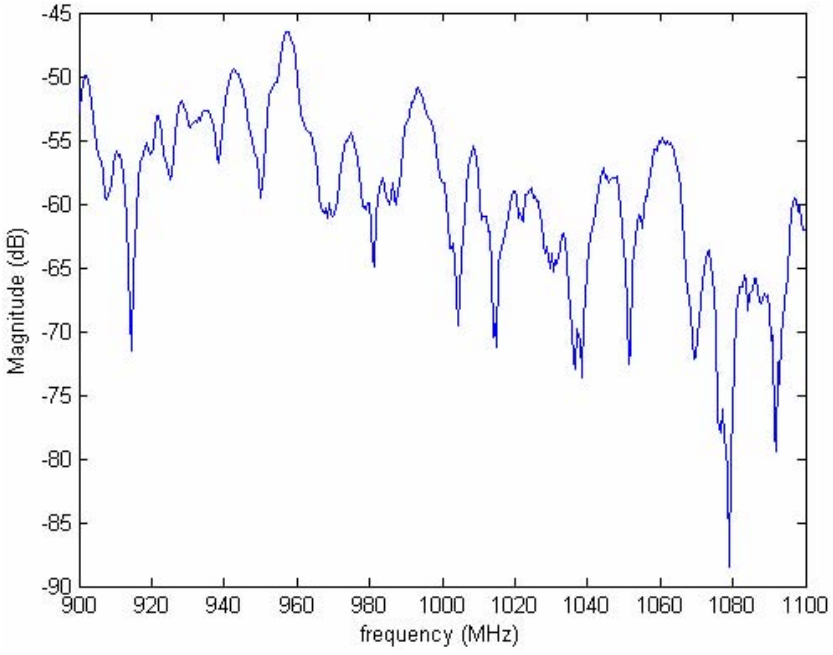

(a)

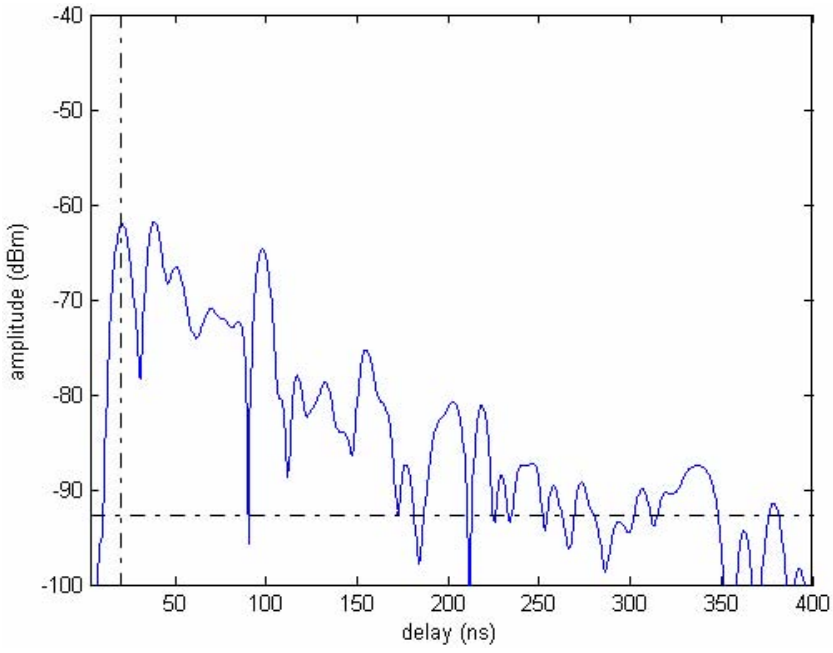

(b)

Figure 2.7: (a) Sample frequency domain measurement from network analyzer - absolute value of the received frequency domain measurement and (b) Corresponding time domain channel profile obtained by the Chirp-Z transformation

2.2.2 Measurement Scenario

In this section we introduce a dynamic scenario of operation with defined walking routes in a typical office building. Figure 2.8 shows our dynamic scenario on the third floor of the *AK Labs* at *WPI*, where a user walks along different routes in the central part of the building.

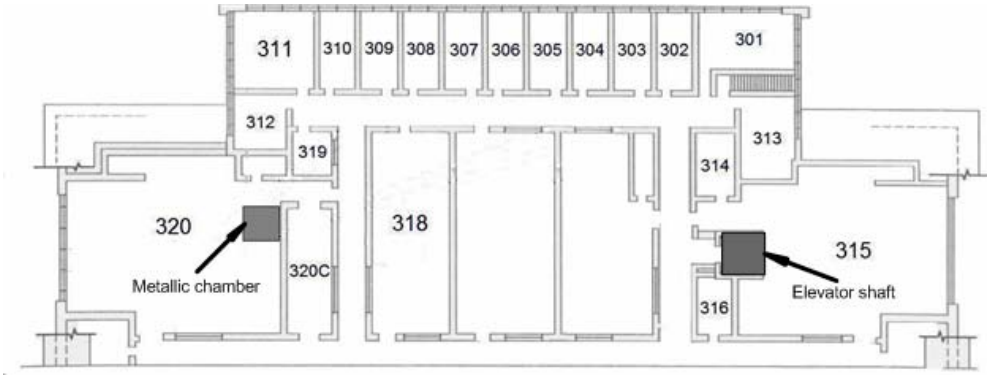

Figure 2.8: Floor plan of the third floor of the *AK Labs* used for conducting wideband measurements - The locations of the metallic shafts are pointed out in the floor plan

There exist two large metallic objects on two sides of this floor plan: an elevator on the right and an RF-isolated chamber on the left. These two objects block the signal paths; in particular, when located between transmitter and receiver they obstruct the direct signal traveling from transmitter to receiver. This causes shadowing of the signal (SUDP conditions). Figure 2.9 shows the walking route in the building, a loop route in which the mobile user walks in the central part of the building. Transmitter 1 (T_{x_1}) is located in the middle of the large laboratory on the left.

For this transmitter, we have substantial SUDP conditions in the upper and left side corridors, but there are no SUDP conditions in the lower and right side corridors. When the mobile takes the central loop route, it observes a SUDP condition approximately 40% of the time. With T_{x_1}, as we trace the mobile along the routes,

we can observe different possibilities for occurrence of shadowing conditions to analyze the behavior of the large ranging errors and effectiveness of different techniques in mitigating them. In the coming chapters we discuss shadowing identification techniques using statistics of RF propagation parameters for all transmitter locations, T_{x_1}, T_{x_2}, and T_{x_3}. The walking route consisted of 76 receiver locations each $1\,m$ apart. This resulted in 76 channel profiles per transmitter location, in which we took five snapshots of channel profile corresponding to each receiver location. The total number of measurements were 228 channel profiles each with five samples.

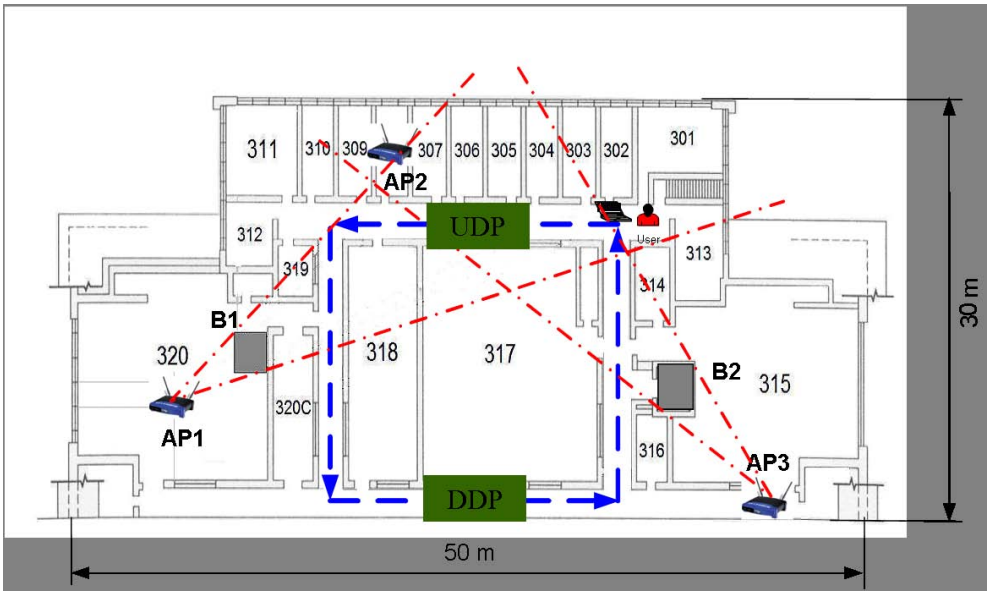

Figure 2.9: Walking route in the same scenario for three different access points - It can be observed that metallic shafts cause instant SUDP for two transmitters

2.3 Comparison of Ray Tracing Simulation and Empirical Wideband Measurement

For the purpose of comparison of the channel profiles obtained from measurement system and RT channel profiles, we performed a comprehensive comparison of the

two approaches. The rest of this chapter focuses on the comparison of measurement and RT and discusses the possible explanations of the theories behind the discrepancies among the two when they are used for algorithm development for indoor localization.

To initialize the comparison we start with a scenario where first measurements were conducted with different obstacles between the transmitter and the receiver. The setup of the measurements was similar to earlier loop measurements. Specifically, two sets of T_x-R_x locations were chosen as illustrated in Fig. 2.10.

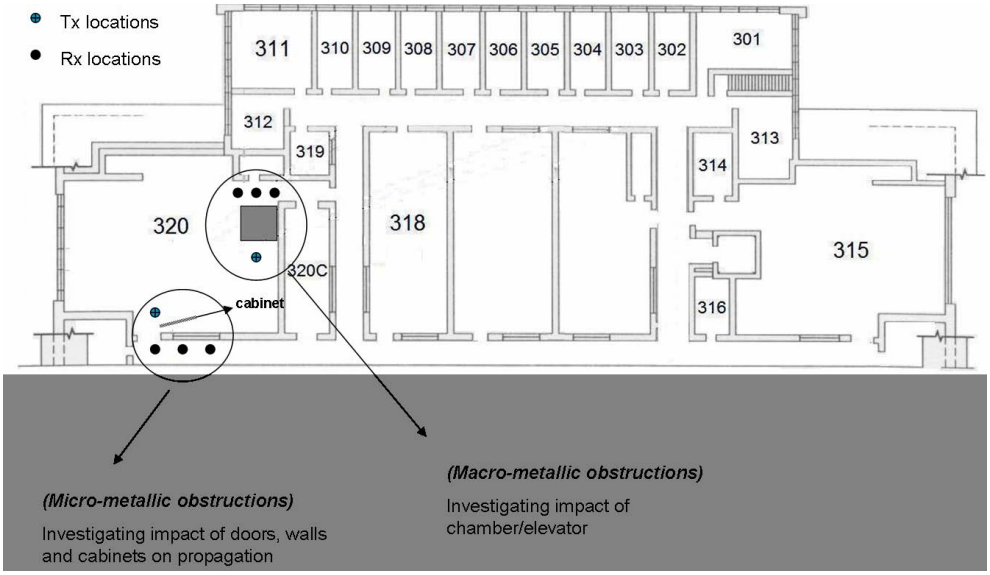

Figure 2.10: First scenario for comparison of measurement and RT - with emphasis on the effects of metallic objects on ToA measurements

In the first location the T_x and R_x were separated by a wall with a metallic door. The impact of the metallic door on signal propagation would highlight that the blockage of the DP with a light metallic object can cause $1m$ of ranging error. In addition penetration through interior walls and cabinets revealed that multipath and signal attenuation in that scenarios can cause errors ranging from $0.6-1.6m$. Similar channel profiles were generated using RT simulations. The comparison between measurement and RT can be seen in Fig. 2.11 which shows the results for the

metallic door scenario illustrated in Fig. 2.10.

It can be seen in Fig. 2.11(a) that in LoS environment the DP component can easily be detected. The experiment also investigates the effects of the human body in close distances on the detection of the DP component. It can be observed that in close distances the human body causes almost $15\,dB$ of attenuation to the power of the DP component. In this case the DP component was still detectable but it can be easily verified that as the distance increases the likelihood of detection of DP component with human body interference decreases. Finally, as we close the metallic door the DP component is completely blocked and the next peak is detected as the DP component and it can be seen that ranging error of $0.8\,m$ has occurred.

The second figure, Fig. 2.11(b) describes the effects of walls and metallic shelves on the detection of the DP component. It can be observed that with only a thin wall between the transmitter and the receiver it is possible to observe $0.6\,m$ of ranging error. The introduction of the metallic shelf causes larger ranging error, in the order of $1.6\,m$. These results can also be verified by RT simulations as Fig. 2.12 for a different set of measurements.

The dashed line represents the result of measurement versus RT when the door is open. Results from both measurement and RT provide an accurate estimate of the ToA with negligible distance measurement errors ($\varepsilon_{RT} = 0\,, \varepsilon_{meas} = 0$). When the door is closed the ranging errors will change to $\varepsilon_{RT} = 3.5\,m$ and $\varepsilon_{meas} = 2.2\,m$.

The next measurement scenario focused on the metallic chamber which could emulate an elevator shaft. As expected, the chamber caused significant ranging errors of $2 - 3\,m$. Figure 2.13 shows the results of measurement versus RT when transmitter and receiver are located in different sides of the chamber shown in Fig. 2.10.

This time $\varepsilon_{RT} = 6.4\,m$ and $\varepsilon_{meas} = 2.4\,m$ which are substantially different. In

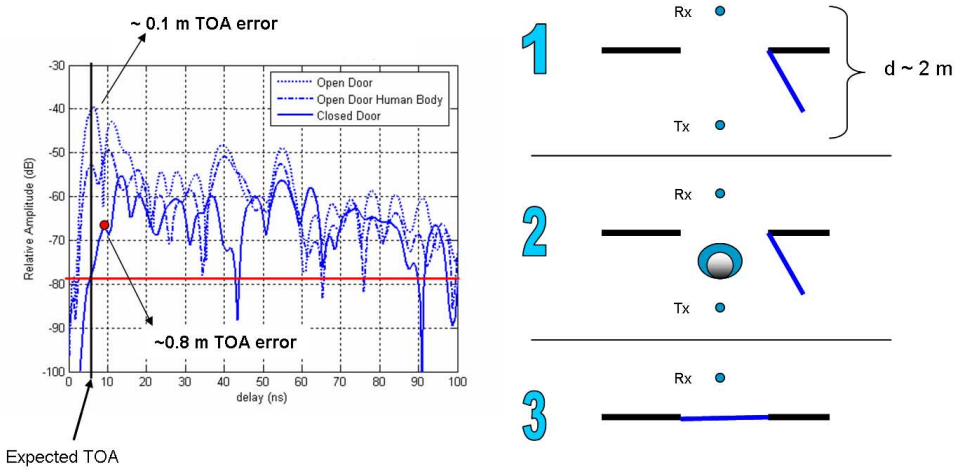

(a)

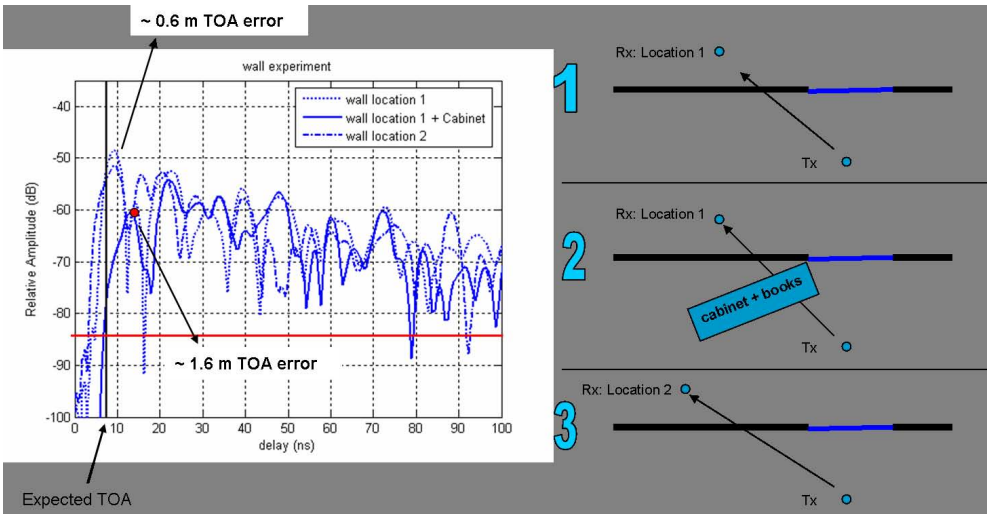

(b)

Figure 2.11: (a) Comparison of channel profiles obtained from measurement and RT software for the metallic door scenario and (b) Comparison of the measurement channel profiles and RT channel profile for the metallic chamber scenario

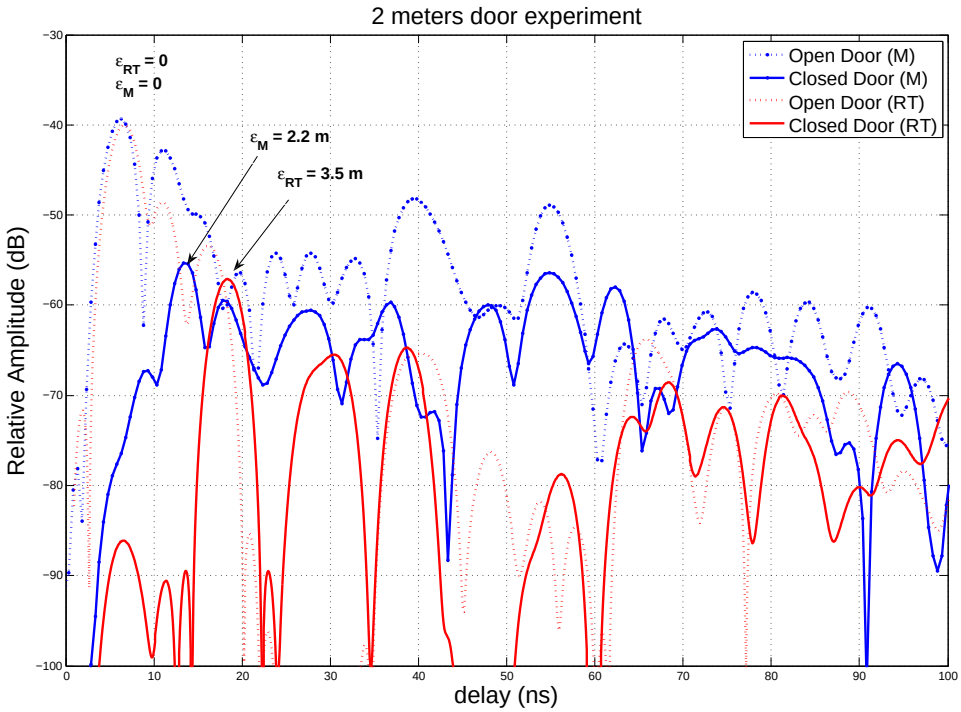

Figure 2.12: Comparison of the results of RT versus the channel measurements for the door scenario

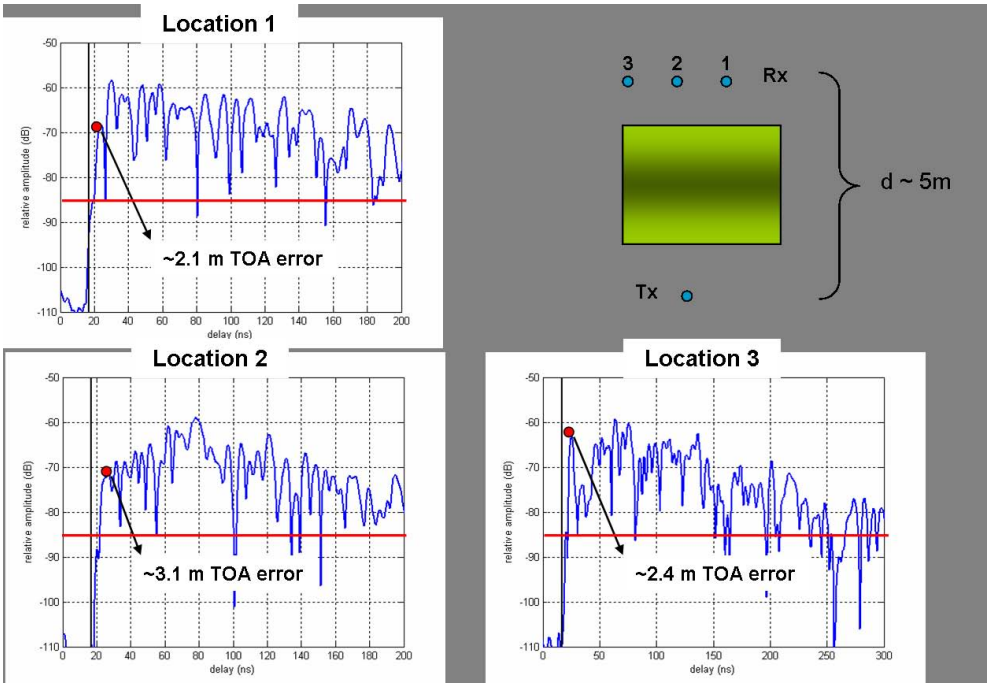

Figure 2.13: Comparison of the results of the RT versus the channel measurements for the chamber scenario

our primary observations we can see more differences when the transmitter/receiver is closer to the chamber.

2.3.1 Effects of Architectural Micro-Metals

In the second setup, measurements across a corridor on the third floor of *AK Labs* were conducted to highlight the impact of micro-metallic obstructions such as cabinets and those metal studs within the walls. Figure 2.14 shows the scenario used to compare RT and measurement results.

In those measurements transmitter was located inside CWINS lab, ($AK320$), and we have selected ten consecutive receiver locations along this corridor, each with one meter distance from its neighbor locations. As the receiver is moved along these ten points, we start with LoS conditions between the T_x and R_x, then we go to NLoS without micro-metals in between, and finally we arrive to an area where a

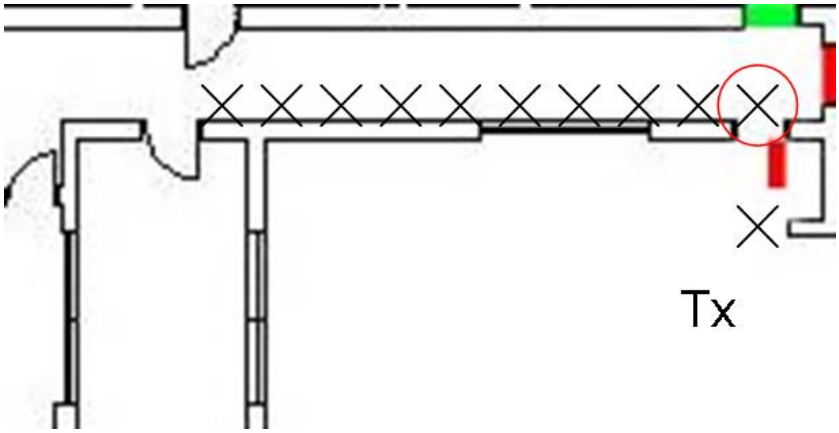

Figure 2.14: Corridor scenario for comparing the results of RT and measurement channel profiles and their respective ToA measurements

micro-metallic object (a shelf) appears between the T_x and R_x.

Figure 2.15 shows the comparison of the results of RT and measurement associated with the circled point shown in Fig. 2.14.

In this location the distance between the transmitter and the receiver is $2\,m$ and they are located in LoS condition across the open door between lab and corridor. Blue line in Fig. 2.15 represents the measurement with 500 MHz bandwidth, the red line represents the results of RT when we add a raised cosine window with a bandwidth of $500\,MHz$ to the RT generated channel impulse response, and the black lines shows the first five paths traced by the RT program. Our objective is to analyze the ToA of the FDP and strongest path (SP) and their respective persistency. To analyze the behavior of the DP in the scenario shown in Fig. 2.14, we produced 10 profiles of the results of measurements, results from RT with 500 MHz bandwidth, and the first five paths.

Figure 2.16 illustrates the comparative results obtained from these figures when FDP or SP components are used for range estimation.

Examination of the files and the summary results of Fig. 2.16 for the FDP and the SP reveals that

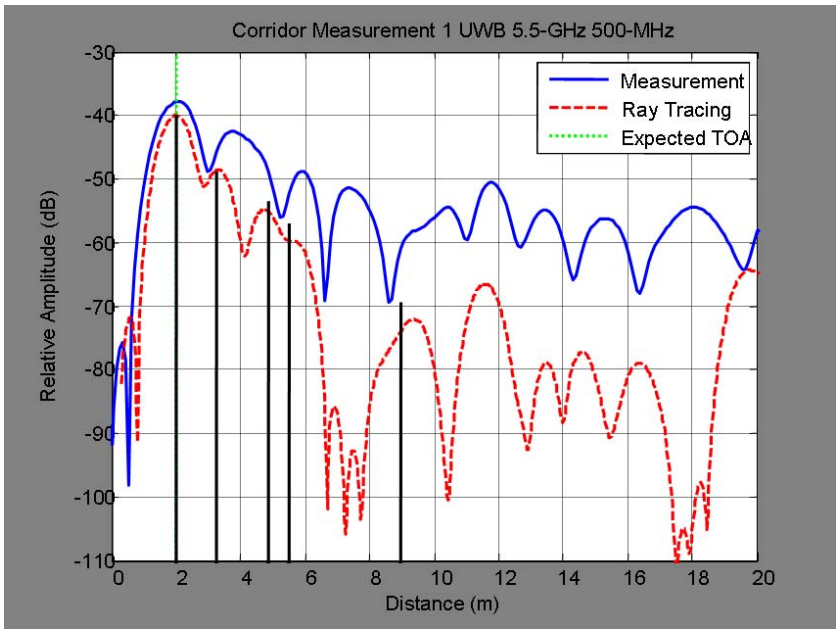

Figure 2.15: Comparison of measurement and RT channel profiles for the first point in corridor scenario

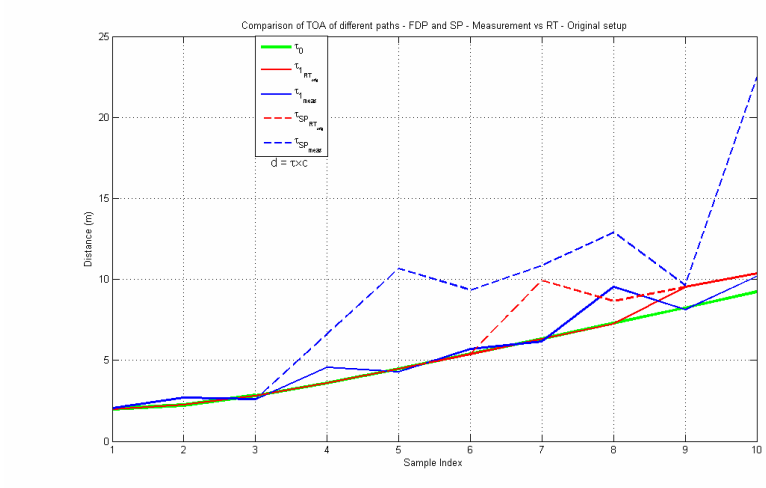

Figure 2.16: Comparison of the ranging estimate obtained from measurement and RT channel profiles

1. In close distances considered in our scenario the FDP is more persistent than the SP and it should be used to examine the results.

2. For the FDP all points show close agreement except for location 8 where it seems that some of the paths in the measurement are combined so that the peak detection algorithm can not detect them while they appear in the RT results.

Close examination of the first few paths in all figures also suggests that number of paths in the measurement is higher than the number of paths obtained from the RT results. Motivated by these two observations the details of the RT layout in this small area were further modified. The channel profiles comparing the results of RT with those of measurement for all the 10 points are provided in Appendices A, B, C.

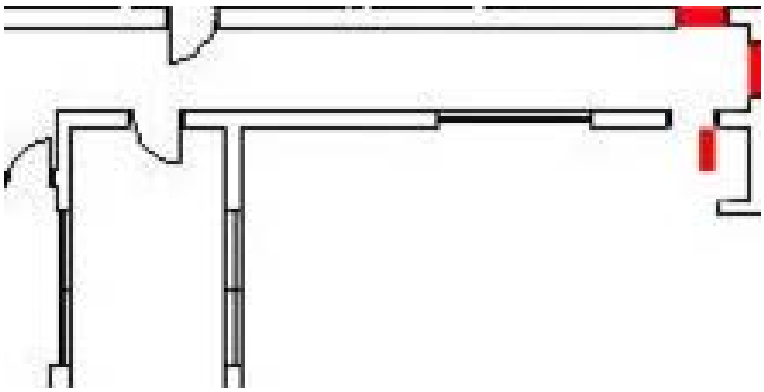

Figure 2.17: Modifications to the original floor plan to include the metallic details of the building

In the original layout shown in Fig. 2.14 the open doors are not included; in addition the green color door was assumed to be a part of the wall defining the boundaries of the building. To match the file the location of the shelf was also adjusted. These adjustments were done at the resolution of the GUI which is 13 cm and the modifications are shown in Fig. 2.17.

Figure 2.18 shows the summary results for the FDP after these adjustments, point 8 shows better agreement. These results show small error for location one through seven and a jump in error for locations $8-10$ where the metallic shelf obstructs the DP between the transmitter and the receiver.

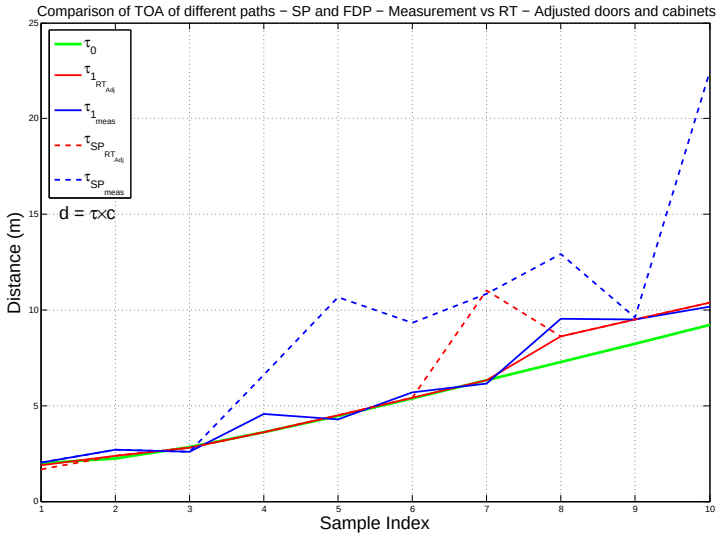

Figure 2.18: Comparison of the ranging estimate obtained from measurement and RT channel profiles after modifications to the original floor plan of the building under study

It can be observed that even small adjustments to the details of the floor plan which is used for RT software affect the accuracy of the ToA measurement. These small adjustments, however, are very hard to implement as one may not be able to identify the cause of adjustment at first glance.

2.3.2 Effects of Scattered Micro-metals

Motivated by the new theory of the effects of micro-metals on the ToA range estimate of the received multipath profiles we added all metallic doors and as many

metallic cabinets as we could identify in the building to the RT floor plan of the third floor of *AKLabs* used as our loop testbed scenario and examined throughout this dissertation. Comparison of the results of RT with measurements provided closer agreements when we included the architectural micro-metals (doors and shelves). Further analysis revealed that the results of RT with architectural micro-metals provide more optimistic estimate of the ranging error in the DDP areas and more pessimistic results in UDP areas. To explain this situation we argued that in the DDP areas if we have no micro-metals, RT almost always detects the DP. With the addition of architectural micro-metals, predictions from the RT get closer to those of the measurements. The remaining difference must have been caused by other metallic objects which we can refer to them as scattered micro-metals. Figure 2.19 shows snapshots of scattered micro-metals in the CWINS labs where Tx_1 is located. These are computer terminals, metallic furniture, and other scattered metallic objects in the area. In the UDP areas scattered macro-metals block the DP but reflections from these micro-metals create more opportunities for a path to reflect or scatter from these objects making RT results look pessimistic.

2.3.3 Closeness of RT and Measurement Channel Profiles

First we used the traditional RT software with the original floor plan to extract the propagation parameters of the wireless channel between the transmitters and receiver locations on the loop specified in Fig. 2.9. We then changed the floor plan to include as much as architectural micro-metallic details of the building. These details included metallic doors, whether open or close, metallic shelves and cabinets, and metallic mount boards. After inclusion of these details we again ran the RT program to extract the propagation parameters of wireless channel between the transmitter and receiver.

Figure 2.19: Scattered metallic object in the vicinity of the transmitter location

Before the inclusion of the details and with the original floor plan, we compared the channel profiles obtained from RT and measurement in terms of their respective ranging error and total power. Figure 2.20 illustrates the comparison of the ToA ranging error.

Similarly, Fig. 2.21 compares the result of total power of the channel profiles obtained from measurement and original RT. It can be seen that in terms of total power of the channel profile, the results of RT and measurement are really close to each other.

This is no surprise as the original RT software and the details of the floor plan were designed and adjusted accordingly to reflect the power characteristics of the channel profile and match the results of frequency-domain measurements.

In the next step, we included limited number of micro-metallic details, mainly

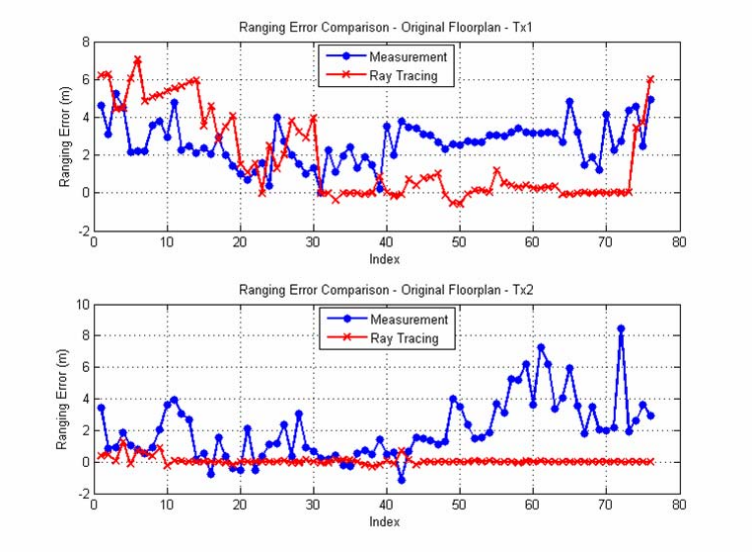

Figure 2.20: Comparison of ToA ranging error for measurement channel profiles and channel profiles obtained from RT with the original floor plan which excluded micro-metallic objects and included only two metallic shafts

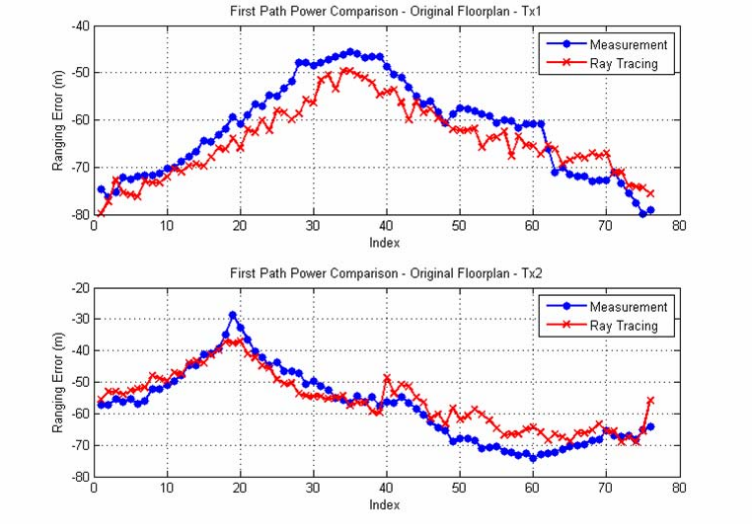

Figure 2.21: Comparison of total power of the channel profile for measurement channel profiles and channel profiles obtained from RT with the original floor plan which excluded micro-metallic objects and included only two metallic shafts

those who were around the transmitter locations, to observe the effects of micro-metallic objects on the comparison of the channel profiles, in terms of their respective ToA ranging error and total power. Figure 2.22 compares the ToA ranging error of the measurement channel profiles and new RT channel profiles. It can be seen that the ToA curves are now comparable.

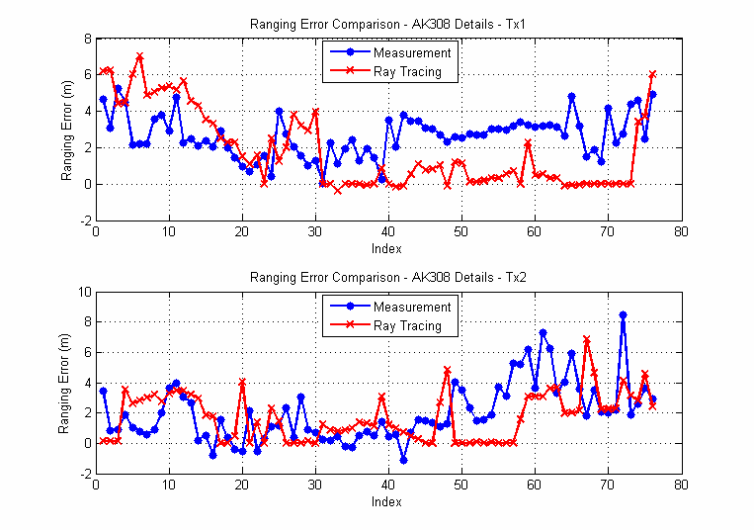

Figure 2.22: Comparison of ToA ranging error for measurement channel profiles and channel profiles obtained from RT with the modified floor plan which included limited micro-metallic objects

This confirms the previous results of matching the RT and measurement that in order to fully match the channel profiles in terms of their respective ranging error (or ToA measurement) we have to include all the necessary details of the building in the floor plan used for ray tracing. The emphasis should be on metallic details such as metallic doors, metallic shelves and elevator shafts. Other scattered metallic objects are preferably required to be included but are very hard to identify and model. The bottleneck of these additions is the cost of identifying these details and implementing them in the floor plan of the building which can be both time and resource consuming and some time user might not even be able to identify the

obstructive objects.

In the final step, we included all the micro-metallic details of the building. Figure 2.23(a) illustrates the comparative results from measurement and RT in location 39 identified in Fig. 2.23(b).

The results are presented in the dB form to lay more emphasis on the differences. In general results of linear plots appear closer to one another. To investigate the effectiveness of the addition of the micro-metallic objects to the accuracy of the ranging error estimation, we observed the ToA measurement of the DP (or consequently the distance between the transmitter and receiver) for the cases with and without the addition of the metallic details of the building to the floor plan.

Figure 2.24 shows the persistency of the FDP obtained from results of RT without architectural micro-metals (red line), with architectural micro-metals (dashed red line) and results obtained from measurements (blue line). The ToA of the FDP is transferred to its equivalent distance, $d = \tau \times c$, in meters so that it can be compared with the actual distance between a receiver location on the loop and the location of the Tx_1 (green line). To further illustrate the similarities among these plots we resort to the CDF of the ranging error values of the FDP from the ToA of the direct path (DP) if it could be detected exactly $\varepsilon_1 = (\tau_1 - \tau_0) \times c$ where τ_0 is the arrival time of the DP.

The red line in Fig. 2.25 shows the CDFs of the ranging error of arrival times from the results of original RT, $\varepsilon_1 = \tau_{1_{RT}} - \tau_0$. The dashed red line and blue line represent the ranging errors obtained from RT with architectural micro-metallic and the measurements, respectively. In general addition of micro-metallic details to the RT plan brings the statistical behavior of the FDP predicted by RT closer to those observed in the measurements.

These results also reveal that after inclusion of the architectural micro-metallic

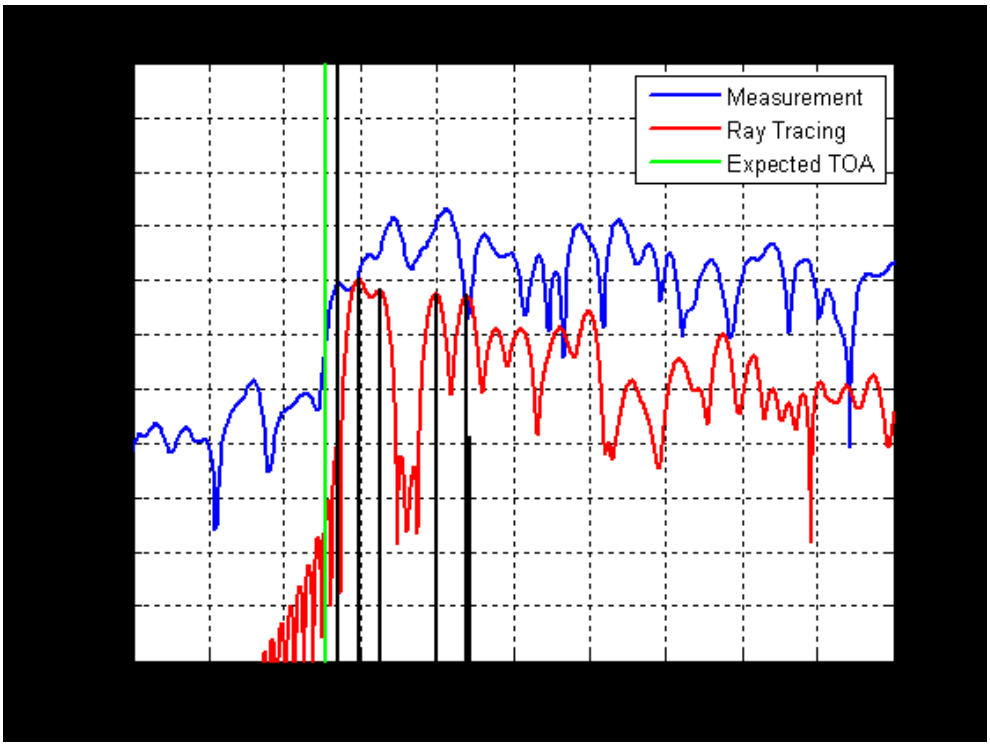

(a) Comparison of RT and measurement channel profiles corresponding to the receiver location 39

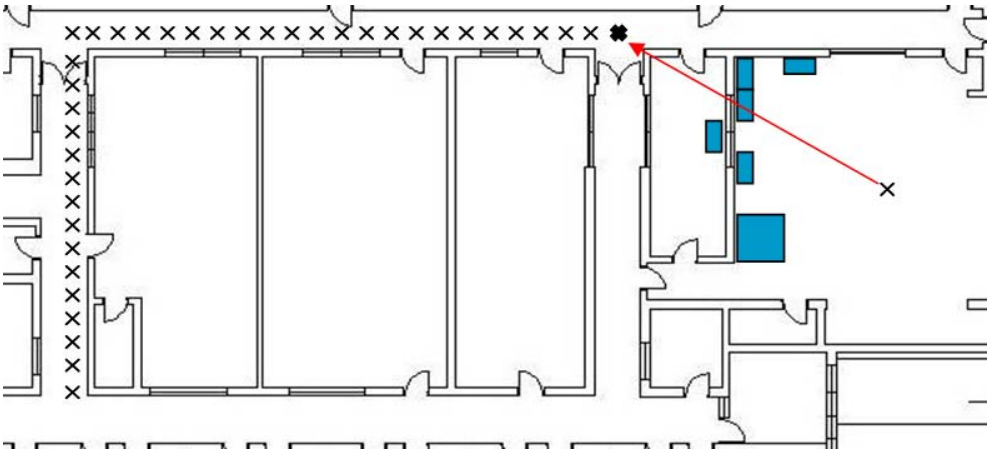

(b) Receiver locations around the loop - emphasis on the point 39

Figure 2.23: (a) Comparison of channel profiles obtained from measurement and RT software for the metallic door scenario and (b) Comparison of the measurement channel profiles and RT channel profile for the metallic chamber scenario

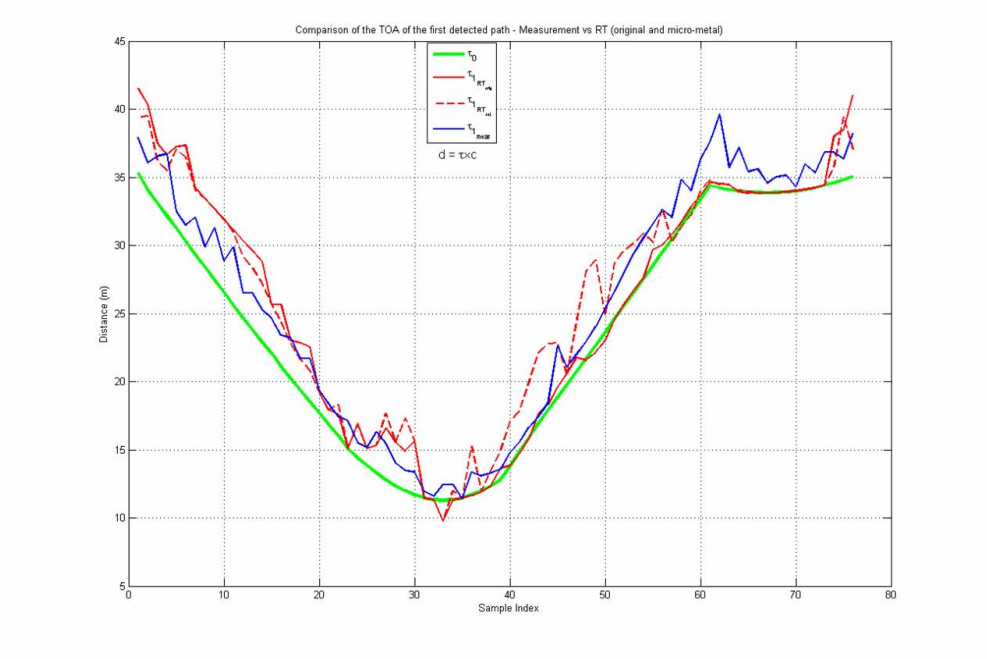

Figure 2.24: Comparison of ToA range estimate for measurement channel profiles and channel profiles obtained from RT with the modified floor plan which inclusion of metallic details of the building

objects for ranging errors up to around $1.5\,m$ (close to the width of the pulse at $500\,MHz$) RT provides more optimistic results than actual measurements while for larger errors RT provides more pessimistic results. The smaller errors are related to the DDP locations and the larger errors are associated with the UDP conditions. Therefore, we can draw a general conclusion that the RT provides optimistic results in DDP areas and pessimistic results in UDP areas.

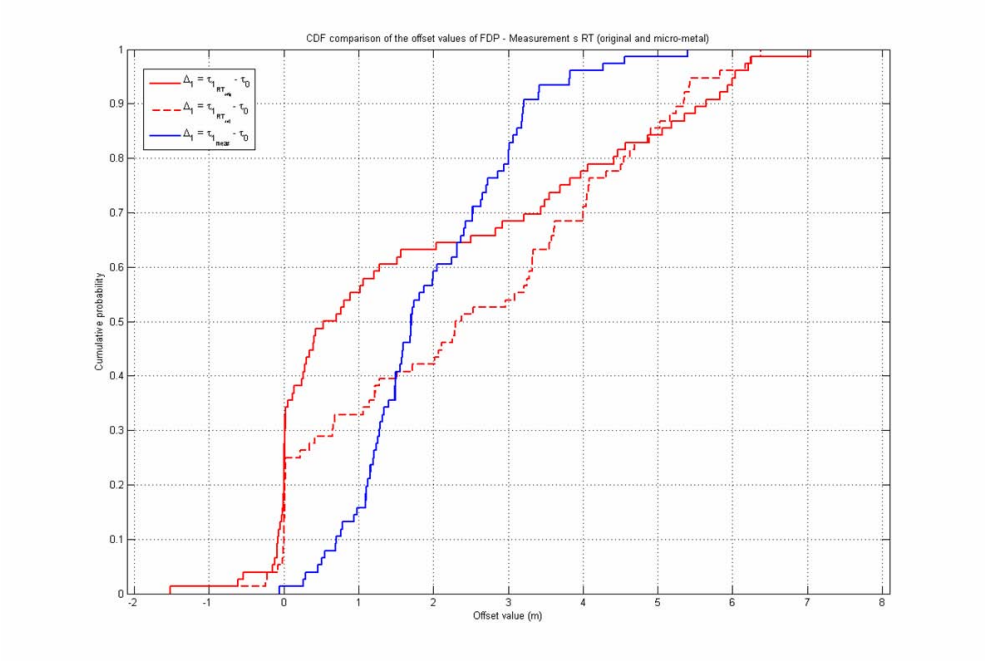

Figure 2.25: Comparison of ToA ranging error for measurement channel profiles and channel profiles obtained from RT with the original floor plan which excluded micro-metallic objects and included only two metallic shafts

Chapter 3

Receiver Location Classification for Modeling the Behavior of Direct Path

In this chapter our focus is on constructing a meaningful framework for classification of the receiver location. As the mobile terminal travels in indoor environment the CIR components change their amplitude and phase. The rate of these changes is dependent on the type of the environment and the details of the indoor environment. Our focus is on modeling the behavior of the DP component in indoor environment. As the mobile terminal changes its position, the DP component changes its class. If there are no obstacles between the transmitter and receiver, the DP component is above the detection threshold and can be detected. As the mobile terminal moves, the power of the DP component decreases and at certain break-point it can no longer be detected. The modeling of behavior of the DP component under occurrence of such conditions is essential to design and development of localization and tracking systems. This chapter defines an indicative categorization for all the possible

classes of receiver location which exhibit different types of ranging error. Section 3.1 describes the four major classes of receiver locations observed in indoor environment. Section 3.2 discusses the receiver location classification based on power characteristics of the channel profile. Section 3.3 introduces new method for classification which is based on the distance of the antenna pair and geometry of the building (used for identifying shadowing conditions). Finally, section 3.4 discusses the statistics of ranging error observed in each class of receiver location.

3.1 Four Classes of Receiver Locations

As already discussed, simple receiver location classification considers each receiver location to be either in LoS conditions or NLoS conditions. However, previous research illustrates that in NLoS conditions it is also possible to detect the DP component [Pah98]. Since the important parameter in ToA-based localization system is the DP component, it is a reasonable idea to classify the receiver locations based on detection of the DP component. This has resulted in DDP/UDP classification. In DDP conditions, the error in ToA estimation is small. On the other hand, the performance of ToA-based positioning degrades significantly when a user moves into a UDP condition which exhibits large ToA estimation errors due to the loss of the DP. In this section we try to differentiate between DDP errors and UDP errors in their characteristics. We ran RT for two different scenarios. In scenario "A" the transmitters location was fixed and the receiver was moving away from the transmitter location in a straight line. The scenario was intended in a way that there was no metallic obstacle between the receiver and the transmitter to cause UDP to happen. Figure 3.1(a) discusses the scenario. At the top total received power is graphed, with the power of the FDP right below it and true power of the DP next

(refer to the right axis), and at the bottom the respective ranging error is shown (refer to the left axis). As Fig. 3.1(a) illustrates, even with no metallic objects in between, ranging error is subject to be large. We have referred to these errors as NUDP conditions.

It can be noticed from Fig. 3.1(a) that NUDP occurs in small bursts and its respective ranging error is less than $0.5m$. On the other hands, scenario "B" illustrates another situation in which a metallic chamber was located between the transmitter and the receiver in some of the receiver locations. A closer look at ranging error will reveal that these errors and their widths are larger than NUDP. This is referred to as SUDP, as Fig. 3.1(b) illustrates.

Therefore, we are able to classify the UDP error into NUDP and SUDP. NUDP refers to those ranging errors which are relatively small and they occur in small bursts. On the other hand, SUDP refers to large ranging errors with wider duration of occurrence. However, a fourth class of receiver location exists in which the distance of the antennas are larger than coverage of the system and hence the communication link between the antenna pair can not be established [Ala06a]. These receiver locations are referred to as no coverage (NC) class. The comprehensive classification of the receiver locations in indoor environment is illustrated in Fig. 3.2.

The major sources of ranging error related to ToA-based localization systems are also identified in Fig. 3.2, for each class of receiver location. It can be seen that multipath induced ranging errors are common in all classes while blockage induced ranging errors are only observed when the receiver location is identified as SUDP.

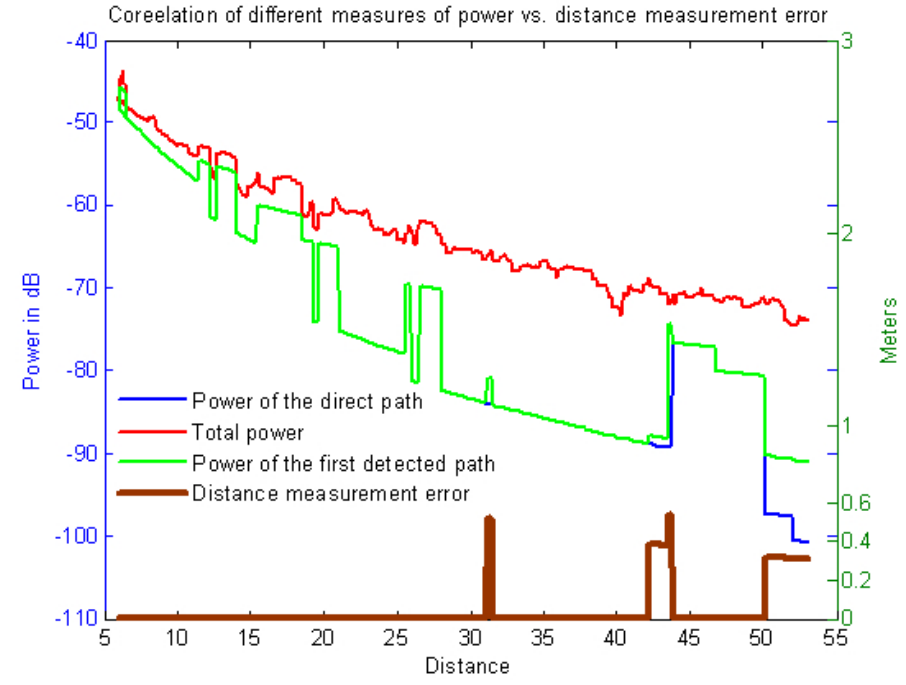

(a)

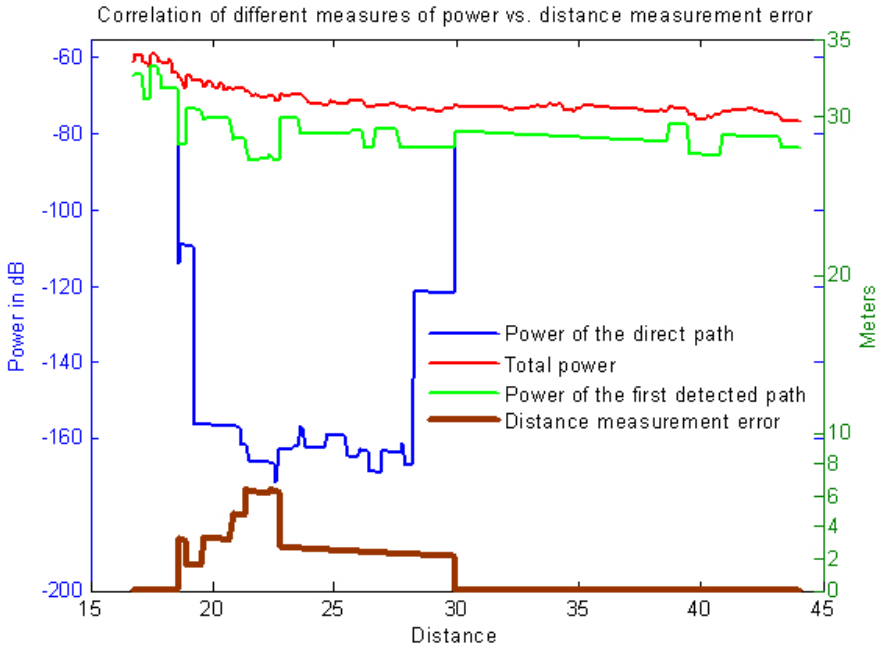

(b)

Figure 3.1: Classification of UDP conditions, a) A NUDP scenario which avoided obstruction by macro metallic objects and b) SUDP scenario in which a metallic chamber obstructs majority of the receiver locations and creates UDP conditions as the receiver moves along the corridor

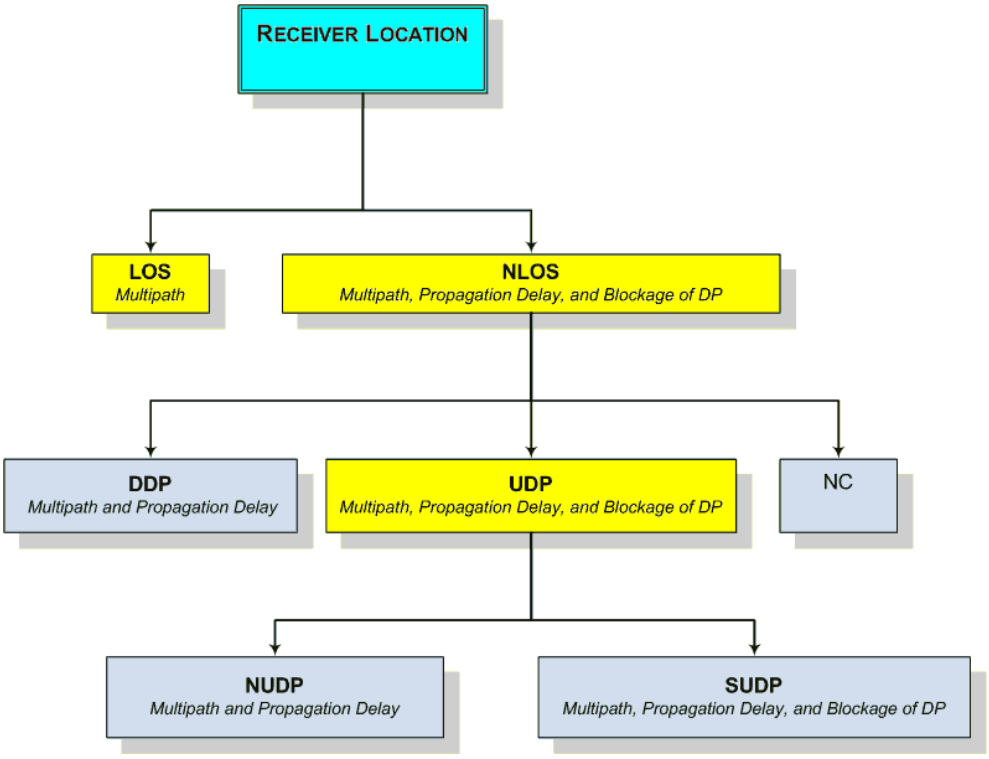

Figure 3.2: Receiver location classification

3.2 Ranging error classification based on power

The receiver location classification is mainly accomplished by the means of power. In such classifications the class of ranging error associated with each receiver location can be defined according to power of the DP component and total received power given by

$$P_{DP} = 20log_{10}(|\alpha_{DP}|) \tag{3.1a}$$

$$P_{tot} = 10log_{10}(\sum_{l=1}^{L}\sum_{k=1}^{K}|\alpha_{k,l}|^2) \tag{3.1b}$$

and also blocking condition, λ_i, a binary index to indicate the blockage of DP and its adjacent components by an obstructive object. In this paper, it is assumed that for the specified location of the transmitter and receiver, the true value of λ_i is known, where $\lambda_i = 0$ represents a channel profile which is not blocked and $\lambda_i = 1$

represent a channel profile which is blocked by an obstructive object.

In DDP class of receiver location, which indeed is a sub-class of LoS, $\lambda_i = 0$, $P_{DP} > \eta_1$, and $P_{tot} > \eta_2$, in which $\eta_{1,2}$ represent the respective detection thresholds for DP and total power and are dependent on the measurement noise of the system. Fixing the transmitter power at a regulated level, η_1 can be related to the dynamic range of the system. Although, increasing the dynamic range of the system, i.e. decreasing η_1, raises the likelihood of the DP component to be detected at the receiver side but it also increases the probability of detecting a noise term (or a side-lobe peak) as the DP component, i.e. a false alarm [Guv07a]. Efficient selection of the proper values of $\eta_{1,2}$ can improve the accuracy of the localization system [Guv05]. Typical values of $\eta_{1,2}$ are $5 \sim 10\, dB$ above the measurement noise present in indoor environment.

In DDP conditions, $\tau_{FDP} \approx \tau_{DP} = \tau_{1,1}$ and $\varepsilon = (\tau_{FDP} - \tau_{1,1}) \times c$ results in insignificant ranging error associated with the ToA measurement given by

$$f_{\boldsymbol{\varepsilon}_{DDP}}(\varepsilon) = f^{\mathbf{M}}(\varepsilon) \tag{3.2}$$

where $f^{\mathbf{M}}$ represents the multipath induced error which are considered to be the main source of ranging error in LoS/DDP class.

In NUDP class of receiver location, $\lambda_i = 0$ and $P_{tot} > \eta_2$ but $P_{DP} < \eta_1$, resulting in $\tau_{FDP} = \underset{k \neq 1}{\tau_{1,k}}$ which indicates that the DP component is not within the dynamic range of the system and hence can not be detected but a neighboring path from the first cluster was detected as the FDP. Consequently, $\varepsilon = (\tau_{FDP} - \tau_{1,1}) \times c$ is in the order of ray arrival rate defined in the CIR system model presented in Eqn. 1.1. It has been shown that NUDP ranging errors are small and occur in small bursts [Pah06]. The gradual weakening of the DP component due to loss of power

from reflection and transmission mechanisms suggests that by moving further from transmitter at a certain break-point distance the power of the DP component, P_{DP}, falls below the detection threshold, i.e. not within the dynamic range of the system, and consequently the receiver exits DDP condition and enters NUDP condition. Similar to DDP class of receiver location, in NUDP regions the error is given by

$$f_{\boldsymbol{\varepsilon}_{NUDP}}(\varepsilon) = f^{\mathbf{M+NUDP}}(\varepsilon) \tag{3.3}$$

where $f^{\mathbf{M+NUDP}}$ indicates that multipath and loss of DP component are the main sources of ranging error.

In contrary to the above states, in SUDP class of receiver locations the attenuation of the multipath components results in very weak paths regarding the first cluster, i.e. channel profiles with *soft onset* CIR [Mol06, Kar07], which shifts the strongest component to the middle of the CIR. Consequently, for SUDP class of receiver location $P_{DP} < \eta_1$ and $P_{tot} > \eta_2$ but $\lambda_i = 1$ denoting that the receiver location is blocked by a metallic object. In such scenarios $\tau_{FDP} = \underset{i \neq 1}{\tau_{i,j}}$, indicating the blockage of the first cluster and that the second cluster is detected instead, resulting in FDP component being either the first or one of the following paths of the second cluster. Consequently, $\varepsilon = (\tau_{FDP} - \tau_{1,1}) \times c$ is in the order of cluster arrival rate defined in the CIR system model presented in Eqn. 1.1. Results of extensive wideband and UWB measurement and simulation in indoor environments confirm the occurrence of unexpected large ranging errors associated with SUDP condition observed in indoor environment [Ala06a, Ala06b, Pah98, Den04]. For SUDP regions,

$$f_{\boldsymbol{\varepsilon}_{SUDP}}(\varepsilon) = f^{\mathbf{M+NUDP+SUDP}}(\varepsilon) \tag{3.4}$$

where $f^{\mathbf{M+NUDP+SUDP}}$ indicates that multipath, loss of DP component, and block-

age are the main sources of ranging error.

Finally, for the last class of receiver location, which is referred to as NC conditions, $P_{tot} < \eta_2$ in which communication is not feasible and the receiver is out of range. Assuming that the mobile terminal resides in one of the UDP areas, by moving further from the transmitter, at a certain break-point distance, the receiver transitions from UDP condition to NC condition. In NC condition the range estimate is not available and ranging error is undefined.

Figure 3.3 illustrates the areas associated with the four classes of ranging error in the third floor of the $AKLabs$ at WPI for the specified location of the transmitter. To determine the areas we have used the measurement calibrated RT software previously used in [Ala06a] to generate comprehensive samples of CIR for different locations of the receiver in the building. The class of ranging error associated with each receiver location is defined according to P_{DP} and P_{tot} given by Eqn. 3.1 and physical layout of the building, represented by λ_i. Increasing the distance of the antenna pair in indoor environment increases the probability of blockage of the DP component. In NUDP class of receiver location, although the receiver location is not blocked by metallic objects, P_{DP} falls below the detection threshold, η_1, and hence receiver makes erroneous estimate of the distance of the antenna pair. In SUDP class of receiver location, blockage of the DP component and its adjacent paths with a metallic object attenuates the DP component and its adjacent paths significantly and hence receiver makes an unexpectedly large ranging error by detecting another reflected path.

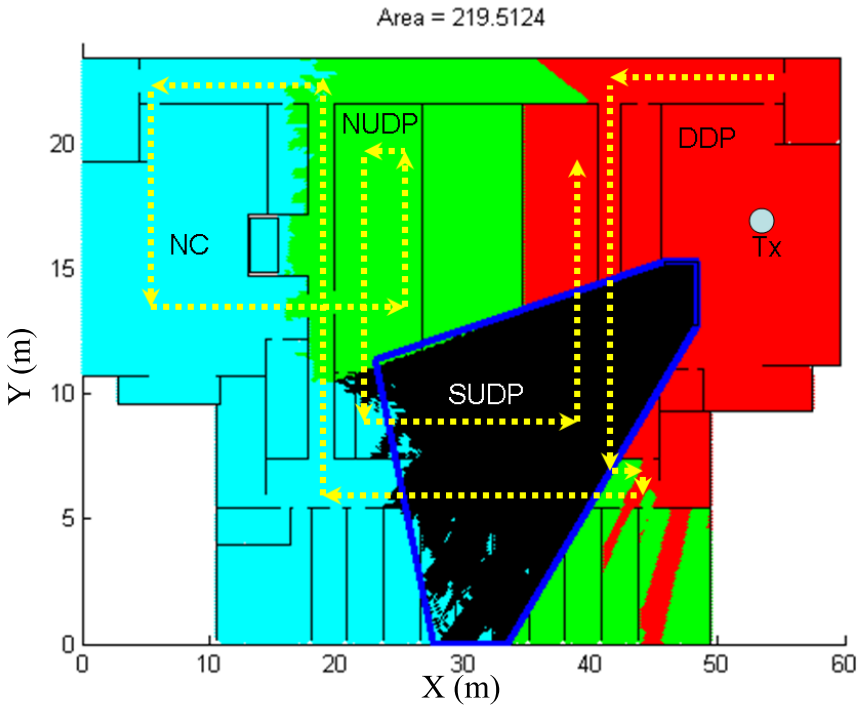

Figure 3.3: Indoor receiver classification simulation for a sample location of the transmitter. The location of the metallic chamber close to the transmitter causes lots of SUDP receiver locations.

3.3 Ranging Error Classification Based on Distance

The receiver location classification described above is very difficult to obtain as it is computationally tedious and time-consuming. Alternatively, to avoid the extensive simulation and/or measurement to categorize the receiver locations in a building, we have developed an infrastructure-distance-measurement-based model (IDM) based on the realistic path-loss models for indoor environment [Ala06a] to represent different classes of receiver location and ranging errors associated with them.

3.3.1 Infrastructure-distance-measurement-based model (IDM)

Assuming the knowledge of blockage condition, $\lambda_i(r)$, for each receiver location, the proposed model can be represented as following

$$\xi_i(r) = \begin{cases} DDP & : d < d_1 \bigcap \lambda_i(r) = 0 \\ NUDP & : d_1 < d < d_2 \bigcap \lambda_i(r) = 0 \\ SUDP & : d < d_3 \bigcap \lambda_i(r) = 1 \\ NC & : \begin{cases} d > d_2 \bigcap \lambda_i(r) = 0 \\ d > d_3 \bigcap \lambda_i(r) = 1 \end{cases} \end{cases} \tag{3.5}$$

where $\xi_i(r)$ represents the class of receiver location and d_1, d_2, and d_3 represent the distance break-point of DDP and NUDP regions, the distance break-point of NUDP and NC regions, and the distance break-point of SUDP and NC regions, respectively. The sample break-points are determined by extensive frequency measurements, sweeping frequency of $3 - 8\,GHz$ with a sampling frequency of $1\,MHz$, conducted in the sample indoor environment [Ala05] to be around $18\,m$, $35\,m$, and $30m$, respectively. The measurement setup has a sensitivity of $-80dBm$ representing the detection threshold [Als04, Ala06a]. Altering the sensitivity of the measurement system, i.e. the detection threshold and dynamic range of the system, as well as other parameters of the measurement will cause modifications in determination of the break-point distances [Guv07a]. However, such modifications are not in the scope of this research and the reported break-point distances are determined using the above measurement setup.

To verify the validity of the proposed model, i.e. IDM realization, we can compare it with the result of receiver location classification using RT simulation. Very

close agreement of RT simulation and the IDM realization of different categories is illustrated in Fig. 3.4, which demonstrates the validity of the proposed IDM realization. The above model, however, represents the static classification of the receiver locations in indoor environments.

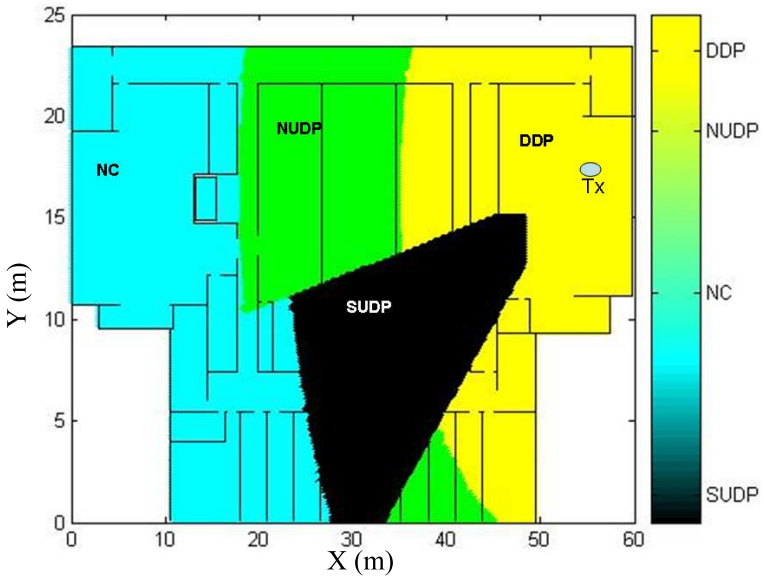

Figure 3.4: Indoor receiver classification for the same location of the transmitter based on infrastructure-distance-measurement (IDM) model. The pattern of the areas associated with each class is very similar to those obtained from power based classification

As a mobile client randomly travels in indoor environment it crosses over different states and hence the ranging error associated with the mobile client changes drastically. The area of each state is directly related to the state probabilities, i.e. probability of residing in a specific state for a random mobile client. These state probabilities become very important for cooperative localization systems as they are

related to the node density of the system. We define the state probabilities as below;

$$P_r^z = P_r(\xi_i \in z) = \frac{\int\int_{\xi_i \in z} dxdy}{\int\int_{\xi_i \in M} dxdy} \tag{3.6}$$

in which M represents the union set of receiver locations and $z \in \{DDP, NUDP, SUDP, NC\}$ represents the desired state.

The state probabilities, in general, are not easy to find analytically as they vary with the change of transmitter location and shape and details of the building. However, statistics of the state probabilities are easy to find and model by altering the location of the transmitter and modeling the result of simulation. Using Eqn. 3.5 to categorize the receiver locations into DDP, NUDP, SUDP, and NC for the same indoor environment described in Fig. 3.3, we were able to compare the average SUDP state probability of the IDM realization and wideband measurement previously conducted in the same scenario. We observed that on average a random mobile client would expect to be in SUDP condition with probability of 8.9% according to IDM realization which is close to the reported value of 7.4% obtained from wideband measurement [Ala06a, Hei07d].

Each state probability can be considered as a random variable. Knowing the statistics of the state probability for a certain state, we are able to define the CDF of the state probability. It follows as

$$F_{P_{SUDP}}(p_1) = P\{P_{SUDP} < p_1\} \tag{3.7}$$

which discloses the receiver locations in which their state probability is less than a certain value p_1. Finally, the probability distribution function (PDF) can be defined as $f_{P_{SUDP}}(p_1) = \frac{\partial F_{P_{SUDP}}(p_1)}{\partial p_1}$. It is worth mentioning that $f_{P_{SUDP}}$ can be considered

as a random variable modeling the distribution of SUDP state probability, which itself is limited to the interval $[0\,,1)$. Therefore, the outcome of such distribution should be truncated to remain in $[0\,,1)$ to ensure that state probabilities are within their limits.

3.4 Statistical Behavior of Ranging Error in Each Class

Modeling the ranging error observed in different classes of receiver location in indoor localization is the major challenge in the analysis of an indoor positioning system. It is a common belief that ranging errors associated with LoS state, and equivalently DDP state, can be modeled with Gaussian distribution [Ala06b]. However, in NLoS conditions, and equivalently NUDP and SUDP states, different distributions consisting of Gaussian [Ala06b], exponential [Mor07, Gha05], log-normal [Jo06, Als07b] and mixture of exponential and Gaussian [Ala03, Den04] have been used for modeling the ranging error. Comprehensive UWB measurement and modeling of ranging errors in NLoS can be found in [Als07a] which reports a heavy tail distribution for ranging errors observed in UDP conditions. In this section we provide precise distribution for modeling the ranging error associated with each state. For each class of receiver location, we provide the histogram and if necessary probability plot of the error for visualization of the goodness-of-fit.

Figure 3.5(a) compares the CDF of the observed ranging error for DDP class of receiver location with its respective normal distribution fit. In DDP class of receiver location $\lambda_i = 0$ and using Eqn. 3.2 leads us to

$$f_{\boldsymbol{\varepsilon}_{DDP}}(\boldsymbol{\varepsilon}) = f^{\mathbf{M}}(\boldsymbol{\varepsilon}) = \mathcal{N}(\mu_{DDP}, \sigma_{DDP}) \tag{3.8}$$

Similarly, Fig. 3.5(b) compares the CDF of NUDP ranging error with its normal distribution fit. It can be noticed that although the CDF of ranging error is similar in cases of DDP and NUDP ranging error, the NUDP ranging errors tend to be more positive. Therefore, the distribution of ranging error can be represented as

$$f_{\boldsymbol{\varepsilon}_{NUDP}}(\boldsymbol{\varepsilon}) = f^{\mathbf{M+NUDP}}(\boldsymbol{\varepsilon}) = \mathcal{N}(\mu_{NUDP}, \sigma_{NUDP}) \tag{3.9}$$

where $\mu_{NUDP} > \mu_{DDP}$.

Our explanations to such observation is the presence of propagation delay and the larger separation of the antenna pair, which allows multipath and loss of the DP to be more effective. Table 3.1 provides the statistics of ranging errors observed in such classes of receiver location.

Table 3.1: Parameters of Normal Distribution Ranging Error of DDP and NUDP Classes

	Normal Distribution	
DDP Ranging Error	μ_{DDP}	σ_{DDP}
	0.0135	0.0105
NUDP Ranging Error	μ_{NUDP}	σ_{NUDP}
	0.1063	0.0239

In SUDP class of receiver locations, the ranging errors are following a heavy tailed distribution which can not be modeled with a Gaussian distribution. It can be observed that in such scenarios, infrastructure of the indoor environment commonly obstructs the DP component and causes unexpected larger ranging errors. As a result, the statistical characteristics of the ranging error in SUDP class exhibits a heavy tail in its distribution function. This heavy tail phenomenon has been reported and modeled in the literature as in [Ala03, Den04] the observed ranging error was modeled as a combination of a Gaussian distribution and an exponential distri-

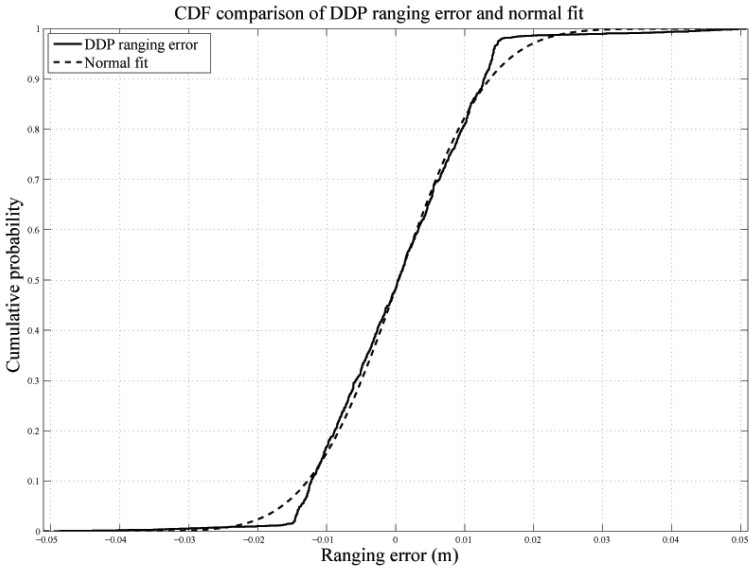

(a) DDP

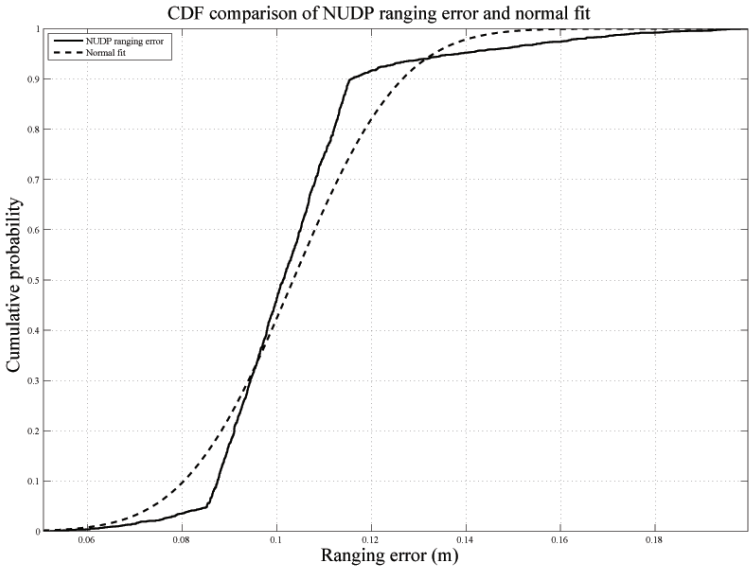

(b) NUDP

Figure 3.5: Distribution modeling of the ranging error with normal distribution for a) DDP class of receiver locations and b) NUDP class of receiver locations

bution and [Jo06, Als07b] model the ranging error with a log-normal distribution.

Traditionally, log-normal, Weibull, and generalized extreme value (GEV) distributions are used to model the phenomena with heavy tail. The GEV class of distributions, with three degrees of freedom, is applied to model the extreme events in hydrology, climatology, and finance [Mar05].

Table 3.2 summarizes the results of the $K-S$ test and χ^2 test for SUDP class for different distributions. It can be observed that from the distributions offered to model the SUDP ranging error, normal distribution fails both $K-S$ and χ^2 hypothesis test while the rest of distributions pass the hypothesis tests.

Figure 3.6(a) compares the PDF of the ranging error for SUDP state with its respective normal, Weibull, GEV, and log-normal fits. Figure 3.6(b) illustrates the probability plot and closeness of the fits for SUDP class. From Table 3.2 it can be also observed that GEV distribution's passing rate is the highest amongst all distributions, which is expected as GEV models the heavy tail phenomenon with three degrees of freedom compared with two degrees of freedom of log-normal and Weibull distributions. Similar observations have been reported in [Als07a] using UWB measurements conducted in different indoor environments. Quantitatively, for the selection of the best distribution, we refer to the Akaike's information criterion [Bur02], represented in Table 3.2, by forming the log-likelihood function of the

Table 3.2: Passing Rate of $K-S$ and Statistical Value of χ^2 Hypothesis Tests at 5% Significance Level Ranging Error for SUDP Class

Distribution	SUDP		
	$K-S$	χ^2	$Akaike\,Weight$
Normal	78.71%	50.84%	0
Weibull	85.02%	74.91%	8.6×10^{-10}
GEV	96.86%	85.31%	1
Log-normal	87.82%	67.11%	6.4×10^{-17}

candidate distribution and penalizing each distribution with its respective number of parameters to be estimated. Following the methodology described in [Bur02], the Akaike weights can be used to determine the best model which fits the empirical data. The higher values of Akaike weight represent more plausible distribution and the highest value can be associated with the best model. The result of such experiment also confirms the result of probability plot and suggests that the best distribution to model the ranging error associated with SUDP class is in fact a GEV distribution, since all the other Akaike weights are practically zero.

The GEV distribution is defined as

$$f(x|\kappa_{SUDP},\mu_{SUDP},\sigma_{SUDP}) = (\frac{1}{\sigma_{SUDP}})\exp(-(1+\kappa_{SUDP}\frac{(x-\mu_{SUDP})}{\sigma_{SUDP}})^{-\frac{1}{\kappa_{SUDP}}}) \cdot(1+\kappa_{SUDP}\frac{(x-\mu_{SUDP})}{\sigma_{SUDP}})^{-1-\frac{1}{\kappa_{SUDP}}} \tag{3.10}$$

for $1+\kappa_{SUDP}\frac{(x-\mu_{SUDP})}{\sigma_{SUDP}} > 0$; where μ_{SUDP} is defined as the location parameter, σ_{SUDP} is defined as the scale parameter, and κ_{SUDP} is the shape parameter. The value of κ_{SUDP} defines the type of the GEV distribution; $\kappa_{SUDP} = 0$ is associated with type I, also known as Gumbel, $\kappa_{SUDP} < 0$ is associated with type II, which is also correspondent to Weibull. However, the type III, associated with $\kappa_{SUDP} > 0$, which is known as Frechet type, best models the heavy tail observed in ranging errors associated with SUDP class of receive location. Parameters of the GEV distribution modeling the ranging error observed in SUDP class of receiver location are reported in Table 3.3. Evidentally, it can be noted that the presented GEV distribution for ranging errors observed in SUDP class of receiver location belongs to the third

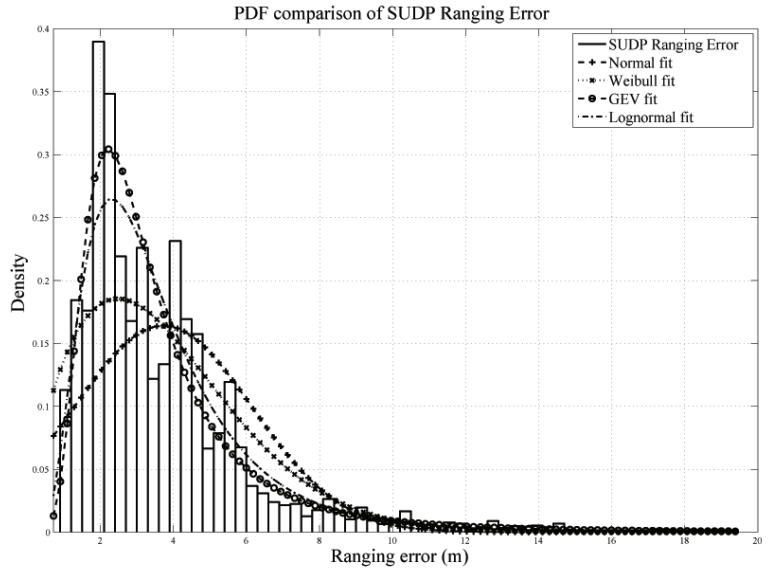

(a) Histogram

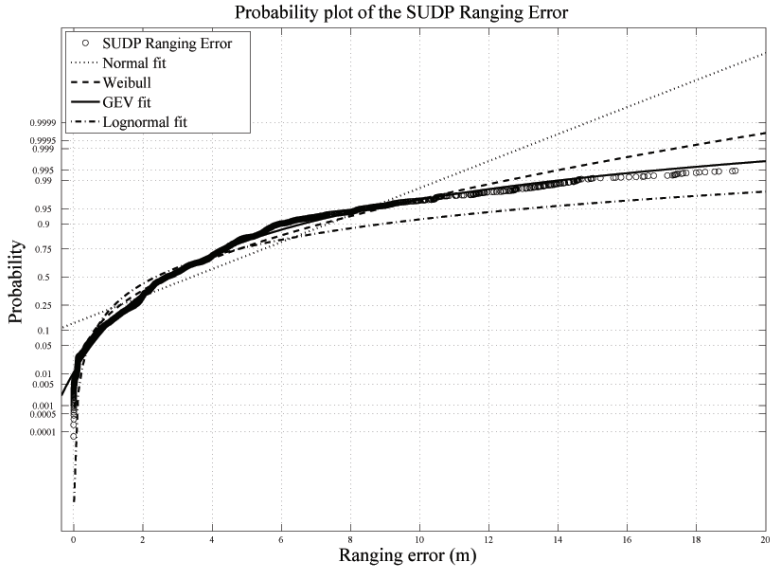

(b) Probability plot

Figure 3.6: Statistical analysis of ranging error observed in SUDP class of receiver location, a) Histogram of ranging error and b) Probability plot of ranging error vs. different distributions. It can be concluded that GEV distribution best models the ranging error observed in such class of receiver location

category with its respective $\kappa_{SUDP} > 0$. Hence,

$$f_{\boldsymbol{\varepsilon}_{SUDP}}(\varepsilon) = f^{\mathbf{M+NUDP+SUDP}}(\varepsilon) = \mathcal{GEV}(\mu_{SUDP}, \sigma_{SUDP}, \kappa_{SUDP}) \tag{3.11}$$

where $\kappa_{SUDP} > 0$.

Table 3.3: Parameter of GEV Distribution Ranging Error of SUDP Class

	GEV Distribution		
	μ_{SUDP}	σ_{SUDP}	κ_{SUDP}
SUDP Ranging Error	2.5218	1.2844	0.4198

Next we relate the statistics of the ranging errors observed in different classes of receiver locations to the parameters of the cluster model defined in IEEE *P*802.15.3, Eqn. 1.2. It is important to notice that the small ranging error values reported for DDP and NUDP classes enables the user to use the channel models reported in IEEE *P*802.15.3 [Cas02, Mol03, Mol05] for ranging purposes while larger ranging errors observed in SUDP region prevents such model to be used for ranging purposes.

3.4.1 Improvement over IEEE 802.15.3 recommended model

IEEE *P*802.15.3 assumes, through Eqn. 1.2, to be the basic discrete model of the wireless channel in indoor environment. Previously, results of indirect channel models similar to IEEE *P*802.15.3 and direct channel models were compared to illustrate the inefficiency of indirect models to be used for localization purposes [Ala06a]. Although indirect models are very advantageous for telecommunication purposes but they do not provide a close approximation for the ToA of DP which is used in ToA based localization systems. In this section, we suggest minor improvements over the specific model of IEEE *P*802.15.3 to adjust such model to localization problem.

From our observations, in DDP class, since the DP is easily detected, ranging error is at its minimum. Although it is shown that in DDP state multipath error exists [Ala06b], for wideband systems the multipath error is on the order of few centimeters, which is acceptable for cooperative localization and wireless sensor networks. In NUDP class, we hypothesize that the first cluster is detected; however, the power of DP is not within the dynamic range of the receiver which results in detecting the second path (or any of the following paths after DP) as the FDP. Therefore, the error should be approximated with the ray arrival rate in the IEEE $P802.15.3$ model. It is reported that the ray arrival rate is in the order of $\theta = 2.1(\frac{1}{nsec})$. By detecting the following paths with the specified arrival rate, an error of $(\frac{1}{\theta} \times 10^{-9} \times c = 0.15)$ meters is expected which is in agreement with the average observed error in the NUDP state and reported in Table 3.1.

However, In the SUDP class, which is characterized by extreme NLoS condition in IEEE $P802.15.3$, blockage of the first cluster results in detecting a path from the next cluster and hence the receiver makes an unexpectedly large error. IEEE $P802.15.3$ model provides the cluster arrival rate of $\Theta = 0.0667(\frac{1}{nsec})$; hence algorithm makes a ranging error in the order of $(\frac{1}{\Theta} \times 10^{-9} \times c = 4.5)\, m$. The mean of the GEV distribution is given by $\mu_{SUDP} - \frac{\sigma_{SUDP}}{\kappa_{SUDP}} + \frac{\sigma_{SUDP}}{\kappa_{SUDP}} \times \Gamma(1 - \kappa_{SUDP})$, where $\Gamma(x)$ represents the gamma function. Substituting the reported parameters of SUDP ranging error yields an average of $4.31\, m$, which, on average, is in agreement with the assumption of loss of the first cluster. Based on this analysis we recommend that if IEEE $P802.15.3$ model is being used for ToA-based ranging purposes in extreme NLoS conditions, slight modifications are necessary for acquiring tangible estimate of the ranging error observed in such conditions.

Chapter 4

Modeling of the Dynamic Behavior of Direct Path

As seen in the previous chapter, there exist different classes of receiver locations with different ranging error characteristics. The subsequent classes range from DDP in which the DP component is detectable and ranging error is negligible to SUDP where the DP component is blocked by a macro-metallic object and hence the ranging error is unexpectedly large. There also exist an NC class in which the ranging error is not defined. In this chapter we discuss the details of modeling of the dynamic behavior of the DP component as it moves amongst different classes. The model starts with associating each class of receiver location with a state of Markov chain. The next step is to derive the parameters of the Markov model analytically using the infrastructure of the floor plan. Then we validate the model with experimental results by letting a mobile terminal traveling in the same indoor environment according to a *random walk* scenario which covers the entire floor plan and determining the parameters of the simulation of the Markov model. After modeling the dynamic behavior of the DP component and its class we assign realistic ranging error distribution models to

receiver locations within a same state and compare the results of the Markov model with ranging error distributions to the results of *random walk* simulations. Section 4.1 of this chapter introduces our approach to modeling the dynamic behavior of ToA ranging errors observed in indoor environment. Section 4.2 discusses the spatial characteristics of ToA ranging errors and dependence of current value of ToA ranging error to previous ranging errors within a certain state. Section 4.3 describes the results of the modeling the dynamic behavior of ToA ranging error and verifies the results with real-time simulation of mobile terminal randomly walking in the sample indoor environment.

4.1 Dynamic Modeling of the Behavior of Class of Receiver Location using Markov Chain

A random mobile client in an indoor environment experiences switching among different classes of ranging error, back and forth, as it keeps moving. Such spatial correlation and change of class can easily be modeled with Markov chains.

4.1.1 Ranging states of the Markov model

As mobile client randomly travels in the building, as shown in Fig. 3.3, and depending on the region of movement, it experiences different classes of ranging errors. Using the four classes of ranging error observed in separate areas of an indoor environment, we can construct a four-state first-degree Markov model to represent the dynamic behavior of ranging error observed by the mobile user. Random movement of the mobile user results in change of its observed class of ranging error, with particular probabilities. The general Markov model representation for indoor positioning is described in Fig. 4.1. At a given time mobile user observes certain error class

and as it moves along there are certain probabilities that it may change its class of ranging error.

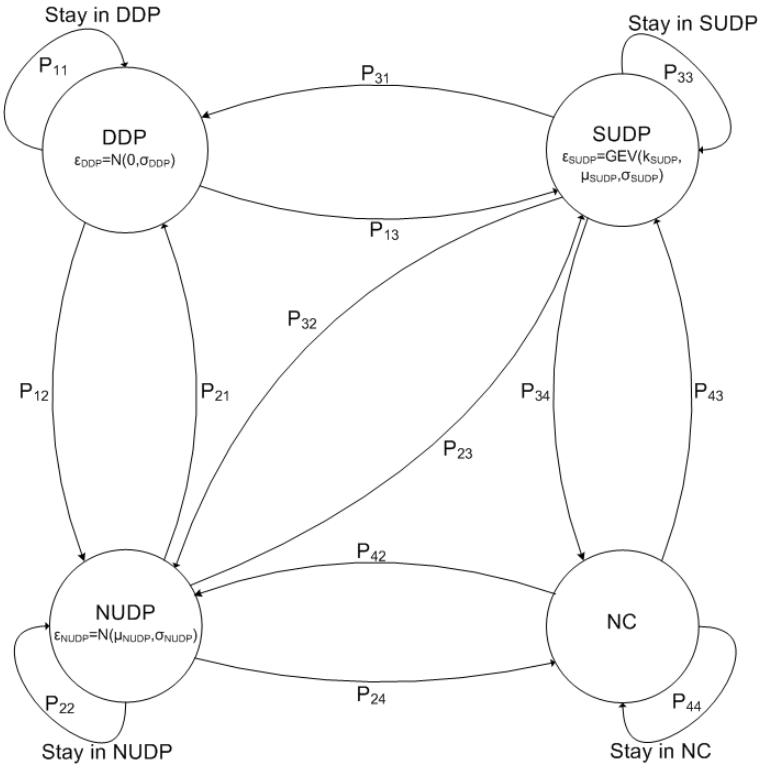

Figure 4.1: Markov model presented for dynamic behavior of the ranging error in indoor localization

Let the current receiver location, $\xi_i(r)$ in 3.5, embed the state of the mobile terminal, ω_i, where ω_i is defined over a discrete set Z consisting of four different receiver locations classes or states, $Z = \{DDP, NUDP, SUDP, NC\}$. The state of the mobile client movement within a 2D space in an indoor environment can be modeled with a Markov chain $\Omega_{0:i} = \{\omega_0, \ldots, \omega_i\}$ which can be generated by $\omega_i \sim \mathcal{MC}(\pi^{(\omega)}, \bar{\mathbf{P}}^{(\omega)})$ with initial-state PDF $\pi^{(\omega)} = \bar{p}\{\omega_0\}$. The initial-state PDF, $\pi^{(\omega)}$, can then be related to the state probabilities, and the average transition probabilities $\bar{\mathbf{P}}^{(\omega)} = \bar{p}_{i,j}^{(\omega)}$.

Following the methodology described in [Hei06, LG94], transition probabilities

are defined as the rate of switching between Markov states or dwell time of the mobile terminal in a state, i.e. staying in the same state, accordingly, and can be represented as

$$\bar{\mathbf{P}}^{(\omega)} = \begin{bmatrix} \bar{p}_{11}^{(\omega)} & \bar{p}_{12}^{(\omega)} & \bar{p}_{13}^{(\omega)} & \bar{p}_{14}^{(\omega)} \\ \bar{p}_{21}^{(\omega)} & \bar{p}_{22}^{(\omega)} & \bar{p}_{23}^{(\omega)} & \bar{p}_{24}^{(\omega)} \\ \bar{p}_{31}^{(\omega)} & \bar{p}_{32}^{(\omega)} & \bar{p}_{33}^{(\omega)} & \bar{p}_{34}^{(\omega)} \\ \bar{p}_{41}^{(\omega)} & \bar{p}_{42}^{(\omega)} & \bar{p}_{43}^{(\omega)} & \bar{p}_{44}^{(\omega)} \end{bmatrix} \tag{4.1}$$

where $\bar{p}_{i,j}^{(\omega)}$ is defined as the average transition probability from the state i to the state j, illustrated in Fig. 3. These average transition probabilities can then be obtained using the following

$$\bar{p}_{i,j}^{(\omega)} = \bar{p}(\omega_k = j | \omega_{k-1} = i) \tag{4.2}$$

From Fig. 4.1, it can be concluded that transition from DDP state to NC state is only possible through one the UDP states, so the resulting transition probabilities are set to zero, accordingly.

4.1.2 Average transition probabilities

Intuitively, the transition probability, i.e. crossing rate between two states, is a function of the area of the states and the length of the boundary of the two states. Previous studies were mainly based on the statistics of such transitions. However, in this section we present the details of obtaining the transition probabilities by discretizing the continuous problem, i.e. forming a grid of receiver locations in the regions. Assuming that at time $t = t_k$ the mobile client is located at one of the grid points, then at $t = t_{k+1}$ the mobile client travels to one of the adjacent grid points. Let Δ represent grid size and $T = t_{k+1} - t_k$ represent the sampling time;

thus, $\Delta = v \times T$ where v represents the velocity of the mobile client. Furthermore, let α_c represent the crossing rate of the system which depends on the spatial pattern of movements. In our discrete model for indoor movements, assuming the walls are either horizontal or vertical, a mobile can only move in four directions. Assuming absolute randomness in the movement of the mobile client results in probability of crossing rate of $\alpha_c = \frac{1}{4}$ and staying in the same region with probability of $1 - \alpha_c$ as Fig. 4.2 suggests. The average probability of cross can then be obtained as

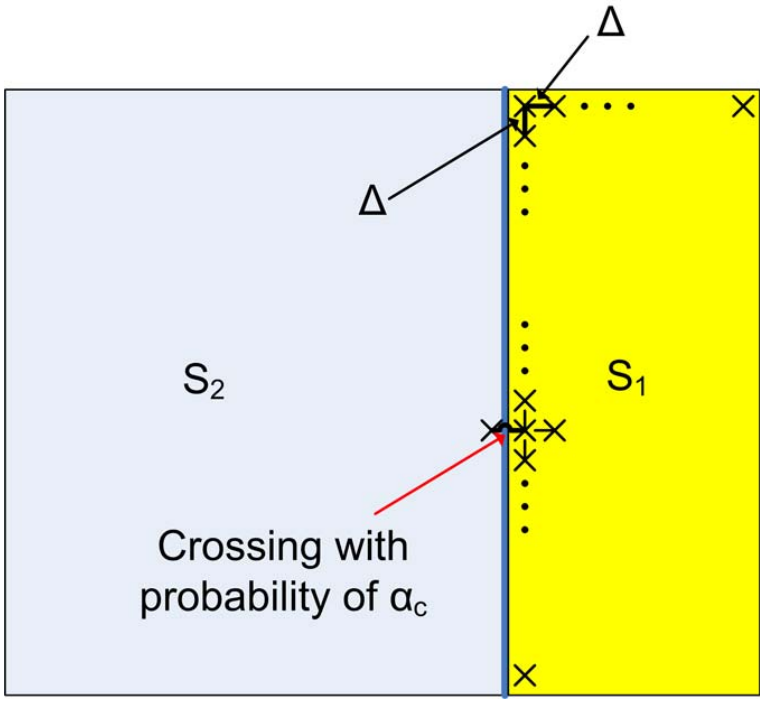

Figure 4.2: Crossing rate a random mobile client from one Markov state to another Markov state

$$\bar{p}_{12} = \frac{\alpha_c \times \frac{l}{\Delta} + 0 \times (\frac{S_1}{\Delta^2} - \frac{l}{\Delta})}{\frac{S_1}{\Delta^2}} \tag{4.3}$$

where l represents the boundary length of the two regions and S_1 represents the area of first region. Simplifying Eqn. 4.3 results in

$$\bar{p}_{12} = \alpha_c \times \frac{l \times \Delta}{S_1} = \alpha_c \times \frac{l \times vT}{S_1} \tag{4.4}$$

Generalizing the results of the previous two-state, i.e. two region, random movement to our Markov model with four states, we can obtain the transition probability matrix as

$$\bar{\mathbf{P}} = \begin{bmatrix} Q_1 & \alpha_c \frac{l_{12} \times vT}{S_1} & \alpha_c \frac{l_{13} \times vT}{S_1} & \alpha_c \frac{l_{14} \times vT}{S_1} \\ \alpha_c \frac{l_{21} \times vT}{S_2} & Q_2 & \alpha_c \frac{l_{23} \times vT}{S_2} & \alpha_c \frac{l_{24} \times vT}{S_2} \\ \alpha_c \frac{l_{31} \times vT}{S_3} & \alpha_c \frac{l_{32} \times vT}{S_3} & Q_3 & \alpha_c \frac{l_{34} \times vT}{S_3} \\ \alpha_c \frac{l_{41} \times vT}{S_4} & \alpha_c \frac{l_{42} \times vT}{S_4} & \alpha_c \frac{l_{43} \times vT}{S_4} & Q_4 \end{bmatrix} \tag{4.5}$$

where $l_{ij} = l_{ji}$ represents the boundary length between i^{th} and j^{th} regions, S_k represent the area of the k^{th} region, and $Q_1 = 1 - \alpha_c \frac{(l_{12}+l_{13}+l_{14}) \times vT}{S_1}$, $Q_2 = 1 - \alpha_c \frac{(l_{21}+l_{23}+l_{24}) \times vT}{S_2}$, $Q_3 = 1 - \alpha_c \frac{(l_{31}+l_{32}+l_{34}) \times vT}{S_3}$, and $Q_4 = 1 - \alpha_c \frac{(l_{41}+l_{42}+l_{43}) \times vT}{S_4}$. Combining α_c and vT parameters, we can obtain

$$\bar{\mathbf{P}} = \begin{bmatrix} \tilde{Q}_1 & \beta \frac{l_{12}}{S_1} & \beta \frac{l_{13}}{S_1} & \beta \frac{l_{14}}{S_1} \\ \beta \frac{l_{12}}{S_2} & \tilde{Q}_2 & \beta \frac{l_{23}}{S_2} & \beta \frac{l_{24}}{S_2} \\ \beta \frac{l_{13}}{S_3} & \beta \frac{l_{23}}{S_3} & \tilde{Q}_3 & \beta \frac{l_{34}}{S_3} \\ \beta \frac{l_{14}}{S_4} & \beta \frac{l_{24}}{S_4} & \beta \frac{l_{34}}{S_4} & \tilde{Q}_4 \end{bmatrix} \tag{4.6}$$

where $\tilde{Q}_1 = 1 - \beta \frac{(l_{12}+l_{13}+l_{14})}{S_1}$, $\tilde{Q}_2 = 1 - \beta \frac{(l_{21}+l_{23}+l_{24})}{S_2}$, $\tilde{Q}_3 = 1 - \beta \frac{(l_{31}+l_{32}+l_{34})}{S_3}$, and $\tilde{Q}_4 = 1 - \beta \frac{(l_{41}+l_{42}+l_{43})}{S_4}$ and $\beta = \alpha_c \times vT$ represents both the velocity of the mobile client and probability of crossing among the regions and the sole parameter to be determined. In the case of indoor positioning the DDP and NC regions are not connected directly resulting in $l_{14} = l_{41} = 0$, which confirms the absent of the link

between DDP and NC state in Fig. 4.1.

4.1.3 Exponential modeling of dwell time

As discussed in [LG94], the Markov property reveals the following regarding the eigenvectors of $\bar{\mathbf{P}}$

$$\varphi_1 = 1, |\varphi_i| < 1 \Rightarrow \bar{\mathbf{P}}\boldsymbol{v}_i = \varphi_i \boldsymbol{v}_i \tag{4.7}$$

where φ_i represents the eigenvalues of $\bar{\mathbf{P}}$ and $\boldsymbol{v}_i$ represents the eigenvectors associated with φ_i. For the presented Markov model, $\boldsymbol{v}_i = [e_1 \quad e_2 \quad e_3 \quad e_4]$ and $\sum e_i = 1$ representing the normalized eigenvector. We concentrate on the steady state probabilities as the Markov chain settles into stationary behavior after the process has been running for a long time. When this occurs we have

$$\bar{\mathbf{P}}\boldsymbol{v}_1 = \boldsymbol{v}_1 \tag{4.8}$$

which represents the eigenvector associated with $\varphi_1 = 1$ and determines the expected average dwell time in each state. In the dynamic case, assuming homogeneous transition probabilities in continuous time, i.e. $P[B(s+t) = j|B(s) = i] = P[B(t) = j|B(0) = i] = p_{ij}(T_n)$, we convert the discrete Markov chain in Eqn. 4.6 to an equivalent continuous time Markov chain to extract the dwell time distributions of each state. The memoryless distribution of the dwell time in a certain state can then only be described by an exponential random variable $p[\mathrm{T} > t] = e^{-\gamma_i t}$ [LG94]. Similar to methodology described in [LG94], γ_is can be determined by solving the respective Chapman-Kolmogorov equation and equating γ_i to $-\frac{1}{\psi_{ii}}$, with ψ being the solution of Chapman-Kolmogorov equation. The solution for the Chapman-

Kolmogorov equation for the steady state $\bar{\mathbf{P}}$ results in

$$\psi = \begin{bmatrix} \hat{Q}_1 & \beta \times \frac{l_{12}}{S_1} & \beta \times \frac{l_{13}}{S_1} & \beta \times \frac{l_{14}}{S_1} \\ \beta \times \frac{l_{12}}{S_2} & \hat{Q}_2 & \beta \times \frac{l_{23}}{S_2} & \beta \times \frac{l_{24}}{S_2} \\ \beta \times \frac{l_{13}}{S_3} & \beta \times \frac{l_{23}}{S_3} & \hat{Q}_3 & \beta \times \frac{l_{34}}{S_3} \\ \beta \times \frac{l_{14}}{S_4} & \beta \times \frac{l_{24}}{S_4} & \beta \times \frac{l_{34}}{S_4} & \hat{Q}_4 \end{bmatrix} \tag{4.9}$$

where $\hat{Q}_1 = -\beta \times \frac{(l_{12}+l_{13}+l_{14})}{S_1}$, $\hat{Q}_2 = -\beta \times \frac{(l_{12}+l_{23}+l_{24})}{S_2}$, $\hat{Q}_3 = -\beta \times \frac{(l_{13}+l_{23}+l_{34})}{S_3}$, $\hat{Q}_4 = -\beta \times \frac{(l_{14}+l_{24}+l_{34})}{S_4}$; which in the case of the presented Markov model leads to

$$[\gamma_1 \quad \gamma_2 \quad \gamma_3 \quad \gamma_4] = [\frac{S_1}{\beta(l_{12}+l_{13}+l_{14})} \quad \frac{S_2}{\beta(l_{12}+l_{23}+l_{24})} \quad \frac{S_3}{\beta(l_{13}+l_{23}+l_{34})} \quad \frac{S_4}{\beta(l_{14}+l_{24}+l_{34})}] \tag{4.10}$$

Determining exponential parameters allows us to simulate the average dwell time in each state and compare them with results of the empirical data.

4.1.4 Multivariate distribution modeling of the state probabilities

Intuitively, altering the location of the transmitter will change the state probabilities, for example, a transmitter location close to the obstructive metallic object will cause larger set of SUDP receiver locations. This illustrates that for a specified indoor environment altering the location of the transmitter changes the state probabilities. As a result, each state probability can be treated as a random variable.

The histogram of the state probabilities can then be modeled by a multivariate distribution, as the state probabilities are clearly not independent. In order to find the best distribution to model the state probabilities, we altered the location

of the transmitter in the floor plan of the building under study and investigated the histograms and probability plots of the state probabilities. As it is shown in the following section a practical choice for the multivariate distribution is Gaussian distribution which leads us to form a joint Gaussian distribution to model the state probabilities of the main three states. The fourth state can then be found deterministically as the sum of the state probabilities should equal unity. Therefore, we can start with a multivariate normal distribution to represent the state probabilities

$$f_{\mathbf{P}}(\mathbf{p}) = (2\pi)^{-\frac{3}{2}}|\mathbf{\Sigma}|^{-\frac{1}{2}} \exp(-\frac{1}{2}(\mathbf{p}-\bar{\boldsymbol{\mu}})^{\mathbb{T}}\mathbf{\Sigma}^{-1}(\mathbf{p}-\bar{\boldsymbol{\mu}})) \tag{4.11}$$

where $\mathbf{p} = [\bar{P}_r^{DDP} \quad \bar{P}_r^{NUDP} \quad \bar{P}_r^{SUDP}]$ represents the random vector containing the average state probability values, $\mathbf{\Sigma}$ and $\bar{\boldsymbol{\mu}}$ are the parameters of the joint distribution, and $\mathbb{T}$ represents the transpose of a vector. In order to extract the parameters of this multivariate normal distribution we used sample mean to approximate the mean as

$$\hat{\bar{\boldsymbol{\mu}}} = \frac{1}{n}\sum_{k=1}^{n} P_{r_k}^{z} \qquad\qquad z \in \{DDP, NUDP, SUDP\} \tag{4.12}$$

where $P_{r_k}^{z}$ represents the k^{th} observed state probability of the state z and n represents the total number of observations. The maximum likelihood estimator of the covariance matrix can then be defined as

$$\hat{\mathbf{\Sigma}} = (\frac{1}{n-1})\sum_{k=1}^{n}(\mathbf{P}_{\mathbf{k}}^{\mathbf{z}} - \hat{\bar{\boldsymbol{\mu}}})(\mathbf{P}_{\mathbf{k}}^{\mathbf{z}} - \hat{\bar{\boldsymbol{\mu}}})^{\mathbb{T}} \tag{4.13}$$

where $\hat{\bar{\boldsymbol{\mu}}}$ is the sample mean and $\mathbf{P}_{\mathbf{r_k}}^{\mathbf{z}} = [P_{r_k}^{DDP} \quad P_{r_k}^{NUDP} \quad P_{r_k}^{SUDP}]$ represents the k^{th} state probability observation and n represents the total number of observation.

Now with the aid of Cholesky decomposition we provide a method for reconstructing the state probabilities in a typical indoor scenario. In communication

realm, Cholesky decomposition is used in synchronization and noise suppression [Poo97, Ben98]. Similar to [Say03], in order to regenerate these state probabilities one may pursue the following procedure. The first step is to decompose the covariance matrix using Cholesky decomposition method

$$AA^T = \hat{\mathbf{\Sigma}} \tag{4.14}$$

then we generate a vector of standard normal values $\mathbf{Z}$, and use the following

$$\breve{\mathbf{y}} = \hat{\boldsymbol{\mu}} + A\mathbf{Z} \tag{4.15}$$

where $\breve{\mathbf{y}} = [P_r^{DDP} \quad P_r^{NUDP} \quad P_r^{SUDP}]$ represents the generated values of state probabilities.

We refer to this method of extracting state probabilities as multivariate normal distribution model (MND) through out this paper.

4.2 Modeling of the Spatial Characteristics of Ranging Error within a State using Autocorrelation Properties

Next phase of the dynamic modeling of the behavior of ranging error is to model the spatial variations of ranging error within a certain state. Intuitively, a small step of the mobile terminal in one direction causes small changes to the value of the ranging error. Assuming that the mobile terminal is in SUDP state, a small step (in the order of spacing of the receiver locations or 13 cm) in any direction keeps the mobile terminal in SUDP state and varies the value of ranging error to a value

close to the previous observed value. To show this dependency, we have used the autocorrelation functions (ACF) of sample ranging error obtained from our scenario to illustrate the dependency of each ranging error to the previous observed ranging errors. Figure 4.3 illustrate the ACF of SUDP ranging error obtained from RT for our *random walk* scenario.

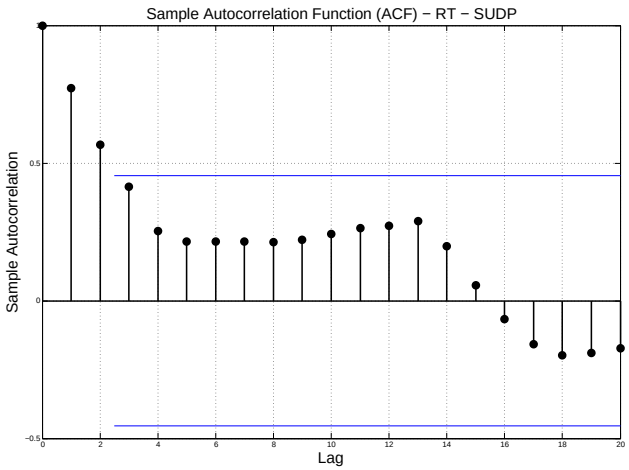

Figure 4.3: ACF of SUDP ranging error for the *random walk* scenario

It can be observed that the current value of ranging error is highly dependent on the previous values. We can model this dependency by filtering the results of ranging error so that

$$\varepsilon_i = \sum_{k=1}^{K} \varpi_{i-k} \times \varepsilon_{i-k} + \varpi \mathcal{D}(\varepsilon) \tag{4.16}$$

where $\mathcal{D}(\varepsilon)$ describes the distribution of the ranging error. Eqn. 4.16 clearly formulates the dependency of the new value of ranging error, ε_i, to the previous values of ranging error, ε_{i-k}, and distribution of ranging error in that state. Eqn. 4.16 in turn can be described by a k^{th} order linear filter. For simplicity, we consider a first

order filter in our discussion which can be described by

$$\varepsilon_i = \varpi \times \varepsilon_{i-1} + \sqrt{1 - \varpi^2} \times \mathcal{D}(\varepsilon) \tag{4.17}$$

where ϖ is the weight of each error contributor. If ϖ is small, the current value of ranging error is solely dependent on the distribution of ranging error in a certain state. On the other hand, large values of ϖ show the dependency of ranging error to the previous value of ranging error. The described filter in 4.17 can be realized by the means of first order exponential filter. Similar observations have been made for other states as well.

4.3 Simulation and Results

To completely model the dynamic behavior of ranging error observed in indoor environment, the transition probabilities of the Markov chain and statistics of ranging error for each Markov state are required. Thus, we started the process by categorizing the receiver locations according to Eqn. 3.5. Once the class of each receiver location and consequently the Markov state associated with it were identified, different distributions for statistics of ranging error observed in each class are introduced and modeled. Consequently, by collecting the area of each state and boundary length between each two states, the transition probabilities were acquired based on 4.6. Finally, we modeled the dynamic behavior of the ranging error by running the Markov chain and compared the results of analytical derivation obtained from section 4.1 to RT simulation of a dynamic scenario observed in the sample indoor environment. Furthermore, Altering the location of the transmitter and gathering the observed values for state probabilities of each state enabled us to model the statistics of state probabilities and initialize the Markov chain.

For the purpose of the simulation we considered the third floor of *AKLabs* at *WPI* as the floor plan of the building under study which resembles typical indoor office environment, yet a really harsh environment due to the existence of extensive blocks of metallic objects in the building. We formed a grid of receiver locations on the floor plan, approximately 14000 receiver locations, and generated their respective CIRs for different locations of the transmitter. In order to simulate the real-time channel profile of the CIR, a finite bandwidth raised-cosine filter can be used to extract the channel profile. For the purpose of ToA-based localization, it is shown that a minimum bandwidth of 200 MHz is sufficient for effectively resolving the multipath components and combating the multipath induced error [Pah06]. However, we used a 5 GHz raised-cosine filter to obtain a more realistic channel profile captured by an wideband measurement system. Post processing peak detection algorithm is then used to estimate τ_{FDP} and consequently form the error as discussed in section 1.2.

4.3.1 Markov model representation

The transition probabilities in Markov chain are analytically obtained using IDM realization, capturing the areas and boundary lengths and consequently using Eqn. 4.6. To validate the analytical derivation of transition probabilities of Markov chain, we consider a *random walk* process traveled by the mobile user in the third floor scenario of the *AKLabs* at *WPI*, shown in Fig. 3.3. In this *random walk* process, we calculate the number of state transitions and compare them to the analytical derivation in Eqn. 4.6.

4.3.1.1 Parameters of the Markov Chain

The generated 14000 CIRs for the different receiver locations in the building were categorized into DDP, NUDP, SUDP, and NC classes using Eqn. 3.5. The *random walk* was designed in a way to simulate a random mobile client traveling in indoor environment. It is assumed that the mobile client travels on the vertical or horizontal routes and continues its route until next node, i.e. door or hallway, and then randomly chooses the next node and travels towards it. This type of movement results in crossing the borders of states whenever mobile client is close to the boundary of two states yielding $\alpha_c \simeq 1$. The separation of the movement at each time instant, i.e. 1 sec, is 14.28 cm resulting in $vT \simeq \frac{1}{7}$. Furthermore, According to the IDM model, the parameters of the floor plan are

$$\begin{aligned}
&l_{12} = 17.07(m)\,, l_{13} = 28.48(m)\,, l_{14} = 0 \quad (m)\,, and \quad S_1 = 255.02(m^2)\\
&l_{21} = 17.07(m)\,, l_{23} = 23.34(m)\,, l_{24} = 14.00(m)\,, and \quad S_2 = 217.51(m^2)\\
&l_{31} = 28.48(m)\,, l_{32} = 23.34(m)\,, l_{34} = 16.70(m)\,, and \quad S_3 = 164.03(m^2)\\
&l_{41} = 0 \quad (m)\,, l_{42} = 14.00(m)\,, l_{43} = 16.70(m)\,, and \quad S_4 = 299.60(m^2)
\end{aligned} \tag{4.18}$$

which according to the analytical derivation of section 4.1 forms a transition probability matrix of

$$\mathbf{P} = \begin{bmatrix} 0.9744 & 0.0095 & 0.0159 & 0 \\ 0.0112 & 0.9642 & 0.0153 & 0.0091 \\ 0.0248 & 0.0203 & 0.9403 & 0.0145 \\ 0 & 0.0066 & 0.0079 & 0.9853 \end{bmatrix} \tag{4.19}$$

On the other hand, once the class of each receiver location was identified, we generated 7000 CIRs associated with the receiver locations of the *random walk* to empirically calculate the transition probability matrix of the Markov model by counting

the number of transitions from a certain state to another state. We repeated the steps for several different configurations of *random walk* inside the building under study and averaged the transition probabilities. The experiment yielded

$$\mathbf{P} = \begin{bmatrix} 0.9645 & 0.0085 & 0.027 & 0 \\ 0.0126 & 0.9501 & 0.0156 & 0.0217 \\ 0.0259 & 0.0179 & 0.9322 & 0.024 \\ 0 & 0.0108 & 0.0169 & 0.9723 \end{bmatrix} \tag{4.20}$$

which considering the fact that type of movement implies $\beta = \alpha \times vT \simeq \frac{1}{7}$ is very close to the analytical transition probability obtained from Eqn. 4.6 and reported in Eqn. 4.19. The differences between the two matrices are mainly due to the pattern of *random walk* as it only considers moving along hallways and in and out of offices. Note that $\bar{p}_{14} = \bar{p}_{41} = 0$ in both matrices confirms the absence of the link between DDP and NC classes. It is worth mentioning that altering the parameters of the simulation such as $\eta_{1,2}$, α, and v results in different transition probabilities.

For our second measure of validity of the Markov model we used state occupancy times as a mean of dwell time. Finding the vector associated with the exponential parameters of $\mathbf{P}$, we can compare CDF of dwell time for different classes of receiver locations. The corresponding dwell time vector is found to be

$$\upsilon = [39.19 \quad 27.98 \quad 16.75 \quad 68.31] \tag{4.21}$$

which yields the parameters of the exponential model of residing in each state for DDP,NUDP, SUDP, and NC states respectively.

We simulated the exponential distributions and compared them to the dwell times resulted from RT simulation and dwell times obtained from running the

Markov chain. Fig. 4.4 represents the CDF comparison of dwell times in SUDP class of receiver locations. It is worth mentioning that other Markov states demonstrate similar close fits as illustrated in Fig. 4.5.

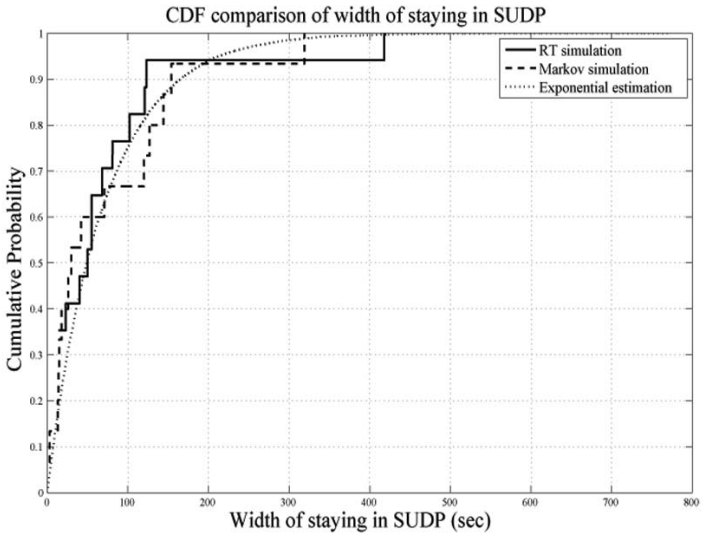

Figure 4.4: Dwell time distribution of mobile terminal in SUDP state

4.3.1.2 Ranging error statistics

As discussed in section 3.4 empirical models using measurement and RT have confirmed that ranging errors occurring in DDP and NUDP states can be modeled with normal distribution whose moments are functions of the bandwidth of the channel [Ala06b, Hei06]. However, in SUDP class of receiver location the distribution which fits the observed ranging error is GEV. Tables 3.1 and 3.3 summarize the statistics of ranging error for different states of the presented Markov model for a bandwidth of 5 GHz obtained from the analysis of CIRs of the same 14000 receiver locations in the third floor of the $AK Labs$.

Using the statistics of ranging error and the parameters of the Markov model of Fig. 4.1 provided by Eqn. 4.6 enable us simulate the dynamic behavior of

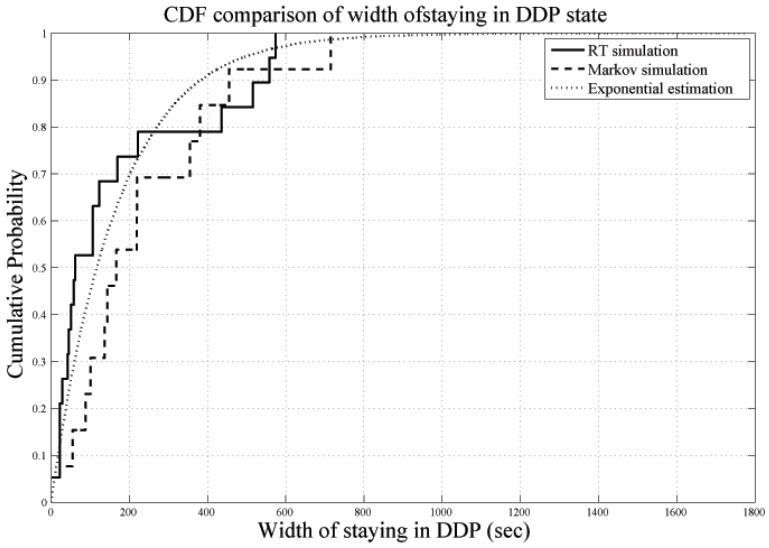

(a) Dwell time distribution of mobile terminal in DDP state

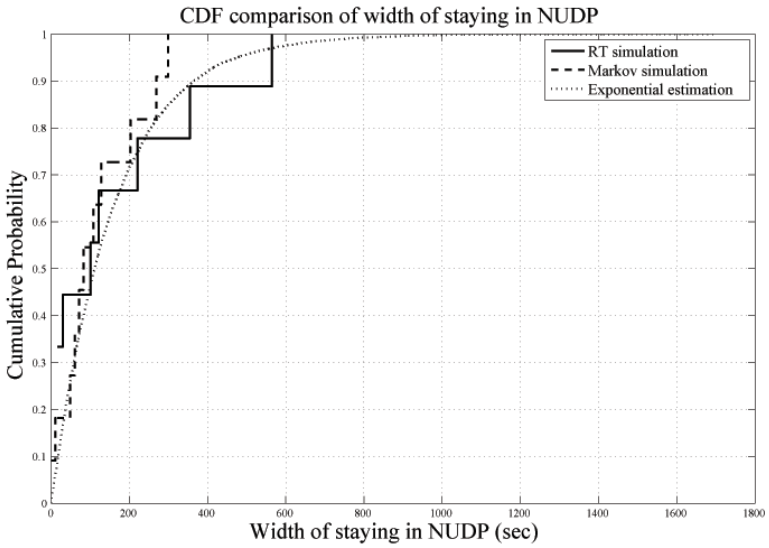

(b) Dwell time distribution of mobile terminal in NUDP state

Figure 4.5: Distributions of dwell time for a random mobile terminal in DDP and NUDP states

ranging error observed by the mobile user. In order to verify the results of the Markov model we compared the results of Markov model simulation with real-time RT simulation. To set up the Markov simulation we first initialized the Markov model with an estimate of state probabilities obtained from MND model and ran the Markov process with the transition probabilities reported in Eqn. 4.19. The output of the Markov model included a series of classes of ranging error. According to the class of ranging error produced by Markov model, we simulated the ranging error of each state by using parameters of Tables 3.1 and 3.3. The output of process included a series of ToA ranging errors whose class were defined according to Markov process and their value were determined according to the underlying distribution of ranging error for the specified class.

On the other hand, in RT simulation, we let the mobile terminal perform a *random walk* in indoor environment and recorded the ToA ranging error for a long period of time. We then compared the CDFs of Markov simulation and RT simulation.

Figure 4.6 compares the CDF of total ranging error observed by the mobile user traveling in indoor environment for empirical data using simulation and analytical dynamic Markov model. It is worth mentioning that comparisons of empirical and simulated ranging error observed in individual classes also show close agreement as the underlying distribution was carefully chosen based on individual classes' distributions of ranging error described in 4.1.

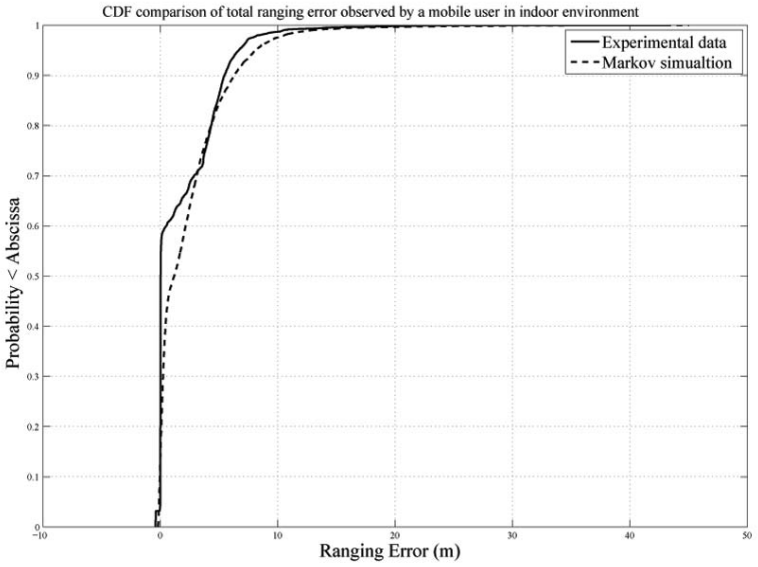

Figure 4.6: Comparison of ranging error observed by a mobile user with simulation

4.3.2 Modeling and analysis of state probabilities

For the building under study varying the location of the transmitter and recording the state probabilities using IDM realization yielded

$$\hat{\bar{\mu}} = [0.3662 \quad 0.4332 \quad 0.0747]$$
$$\hat{\mathbf{\Sigma}} = \begin{bmatrix} 0.0081 & -0.0015 & 0.004 \\ -0.0015 & 0.0096 & -0.0031 \\ 0.004 & -0.0031 & 0.0018 \end{bmatrix} \tag{4.22}$$

Following the Cholesky decomposition method and regenerating the state probabilities we can approximate the parameters of the MND model and compare the MND model with the result of simulation. Figure 4.7 illustrates the reconstruction of the state probabilities with 100 iterations for the main three states using MND

model. The NC state can be found deterministically using

$$P_{NC} = 1 - P_{DDP} - P_{NUDP} - P_{SUDP} \tag{4.23}$$

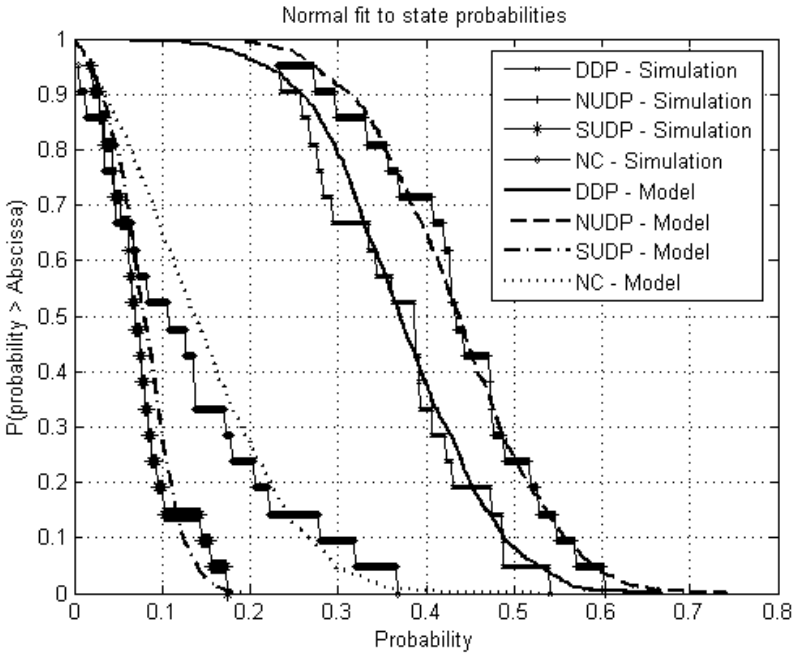

Figure 4.7: Comparison of the CDF of the state probabilities for different states with their respective normal fit

It can be observed that the MND model generated state probabilities closely follow IDM.

Chapter 5

Binary Hypothesis Testing for UDP Identification

Another open problem in the field of localization and positioning is the problem of identification of the channel profiles which exhibit unexpected large ranging errors. In traditional localization the distance measurements from different RPs were incorporated into the localization algorithm without mitigating the effects of ranging error. Therefore, the accuracy of the localization system would degrade drastically when problem of UDP occurred. The following chapter and the next chapter investigate different techniques in identification of these channel profiles with large ranging errors (UDP identification). We have used propagation parameters of the wireless channel profile at the receiver side to decide whether a channel profile is in UDP conditions. To illustrate the effectiveness of such identification of channel profiles with UDP conditions, we set up an experiment with very limited number of RPs and compared the performance of the traditional algorithm with the proposed algorithm based on UDP identification. In the proposed algorithm we suggest to adjust the value of the distance measurement once a channel profile is identified to be in UDP

conditions. The adjustment is performed by subtracting a correction value from the distance measurement. The amount of the correction value is determined based on predefined distributions of the ranging error in the typical environments similar to the building under study. Section 5.1 of this chapter defines the RF propagation metrics being used for identification purposes. Section 5.2 introduces the binary hypothesis method and analyzes the accuracy of such algorithm in identifying the UDP conditions. Finally, Section 5.3 evaluates the effectiveness of UDP identification in localization accuracy enhancement of indoor localization in a sample scenario using the results of RT and real-time measurement.

5.1 Indoor Localization

As discussed in the previous chapters, the most important and distinguishing parameter in ToA-based localization system is the presence of the DP component. Detecting the DP component results in accurate ranging estimate of the distance of the antenna pair. On the other hand, the erroneous estimation of the distance of the antenna pair results in large ranging error observed by the localization system and drastically degrades the performance of such systems. Therefore, we face two hypotheses

$$\begin{cases} H_0 : DDP \mid d_{FDP} \approx d_{DP}, \varepsilon \approx 0 \\ H_1 : UDP \mid d_{FDP} \gg d_{DP}, \varepsilon \gg 0 \end{cases} \tag{5.1}$$

where H_0 denotes the DDP hypothesis, which indicates that the channel profile can effectively be used for localization, and H_1 denotes the UDP hypothesis, which indicates that the channel profile is not appropriate for being used for localization purposes. d_{DP}, d_{FDP}, and ε are defined in Eqns. 1.3 through 1.5.

5.1.1 Least Square Solution to Indoor Localization Problem

In 2-D localization, knowledge of three accurate distance measurements from three known reference points (RPs) will be sufficient to accurately locate the mobile terminal with the help of trilateration. Assume $[x_r \quad y_r]$ is the estimate of the coordinates of the mobile terminal. Furthermore, assume $[x_i \quad y_i]$ is the coordinate of the i^{th} RP. The distance between the i^{th} RP and mobile terminal can then be estimated as

$$(x_r - x_i)^2 + (y_r - y_i)^2 = d_{FDP}^2 \tag{5.2}$$

where estimated distance is defined as $d_{FDP} = d_{DP} + \varepsilon_d$. This ranging error term includes three different ranging error contributors. As shown in [Hei07c], these three contributors can be modeled as

$$\varepsilon_d = \varepsilon_{UDP} + \varepsilon_m + \varepsilon_{pd} \tag{5.3}$$

where ε_{UDP}, ε_m, and ε_{pd} represent blockage of DP, multipath, and propagation delay induced errors, respectively. ε_{pd} is assumed to be insignificant for indoor environment while ε_m is shown to follow a normal distribution, $\mathcal{N}(0, \sigma_\omega^2)$ where its variance, σ_ω^2 decreases with the increase of bandwidth and is shown to be sufficiently small for the bandwidths greater than 200 MHz [Pah06]. The term ε_{UDP} does not exist if the mobile terminal is in DDP conditions; however, in UDP conditions it can be observed that the infrastructure of the indoor environment commonly obstructs the DP component and causes unexpected larger ranging errors. As a result, the statistical characteristics of the ranging error in UDP class exhibits a heavy tail in its distribution function. This heavy tail phenomenon has been reported and modeled in the literature; in [Ala03, Den04] the observed ranging error was modeled

as a combination of a Gaussian distribution and an exponential distribution and [Jo06, Als07b] model the ranging error with a log-normal distribution, and finally [Als07a, Hei07c] model the behavior of ranging error in harsh NLoS environment with GEV. In this section, for simplicity, we will model the term ε_{UDP} with a normal random variable with known statistics as reported in [Ala06a].

One approach to solve the localization problem is to use least-squares (LS) method to solve the set of trilateration equations 1.4 of the form

$$\begin{cases} (x_r - x_1)^2 + (y_r - y_1)^2 = d_{FDP_1}^2 \\ (x_r - x_2)^2 + (y_r - y_2)^2 = d_{FDP_2}^2 \\ (x_r - x_3)^2 + (y_r - y_3)^2 = d_{FDP_3}^2 \end{cases} \tag{5.4}$$

in which d_{FDP_i} represents the estimated distance of the transmitter and the receiver.

Increasing the number of RPs will enhance the accuracy of the system as it increases the likelihood of observing three or more precise ranging measurements from RPs. In such scenarios, one approach to mitigate the UDP problem is to simply discard the profiles suspicious to be UDP. In practice, however, those scenarios are rare and positioning systems often have access to only three or fewer RPs. In addition, harsh indoor wireless environment introduces erroneous estimates of distance which degrades the performance of the localization algorithm. In these cases, we have to remedy the ranging estimate of the ToA measurement system.

In traditional localization systems, one approach is to estimate the receiver position using the least-squares (LS) algorithm to solve the trilateration equations given in Eqn. 5.4. The particular instance of the LS algorithm that has been used for our evaluations is the one by Davidon [Dav68], which attempts to minimize the

objective function

$$Q(\mathbf{x}) = \sum_{j=1}^{N} \left(d_j - \sqrt{(x_r - x_j)^2 + (y_r - y_j)^2} \right)^2 \qquad \mathbf{x} = [x_r \quad y_r] \tag{5.5}$$

in an iterative manner using the following relation

$$\mathbf{x}_{k+1} = \mathbf{x}_k - \mathbf{H}_k \mathbf{g}(\mathbf{x}_k) \tag{5.6}$$

where $\mathbf{H}_k$ represents an approximation to the inverse of the Hessian of $Q(\mathbf{x})$, $\mathbf{G}(\mathbf{x})$, which is defined as

$$\mathbf{G}(\mathbf{x}) = \begin{pmatrix} \frac{\partial^2 f}{\partial x^2} & \frac{\partial^2 f}{\partial x \partial y} \\ \frac{\partial^2 f}{\partial y \partial x} & \frac{\partial^2 f}{\partial y^2} \end{pmatrix} \tag{5.7}$$

and $\mathbf{g}(\mathbf{x})$ is the gradient of $Q(\mathbf{x})$, defined as

$$\mathbf{g}(\mathbf{x}) = \nabla f(\mathbf{x}) \tag{5.8}$$

The following relation defines when the computations will be terminated

$$\rho_k = (\mathbf{g}(\mathbf{x}_{k+1}))^T \mathbf{H}_k (\mathbf{g}(\mathbf{x}_{k+1})) \tag{5.9}$$

so that the iterations will stop when $\rho_k \leq \epsilon$, where ϵ is a small tolerance value.

In this section, we propose a methodology to distinguish between the DDP and UDP conditions by investigating the statistics of the specific metric of the channel profile. For the purpose of simulation and algorithm development we used both RT simulation database, 2.1, and measurement database, 2.2, to extract the desired metrics, range estimate, τ_{FDP}, and subsequently we can estimate d_{DP}. We

then prove the effectiveness of identifying the UDP conditions by employing the UDP identification idea in a real-time scenario designed for localization in indoor environment.

There are two types of metrics being extracted from channel profile which can be utilized in identification of UDP conditions. The first class of metrics, is the time delay characteristics of the channel profile, while the second class deals with power characteristics of the channel profile. We can also utilize a hybrid metric, consists of time and power, in order to classify the receiver location.

5.1.2 Time Metrics

The time characteristics of channel profiles have been used in literature for variety of applications in communication field [Mol96, Has92, Rap90]. RMS delay spread and mean excess delay are being used to determine the data-rate of the communication systems in indoor and outdoor environment. Here, we utilize the time characteristic to identify UDP condition [Hei07b, Hei07a, Hei08a, Hei08b].

5.1.2.1 Mean Excess Delay

Delay information encrypted in the channel profile is our first time metric to investigate. Amongst all of the delay metrics the mean excess delay of the channel profile is the easiest to find and perhaps the most effective metric, relatively, to efficiently identify the UDP conditions. We used RT database for modeling the different distributions of mean excess delay in this section. Mean excess delay is defined as the

$$\tau_m = \frac{\sum_{i=1}^{L_p} \hat{\tau}_i |\alpha_i|^2}{\sum_{i=1}^{L_{dp}} |\alpha_i|^2} \tag{5.10}$$

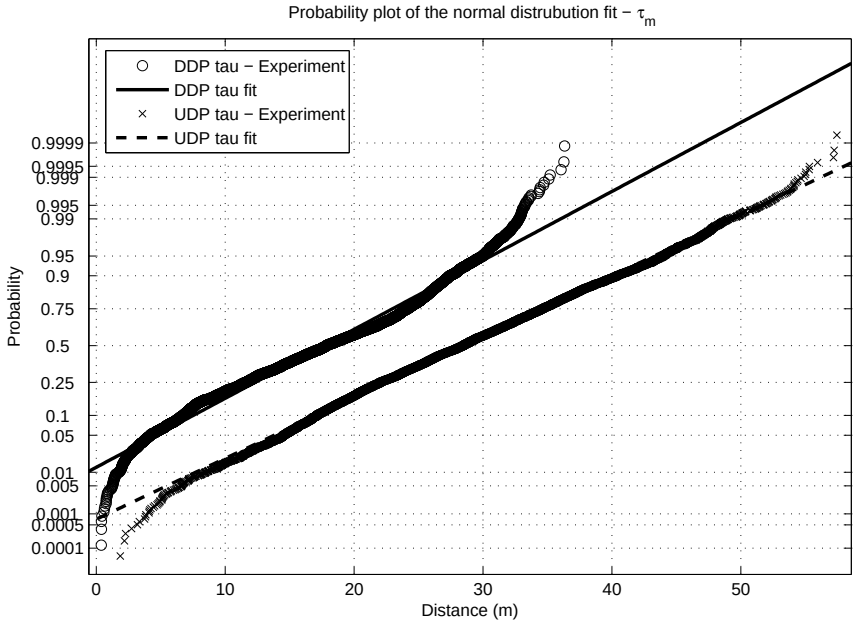

Figure 5.1: Normality of τ_m for DDP and UDP profiles - Probability plot preview

where $\hat{\tau}_i$ and α_i represent the ToA and complex amplitude of the i^{th} detected path, respectively, and L_p represents the number of detected peaks.

Conceptually, it can be observed that profiles with higher mean excess delay are more likely to be UDP conditions as it is illustrated in Fig. 5.1 in which the τ_m values are converted to distances.

By graphing the distribution of the τ_m for DDP and UDP the normality of the distributions can be verified. Figure 5.2 illustrates the distributions along with their normal fits.

The probability plots of the distribution of DDP and UDP clearly indicate that they can be best modeled with normal distribution and their separation indicates that their normal distribution parameters are distinct as follows

$$\begin{cases} f(\tau_m^d|H_0) = \frac{1}{\sqrt{2\pi}\sigma_m^d} \exp[-\frac{(\tau_m^d-\mu_m^d)^2}{2(\sigma_m^d)^2}] \\ f(\tau_m^u|H_1) = \frac{1}{\sqrt{2\pi}\sigma_m^u} \exp[-\frac{(\tau_m^u-\mu_m^u)^2}{2(\sigma_m^u)^2}] \end{cases} \tag{5.11}$$

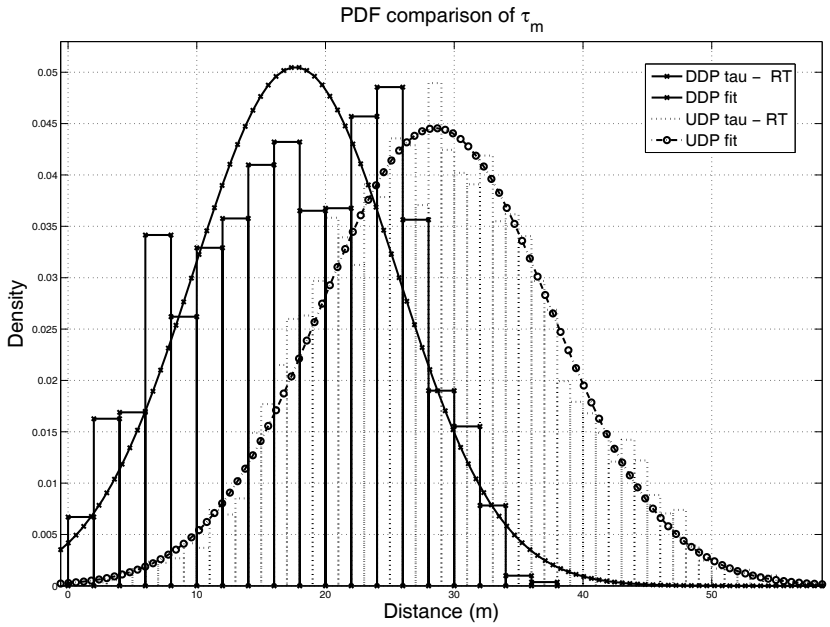

Figure 5.2: Normality of τ_m for DDP and UDP profiles - Distribution preview

where μ_m^d and σ_m^d represent the mean and standard deviation of the channel profiles associated with DDP conditions. Similarly, μ_m^u and σ_m^u represent the mean and standard deviation of the channel profiles associated with UDP conditions. These parameters are reported in Table 5.2 [Hei07b, Hei08a].

In order to quantitatively determine the goodness-of-fit of the data to the normal distribution we apply the Kolmogorov-Smirnov ($K-S$) and χ^2 hypothesis tests. The results of the normal distribution parameters, $K-S$ test and χ^2 test are summarized in Table 5.1.

Table 5.1: The mean and standard deviation of the normal distribution for the τ_m

Channel Profile	μ_{τ_m}	σ_{τ_m}	$K-S_\tau$	χ^2_τ
DDP	17.65	7.90	94.02%	55.61%
UDP	28.54	8.95	98.31%	59.72%

It can be observed that normal distribution passes the assumption of normality for both DDP and UDP classes.

5.1.2.2 RMS Delay Spread

Another useful time metric which can be used for UDP identification purposes is RMS delay spread [Hei07a, Hei08b]. We used measurement database to build and model the distributions of RMS delay spread for DDP and UDP conditions. RMS delay spread is defined as the

$$\tau_{rms}^2 = \frac{\sum_{i=1}^{L_p} (\hat{\tau}_i - \tau_m)^2 |\alpha_i|^2}{\sum_{i=1}^{L_p} |\alpha_i|^2} \tag{5.12}$$

where $\hat{\tau}_i$ and α_i represent the ToA and complex amplitude of the i^{th} detected peak, respectively, L_p represents the number of detected peaks, and τ_m is the mean excess delay of the channel profile defined in 5.10. Conceptually, it can be observed that profiles with higher RMS delay spread are more likely to be UDP conditions.

Constructing a database of DDP and UDP channel profiles and extracting their propagation metrics enable us to compare the statistics of the desired metric. Comparing the probability plots of the extracted RMS delay spread for DDP and UDP conditions further highlights the differences between the two cases as it is illustrated in Fig. 5.3 in which the τ_{rms} values are converted to distances [Hei07a, Hei08b].

The probability plots of the distribution of DDP and UDP clearly indicates that they can be best modeled with normal distribution and their separation indicates that their normal distribution parameters are distinct which follows

$$\begin{cases} f(\tau_{rms}^d | H_0) = \frac{1}{\sqrt{2\pi}\sigma_{rms}^d} \exp[-\frac{(\tau_{rms}^d - \mu_{rms}^d)^2}{2(\sigma_{rms}^d)^2}] \\ f(\tau_{rms}^u | H_1) = \frac{1}{\sqrt{2\pi}\sigma_{rms}^u} \exp[-\frac{(\tau_{rms}^u - \mu_{rms}^u)^2}{2(\sigma_{rms}^u)^2}] \end{cases} \tag{5.13}$$

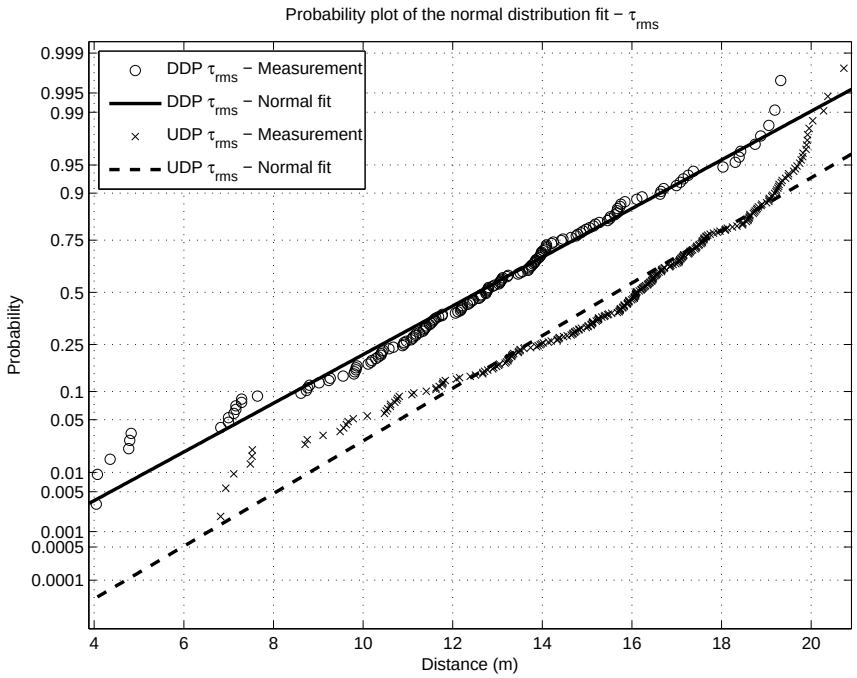

Figure 5.3: Normality of τ_{rms} for DDP and UDP profiles - Probability plot preview

where μ^d_{rms} and σ^d_{rms} represent the mean and standard deviation of the channel profiles associated with DDP conditions. Similarly, μ^u_{rms} and σ^u_{rms} represent the mean and standard deviation of the channel profiles associated with UDP conditions. These parameters are reported in Table 5.2.

In order to quantitatively determine the goodness-of-fit of the data to the normal distribution we apply the Kolmogorov-Smirnov $(K-S)$ and χ^2 hypothesis tests. Both of the hypothesis tests are performed at 5% significant level to obtain the passing rates of the proposed distribution. The results of the normal distribution parameters, $K-S$ test and χ^2 test are summarized in Table 5.2. It can be observed that normal distribution passes the assumption of normality. It is worth mentioning that the other measures of time delay characteristics of channel profile are not found to be as effective for our classification [Hei07b, Hei08a].

Table 5.2: The mean and standard deviation of the normal distribution for the τ_{rms}

Channel Profile	$\mu_{\tau_{rms}}$	$\sigma_{\tau_{rms}}$	$K-S_{\tau_{rms}}$	$\chi^2_{\tau_{rms}}$
DDP	12.55	3.18	94.30%	56.63%
UDP	15.64	2.94	89.02%	47.21%

5.1.3 Power Metrics

The other class of metrics that can be extracted from the channel profile are power characteristics. There is hidden information regarding the DDP/UDP classification in the respective power characteristics. Amongst the useful power metrics, total power and FDP power are the most useful ones.

Total Power

- Modeling the Distribution of Total Power using RT Database

RSS is a simple metric that can be measured easily and it is measured and reported by most wireless devices. For example, the MAC layer of IEEE 802.11 WLAN standard provides RSS information from all active access points (APs) in a quasi-periodic beacon signal that can be used as a metric for localization [Kan06]

$$-P_{tot} = r = -10\log_{10}(\sum_{i=1}^{L_p}|\alpha_i|^2) \tag{5.14}$$

For identification, we used $-P_{tot} = r$ which is referred to as power Loss [Hei07b, Hei07a, Hei08a, Hei08b]. It can be observed that profiles with higher power Loss are more likely to be UDP conditions. This is best illustrated in Fig. 5.4 in which their respective probability plots with their Weibull fits are sketched. The separation of the curves illustrates the difference of the $P_{tot} = r$ behavior for different DDP/UDP conditions.

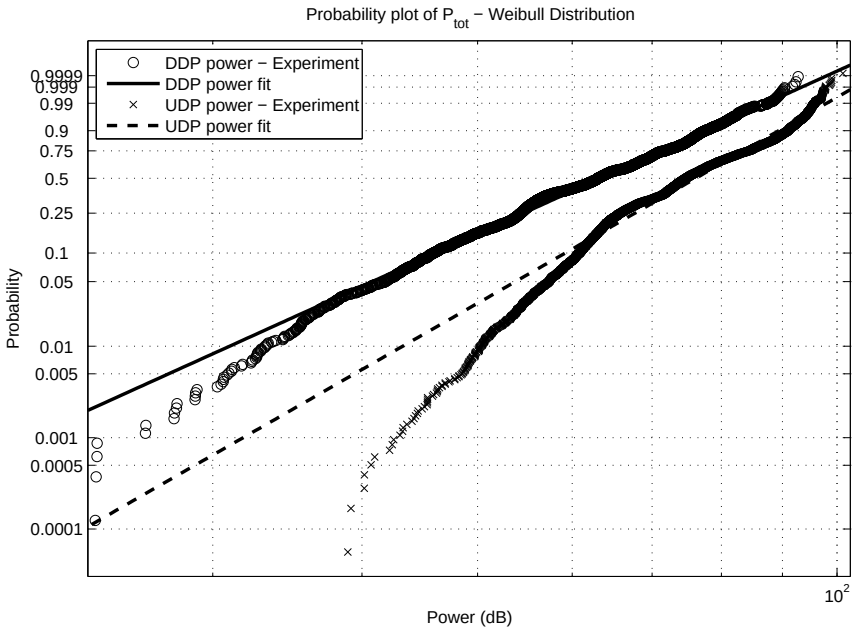

Figure 5.4: Weibull distribution modeling of total power for RT database - Probability plot preview

By graphing the distribution of the $-P_{tot} = r$ for DDP and UDP it can be verified that the distributions of total power are following a Weibull distribution. Figure 5.5 illustrates the distributions along with their normal fits.

$$\begin{cases} f(r^d_{RT}|H_0) = \frac{b^d_{RT}}{a^d_{RT}}(\frac{r^d_{RT}}{a^d_{RT}})^{b^d_{RT}-1}\exp[-(\frac{r^d_{RT}}{a^d_{RT}})^{b^d_{RT}}] \\ f(r^u_{RT}|H_1) = \frac{b^u_{RT}}{a^u_{RT}}(\frac{r^u_{RT}}{a^u_{RT}})^{b^u_{RT}-1}\exp[-(\frac{r^u_{RT}}{a^u_{RT}})^{b^u_{RT}}] \end{cases} \tag{5.15}$$

where b^d_{RT} and a^d_{RT} represent the shape and scale parameters of the Weibull distribution associated with DDP channel profiles, respectively. Similarly, b^u_{RT} and a^u_{RT} represent the shape and scale parameters of the Weibull distribution associated with UDP channel profiles. The parameters are reported in Table 5.3.

Again, in order to quantitatively determine the goodness-of-fit of the Weibull distribution to the data we apply the Kolmogorov-Smirnov $K-S$ and χ^2 hypothesis

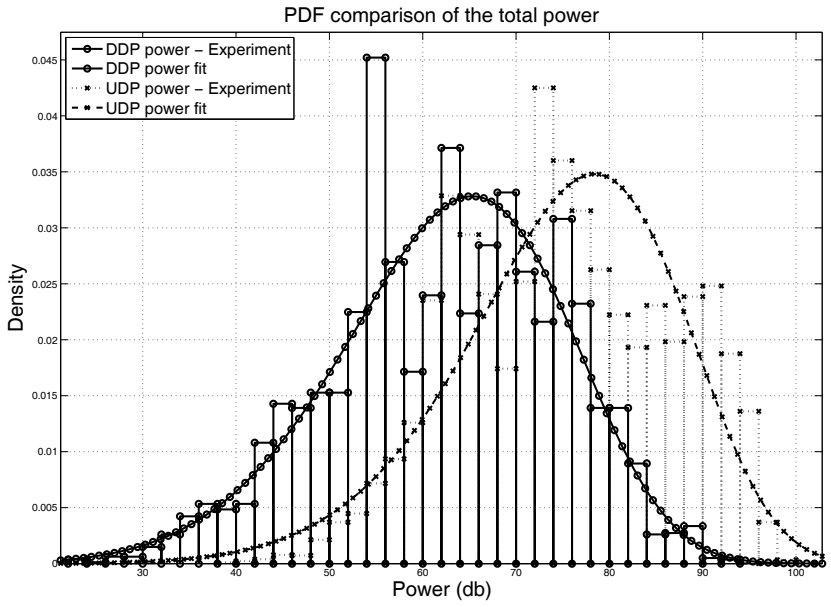

Figure 5.5: Weibull distribution modeling of power loss for RT database - Distribution preview

tests. The results of the Weibull distribution parameters, $K-S$ test and χ^2 test are summarized in Table 5.3.

Table 5.3: The a and b parameters of the Weibull distribution for the $-P_{tot} = r$

Channel Profile	a_{RT}	b_{RT}	$K-S_{RT}$	χ^2_{RT}
DDP	67.38	5.92	95.11%	55.97%
UDP	79.94	7.49	94.78%	46.51%

It can be observed that Weibull distribution passes the $K-S$ and χ^2 hypothesis tests.

- Modeling the Distribution of Total Power using Measurement Database

At the same time we used the measurement database to model the distribution of the power loss [Hei07a, Hei08b]. Again, it can be observed that we distinguish between DDP and UDP conditions based on the observed value of total power. This

is best illustrated in Fig. 5.6 in which their respective probability plots and their Weibull fits are sketched. According to our studies and based on the comparison of the goodness-of-fit for different distributions for modeling the total power, we chose Weibull distribution.

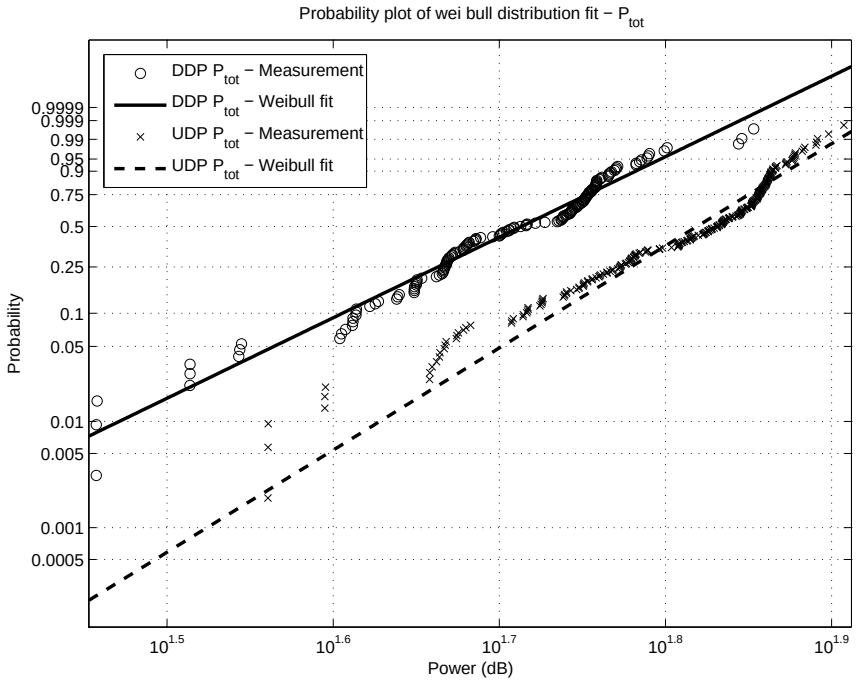

Figure 5.6: Weibull distribution modeling of total power

The selection of the best distribution is performed by Akaike's weights method. The separation of the curves illustrates the difference of the $-P_{tot} = p$ behavior for different DDP/UDP conditions. The distributions can then be described as following

$$\begin{cases} f(r^d_{meas}|H_0) = \frac{b^d_{meas}}{a^d_{meas}}(\frac{r^d_{meas}}{a^d_{meas}})^{b^d_{meas}-1}\exp[-(\frac{r^d_{meas}}{a^d_{meas}})^{b^d_{meas}}] \\ f(r^u_{meas}|H_1) = \frac{b^u_{meas}}{a^u_{meas}}(\frac{r^u_{meas}}{a^u_{meas}})^{b^u_{meas}-1}\exp[-(\frac{r^u_{meas}}{a^u_{meas}})^{b^u_{meas}}] \end{cases} \tag{5.16}$$

where b^d_{meas} and a^d_{meas} represent the shape and scale parameters of the Weibull distribution associated with DDP channel profiles, respectively. Similarly, b^u_{meas}

and a^u_{meas} represent the shape and scale parameters of the Weibull distribution associated with UDP channel profiles. The parameters are reported in Table 5.4 [Hei07a, Hei08b].

Table 5.4: The a and b parameters of the Weibull distribution for the $-P_{tot} = r$

Channel Profile	a_{meas}	b_{meas}	$K - S_{meas}$	χ^2_{meas}
DDP	54.23	7.59	89.57%	29.72%
UDP	70.45	9.63	88.55%	30.63%

Similarly, in order to quantitatively determine the goodness-of-fit of the Weibull distribution to the data we apply the Kolmogorov-Smirnov $K-S$ and χ^2 hypothesis tests. The results of the Weibull distribution parameters, $K-S$ test and χ^2 test are summarized in Table 5.4. It can be observed that Weibull distribution passes the $K-S$ hypothesis test but fails the χ^2 hypothesis test. As it can be concluded from Fig. 5.6 Weibull distribution fits the middle part of the probability plot of the both curves which is the reason behind failing the χ^2 hypothesis test.

5.1.4 Hybrid Time/Power metric

- Modeling the Distribution of the Hybrid Metric using RT Database

Although, individual time or power metric can be used to identify the class of receiver locations, but one can form a hybrid metric to achieve better results in identification of the UDP conditions. Here, we propose to use a hybrid metric consisting of ToA of DP component and its respective power as the metric to identify the UDP conditions [Hei07b, Hei08a]. Mathematically

$$\xi_{hyb} = -P_{FDP} \times \tau_{FDP} \tag{5.17}$$

where ξ_{hyb} represents the metric being extracted. It can be shown that the desired metric can be best modeled with Weibull distribution. Figure 5.7 represents the separation of the fits and proves that the proposed metric can efficiently be used in UDP condition identification.

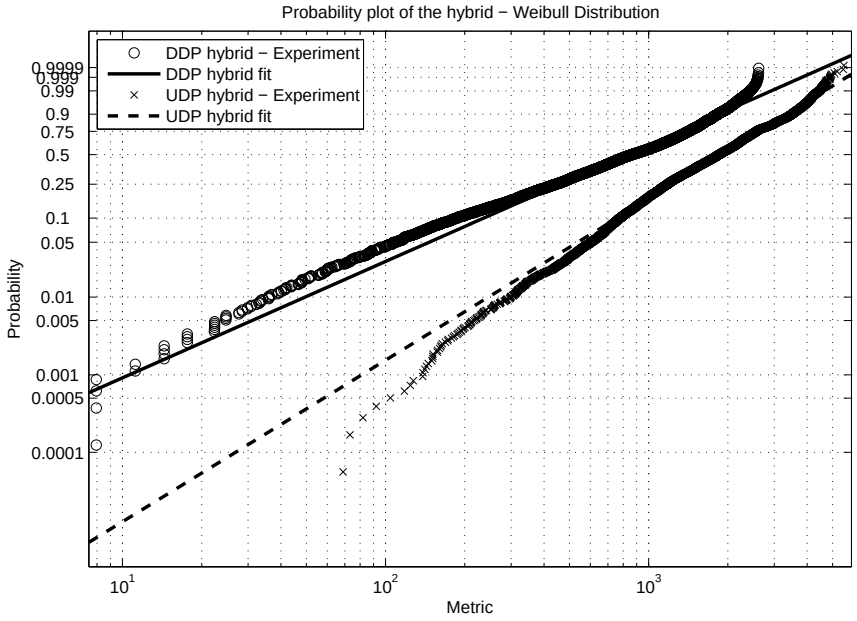

Figure 5.7: Weibull distribution modeling of hybrid metric

By graphing the distribution of the ξ_{hyb} for DDP and UDP the Weibullity of the distributions can be verified. Figure 5.8 illustrates the distributions along with their Weibull fits.

$$\begin{cases} f(\xi^d_{RT}|H_0) = \frac{\kappa^d_{RT}}{\vartheta^d_{RT}}(\frac{\xi^d_{RT}}{\vartheta^d_{RT}})^{\kappa^d_{RT}-1}\exp[-(\frac{\xi^d_{RT}}{\vartheta^d_{RT}})^{\kappa^d_{RT}}] \\ f(\xi^u_{RT}|H_1) = \frac{\kappa^u_{RT}}{\vartheta^u_{RT}}(\frac{\xi^u_{RT}}{\vartheta^u_{RT}})^{\kappa^u_{RT}-1}\exp[-(\frac{\xi^u_{RT}}{\vartheta^u_{RT}})^{\kappa^u_{RT}}] \end{cases} \tag{5.18}$$

where κ^d_{RT} and ϑ^d_{RT} represent the shape and scale parameters of the Weibull distribution associated with DDP channel profiles, respectively. Similarly, κ^u_{RT} and ϑ^u_{RT} represent the shape and scale parameters of the Weibull distribution associated with UDP channel profiles. Change of the name of the shape and scale parameters

from the Weibull distribution for total power to Weibull distribution for the hybrid metric was done merely to avoid confusion.

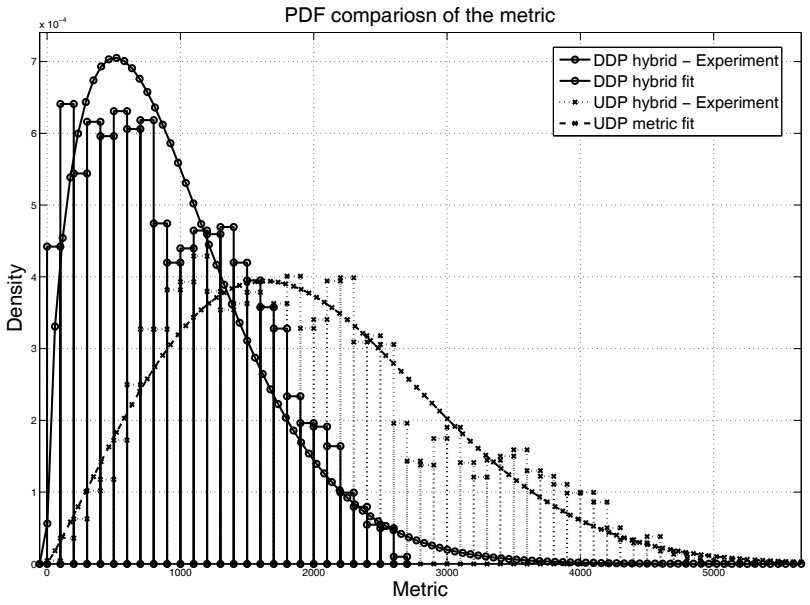

Figure 5.8: Weibullity of ξ_{hyb} for DDP and UDP profiles - Distribution preview

The results of $K-S$ and χ^2 tests for goodness-of-fit show close agreement for the assumption of the Weibull distribution. The results of the Weibull distribution parameters, $K-S$ test and χ^2 test are summarized in Table 5.5 [Hei07b, Hei08a].

Table 5.5: The ϑ and κ parameters of the Weibull distribution for the ξ_{hyb}

Channel Profile	ϑ_{RT}	κ_{RT}	$K-S_{RT}$	χ^2_{RT}
DDP	1056.89	1.50	94.58%	56.69%
UDP	2236.32	2.08	97.46%	55.19%

- Modeling the Distribution of the Hybrid Metric using Measurement Database

Similar to total power discussion we can use the measurement campaign to model the distribution of the hybrid metric as well. By studying the hybrid metric gathered

from DDP and UDP channel profiles it can be shown that the desired metric can be best modeled with Weibull distribution [Hei07a, Hei08b]. Figure 5.9 represents the separation of the fits and proves that, indeed, the proposed metric can effectively be used in UDP condition identification.

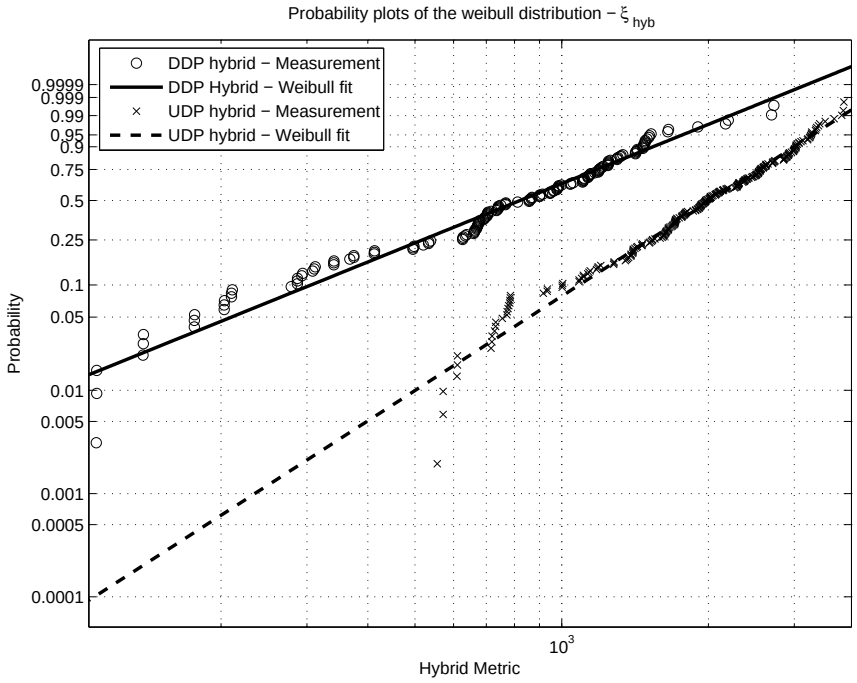

Figure 5.9: Weibull distribution modeling of hybrid metric

The corresponding equations can then be described as

$$\begin{cases} f(\xi^d_{meas}|H_0) = \frac{\kappa^d_{meas}}{\vartheta^d_{meas}}\left(\frac{\xi^d_{meas}}{\vartheta^d_{meas}}\right)^{\kappa^d_{meas}-1}\exp[-\left(\frac{\xi^d_{meas}}{\vartheta^d_{meas}}\right)^{\kappa^d_{meas}}] \\ f(\xi^u_{meas}|H_1) = \frac{\kappa^u_{meas}}{\vartheta^u_{meas}}\left(\frac{\xi^u_{meas}}{\vartheta^u_{meas}}\right)^{\kappa^u_{meas}-1}\exp[-\left(\frac{\xi^u_{meas}}{\vartheta^u_{meas}}\right)^{\kappa^u_{meas}}] \end{cases} \tag{5.19}$$

where κ^d_{meas} and ϑ_{meas} represent the shape and scale parameters of the Weibull distribution associated with DDP channel profiles, respectively. Similarly, κ^u_{meas} and ϑ_{meas} represent the shape and scale parameters of the Weibull distribution associated with UDP channel profiles.

The results of $K-S$ and χ^2 tests for goodness-of-fit show close agreement for the assumption of the Weibull distribution. The results of the Weibull distribution parameters, $K-S$ test and χ^2 test are summarized in Table 5.6 [Hei07a, Hei08b].

Table 5.6: The ϑ and κ parameters of the Weibull distribution for the ξ_{hyb}

Channel Profile	ϑ_{meas}	κ_{meas}	$K-S_{meas}$	χ^2_{meas}
DDP	995.05	1.90	91.00%	52.00%
UDP	2279.09	3.03	94.92%	87.25%

5.2 Binary Hypothesis Testing for UDP Identification

Knowledge of the statistics of τ_m, τ_{rms}, r, and ξ_{hyb} enables us to identify the UDP conditions. In order to do so binary likelihood ratio tests can be performed to select the most probable hypothesis. For this purpose, we picked a random profile and extracted its respective metrics. The likelihood function of observed mean excess delay, τ_{m_i}, for DDP condition can then be described as

$$L(H_0|\tau_{m_i}) = P_r(\tau_{m_i}|H_0) \tag{5.20}$$

Similarly, the likelihood function of observed RMS delay spread, τ_{m_i}, for UDP condition can then be described as

$$L(H_1|\tau_{m_i}) = P_r(\tau_{m_i}|H_1) \tag{5.21}$$

The likelihood ratio function of τ_m can then be determined as

$$\Lambda(\tau_{m_i}) = \frac{\sup\{L(H_0|\tau_{m_i})\}}{\sup\{L(H_1|\tau_{m_i})\}} \tag{5.22}$$

The defined likelihood ratio functions are the simplified Bayesian alternative to the traditional hypothesis testing [Hei07b, Hei08a]. The outcome of the likelihood ratio functions can be compared to a certain threshold, i.e. unity for binary hypothesis testing, to make a decision

$$\Lambda(\tau_{m_i}) \underset{H_1}{\overset{H_0}{\gtrless}} \eta_m \tag{5.23}$$

Similarly, we can define the likelihood functions for τ_m, P_{tot} and ξ_{hyb} as

$$\Lambda(\tau_{m_i}) = \frac{\sup\{L(H_0|\tau_{m_i})\}}{\sup\{L(H_1|\tau_{m_i})\}} \tag{5.24}$$

$$\Lambda(p_i) = \frac{\sup\{L(H_0|p_i)\}}{\sup\{L(H_1|p_i)\}} \tag{5.25}$$

$$\Lambda(\xi_i) = \frac{\sup\{L(H_0|\xi_i)\}}{\sup\{L(H_1|\xi_i)\}} \tag{5.26}$$

which leads us to the corresponding hypothesis tests as

$$\Lambda(\tau_{m_i}) \underset{H_1}{\overset{H_0}{\gtrless}} \eta_{\tau_m} \tag{5.27}$$

$$\Lambda(p_i) \underset{H_1}{\overset{H_0}{\gtrless}} \eta_p \tag{5.28}$$

$$\Lambda(\xi_i) \underset{H_1}{\overset{H_0}{\gtrless}} \eta_\xi \tag{5.29}$$

Each of the above likelihood ratio tests can individually be applied for UDP identification of an observed channel profile. The outcome of the likelihood ratio test being greater than unity indicates that the receiver location is more likely to be a DDP condition and can appropriately be used in localization algorithm while the outcome less than unity indicates that the profile is, indeed, more likely to belong to

UDP class of receive location; hence, the estimated τ_{FDP} has to be remedied before being used in the localization algorithm.

To use the likelihood functions more effectively, we can combine the functions and form a joint likelihood function. Using the distributions obtained from RT database for UDP identification we can exploit τ_m, p, and ξ_{hyb} distributions and their respective parameters obtained from RT channel profiles to form the joint density function [Hei07b, Hei08a]. Assumption of the independence of the likelihood functions along with combining them leads to a suboptimal likelihood function defined as

$$\Lambda_{RT}(\tau_m, p, \xi_{hyb}) = \Lambda(\tau_m) \times \Lambda(p) \times \Lambda(\xi_{hyb}) \tag{5.30}$$

which can be compared to a certain threshold for decision making, i.e. $\Lambda(\tau_m, P_{tot}, \xi_{hyb}) \underset{H_1}{\overset{H_0}{\gtrless}} \eta_\delta$. For the simulation of the accuracy of the UDP identification we set up an experiment that consisted all the RT channel profiles existing in our database. We used 25% of channel profiles to obtain the parameters of the distributions, which are reported in Tables 5.1, 5.3, and 5.5. We used all the RT channel profiles, including the ones used for obtaining the parameters, for UDP identification and recorded the percentage of accuracy of each method. The results of the accuracy of the likelihood hypothesis tests, individually and as a joint distribution, are summarized in Table 5.7.

Table 5.7: Accuracy of the Likelihood Hypothesis Test using RT channel profiles

Likelihood Ratio	*CorrectDecision*
τ_m	70.85%
P_{tot}	67.06%
ξ_{hyb}	69.73%
$\Lambda_{RT}(\tau, r, \xi)$	89.29%

It can be observed that the accuracy of using individual metrics for identification

of UDP conditions is about 70% while combining the metrics for UDP identification can achieve 90% of accuracy.

Similarly, using τ_{rms}, r, and ξ_{hyb} distribution parameters obtained from measurement campaign we can form the joint density function as

$$\Lambda_{meas}(\tau_{rms}, p, \xi_{hyb}) = \Lambda(\tau_{rms}) \times \Lambda(p) \times \Lambda(\xi_{hyb}) \tag{5.31}$$

For the simulation of the accuracy of the UDP identification we set up an experiment that consisted all the measurement channel profiles existing in our database. We used 25% of channel profiles to obtain the parameters of the distributions, which are reported in Tables 5.2, 5.4, and 5.6. We used all the measurement channel profiles, including the ones used for obtaining the parameters, for UDP identification and recorded the percentage of accuracy of each method. The results of the accuracy of the likelihood hypothesis tests, individually and as a joint distribution, are summarized in Table 5.8.

Table 5.8: Accuracy of the Likelihood Hypothesis Test using Measurement Channel Profiles

Likelihood Ratio	$CorrectDecision$
τ_{rms}	72.40%
P_{tot}	78.30%
ξ_{hyb}	85.48%
$\Lambda_{meas}(\tau_{rms}, r, \xi)$	89.42%

It can be observed that the separations of the curves are larger in measurement database and the localization system have an easier job in terms of UDP identification.

5.3 Simulations and Results of Localization using ToA measurements

5.3.1 Simulations

For simulations, an internally developed ray tracing software has been used [Hol92] and the output of this software has been processed by Matlab® by using Davidon's least squares algorithm. The floor plan chosen for the simulations is the third floor of $AKLabs$ at WPI. The emphasize on the importance of the UDP identification on the accuracy of the localization system the following experiment was designed to assess the outcome of the localization system. The transmitters have been placed as shown in figure 5.10 indicated by triangles. The metallic chamber and the elevator shaft, shown as black shaded boxes, block the DP for a certain portion of the receiver's pathway (indicated by blue dots) and hence lead to large localization errors (indicated by black dotted estimates). The RMSE value of localization in this case is found to be $3.12\,m$.

Next we examine the UDP identification and range estimate mitigation associated with it. Identifying the UDP scenarios with the above method gives us an edge to mitigate the ranging estimate associated with the profile. Since the exact value of the error is not known, the best is to use the statistics of the error [Ala06b] and subtract that value from the observed estimated ranging.

$$\begin{aligned} \tau_{DP} &\simeq \tau_{FDP} - \varepsilon_{\tau} \\ d_{DP_i} &\simeq d_{FDP_i} - \varepsilon_{d} \end{aligned} \tag{5.32}$$

Mitigating the distance measurement of the antenna pair and employing the idea on the previous scenario results in enhanced localization error observed by

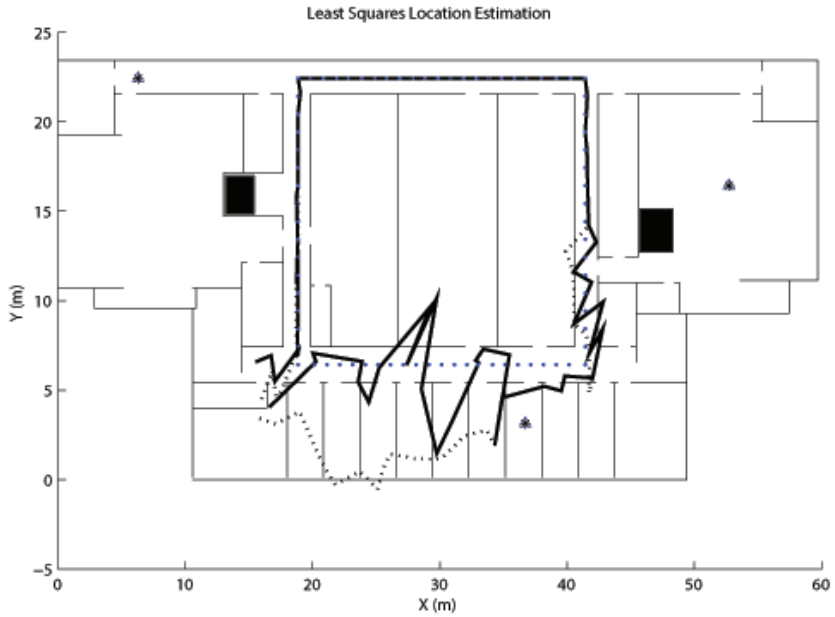

Figure 5.10: Localization error in sample indoor environment - Simulation

each receiver location and greatly improves the accuracy of the localization system. Figure 5.10 illustrates the estimation results in black solid line. It can be observed that identifying the UDP condition and mitigating the ranging error associated with such receiver locations, greatly improves the localization error observed in UDP receiver locations.

The RMSE value of the localization error has also improved by 50% and has dropped to 1.56 m. Obviously, the identification method is not absolute for all the receiver locations and it may identify some DDP profiles as UDP and by mistake subtract a correction value from their estimated ToA which will result in accuracy degradation at some receiver locations. However, as Fig. 5.10 illustrates, the identification and mitigation together can enhance the accuracy of the localization algorithm. Figure 5.11 compares the CDF of localization error associated with each scenario. It can be observed that even though localization error has increased at certain receiver locations, it has helped the algorithm to identify the UDP conditions

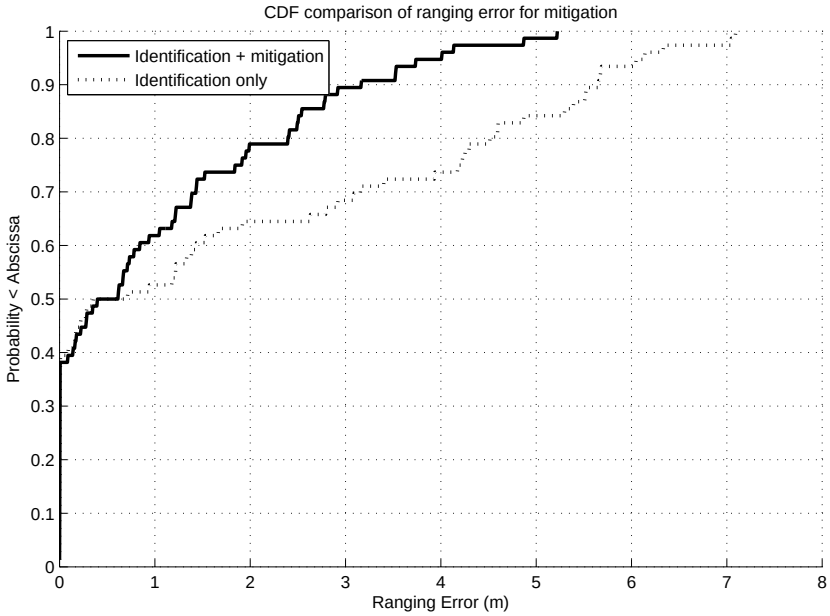

Figure 5.11: CDF of localization error for sample indoor environment - Simulation

and mitigate their ranging measurement to a more accurate location estimation on average.

5.3.2 Measurements

For the purpose of validating our approach in real world scenarios, we conducted wideband frequency domain measurements on the grid of receiver locations on the third floor of the $AKLabs$ at WPI. The measurement system and post processing procedure were described in section 2.2. Although the results of RT has already showed great enhancement in the accuracy of the localization system, but we can verify the results by employing the idea in a real-time scenario with real-time frequency-domain measurements.

Again, to emphasize on the importance and significance of identification of UDP condition, Fig. 5.12 describes localization with only three known RPs in the presence

of multipath and blockage (black dotted line). The RMSE value of localization error is found to be 8.42 m. The main reason for increased RMSE as compared to ray tracing is that in the real world scenario there are several micro metallic objects such as shelves, doors, and cabinets which block the DP component from the transmitter to receiver; therefore, the channel profile exhibits an erroneous range estimate. In ray tracing only major walls and large metallic obstructions are considered.

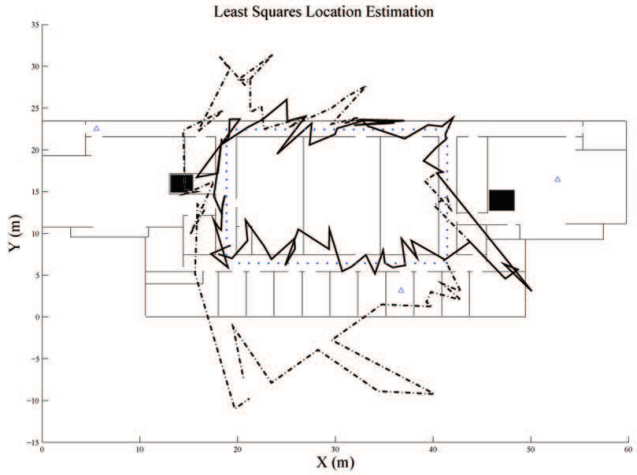

Figure 5.12: Localization error in sample indoor environment - Measurements

When we applied UDP identification and error mitigation as described earlier, we observed that the RMSE value of the localization error has also improved by 60% and has dropped to 3.95m.

Figure 5.13 compares the CDF of localization error associated with each scenario. Similar to the simulation case, it can be observed that, although localization error has increased at certain receiver locations, on average it has helped the algorithm to identify the UDP conditions and mitigate their ranging measurement for a more accurate location estimation.

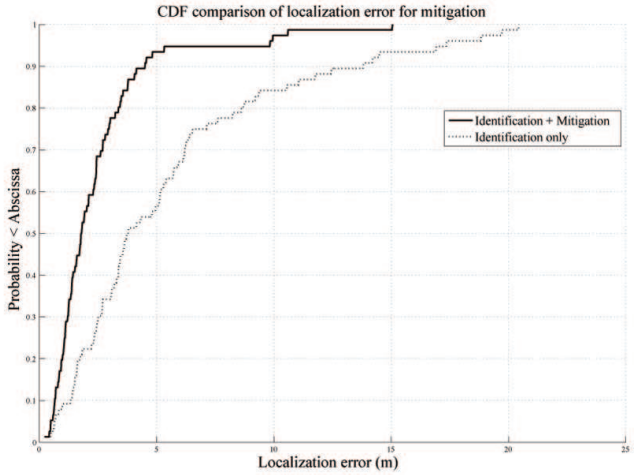

Figure 5.13: CDF of localization error for sample indoor environment - Measurements

Chapter 6

Neural Network Architecture for UDP Identification

The previous chapter addressed the issue of UDP identification based on binary hypothesis testing of propagation parameters of the wireless channel and the observed channel profile. It was concluded that binary hypothesis tests can be applied to the problem of the UDP identification to compare the likelihood of each hypothesis. The results showed considerable accuracy in identification of the UDP conditions and extensive improvement in the accuracy of the localization system over the traditional localization systems. In this chapter we adopt the same hypotheses and use the pattern classification characteristics of the neural network architecture to solve the problem of the UDP identification. We have used the same propagation parameter of the wireless channel to train the neural network and then have simulated the *unseen* channel profiles with the trained neural network to make a decision on UDP identification. Section 6.1 of this chapter describes the basics of the neural network architecture and Section 6.2 discusses the results of applying neural network to the problem of UDP identification.

6.1 Neural Network Architecture

In this section, we propose a second methodology to distinguish between the DDP and UDP conditions by investigating the propagation parameters of the channel profile and an application of neural network architecture (NNA) [Hei07a, Hei08b]. For the purpose of simulation we conducted wideband frequency-domain measurements on the grid of receiver locations on the third floor of the $AKLabs$ at WPI. The measurement system and post processing procedure were described in 2.2.

Amongst the important parameters of a radio signal, time delay propagation parameters and power propagation parameters have been widely used in the field of telecommunication. Here, we examine these radio propagation characteristics in order to identify the receiver locations with large ranging error. A hybrid metric consisted of both time delay and power characteristics can also be used for UDP identification [Hei07a, Hei08b]. The metrics and their respective distributions and distribution parameters are described in 5.1.

Although, individual measurement likelihood ratio tests can be applied for UDP identification of an observed channel profile. The outcome of the likelihood ratio test being greater than the threshold indicates that the receiver location is more likely to be a DDP condition and can appropriately be used in localization algorithm while the outcome less than unity indicates that the profile is, indeed, more likely to belong to UDP class of receive location; hence, the estimated τ_{FDP} has to be remedied before being used in the localization algorithm.

For more effectively using the likelihood functions, we can combine the outcomes of the likelihood functions and form a linear simple NNA as illustrated in Fig. 6.1, where three outputs of the likelihood functions are the inputs of the NNA, the hidden layer of the NNA consist of several neurons and the output of the NNA, δ,

represents the UDP identification flag [Hei07a, Hei08b].

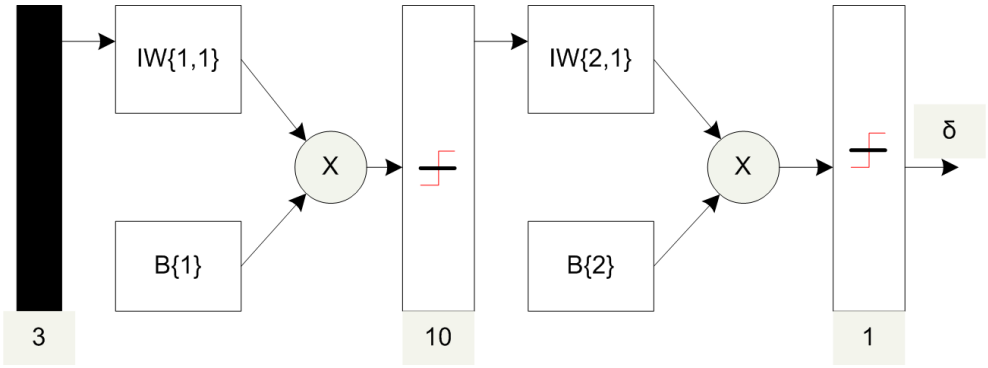

Figure 6.1: Basic schematic of the artificial neural network used in this study. For training, the network is fed with the extracted RMS delay spread, total power, and hybrid metric of the channel profile as inputs as well as UDP identification flag as output. The process os repeated for few receiver location. Once NNA is trained, the extracted metric of an unknown channel profile is fed to the network and networks simulates the respective output. The process is repeated for all of the transmitters, individually but simultaneously

There exist several network types available in literature to construct the NNA. Several examples of these types are feed-forward backdrop, cascade-forward backdrop, generalized regression, hopefield, and etc. The feed-forward backdrop type is chosen for this research [Dem07].

In general, NNA forms a function of the inputs to obtain the output; in case of our UDP identification flag

$$\delta = G_1(\sum_i \omega_i g_i(\mathbf{x})) \tag{6.1}$$

where G_1 is the predefined function and $\mathbf{x} = [\tau_{rms_i} \quad r_i \quad \xi_i]^T$ represents the input vector and ω_is represent the weights of the NNA. Each of the g_i components are themselves a function of the inputs of the NNA as follows

$$g_i(\mathbf{x}) = G_2(b_1\tau_{rms_i} + b_2 r_i + b_3\xi_i) \tag{6.2}$$

where G_2 is the inner predefined function and b_is are referred to as biases of the

NNA.

The task of the NNA is to learn the pattern of the occurrence of UDP based on the training set of data which is available to the NNA at the training mode. In order to learn and adjust the weights and biases to solve the task in an optimal sense, we have to initially define a cost function for the network. The typical cost functions used in NNA are mean squared error (MSE), regularized mean squared error (MSEREG), and sum squared error (SSE) defined as

$$\begin{aligned} mse &= \frac{1}{Q}\sum_{k=1}^{Q}(i(k)-o(k))^2 \\ msereg &= \gamma mse + (1-\gamma)msw \\ sse &= \sum_{k=1}^{Q}(i(k)-o(k))^2 \end{aligned} \tag{6.3}$$

where $i(k)$s are the targets of the NNA and $o(k)$s are the outputs of the NNA. Q represents the number of training sequence. γ is defined as the performance ratio and $msw = \frac{1}{n}\sum_{j=1}^{n} w_j^2$ is mean of the sum of squares of the network weights and biases [Dem07]. The goal of NNA is to minimize the preferred cost function over the training input data. For better functionality of NNA and prevent the weights and biases to grow exponentially, the input data are usually normalized to the range of [0 1].

Training function of the NNA is another important aspect of NNA which affects the performance of the NNA. There exist various functions for training a feed-forward backdrop NNA such as Levenberg-Marquardt algorithm, conjugate gradient algorithms, and quasi-Newton algorithms. The difference between the algorithms are their speed, memory usage, and performance. Levenberg-Marquardt algorithm is shown to be one of the fastest algorithms while maintaining the performance at

desired level [Dem07].

After selecting the type of the NNA and training functions, feeding the NNA with samples of extracted metrics and desired UDP identification flags allows the network to adjust its weights and bias values to adapt to the pattern of UDP identification problem. In our study, we feed the NNA with samples of τ_{rms}, r, and ξ_{hyb} as inputs and binary target values of 1 and 0, 1 for the case of UDP condition and 0 for the case of DDP.

Once the NNA is trained, we can simulate the unknown channel profiles by feeding their extracted τ_{rms_i}, r_i, and ξ_i to the NNA to identify the UDP condition. As a small experiment, for the purpose of training and simulation we used 400 training channel profiles and 100 unknown channel profiles for simulation, the results of accuracy of the likelihood ratio tests and NNA is summarized in Table 6.1.

Table 6.1: Accuracy of UDP Identification using Likelihood Hypothesis Tests and Neural Network Architecture

Likelihood Ratio	$CorrectDecision$
τ_m	72.40%
P_{tot}	78.30%
ξ_{hyb}	85.48%
δ	92.00%

It can be observed that amongst individual metrics, the hybrid metric performs superior, as expected, while the other two yield reasonable identification pointers. The overall performance of NNA, however, is better than individual metrics, as the NNA has adapted itself to the classification problem and the weights are adjusted accordingly.

6.1.1 NNA Parameters

The performance of NNA highly depends on its parameters with which it has been initialized. In this section we analyze the effects of number of training points on the overall performance of the NNA for indoor localization problem. Training an NNA is similar to the procedure of training RSS-based fingerprinting localization systems. In RSS-based systems based on fingerprinting technique [Eka07], initial sample measurements have to be taken to build the online database. At each receiver location, the client measures the received power from each access point and assigns the set of measurement to the coordinates of the receiver location. In the offline phase, a new set of power measurements are taken and compared with the database. The positioning system, therefore, decides on the best possible estimate of the coordinates of the new receiver location. Similar procedure is involved in initialization of an NNA. In the online phase, some initial measurements have to be taken and their respective parameters have to be stored as the inputs of the NNA along with the UDP flag of the current receiver location as the output of the NNA. The NNA then trains itself with the sample inputs and outputs and adjusts its weights and biases. When a new profile is observed by the NNA, it simulates the output based on the previous adjusted weights and biases. To analyze the performance of the NNA with different sets of training points, we changed the number of training points of the NNA and recorded the performance of the network. Figure 6.2 illustrates the accuracy of predicting the UDP conditions as a function of number of training points for the three specified cost functions defined in Eqn. 6.3. At first it can be observed that MSE with regularization performs the best.

The small differences between the performance of the network when different cost functions are used are problem specific. For different problems individual cost function might perform superior. However, in the case of UDP identification using

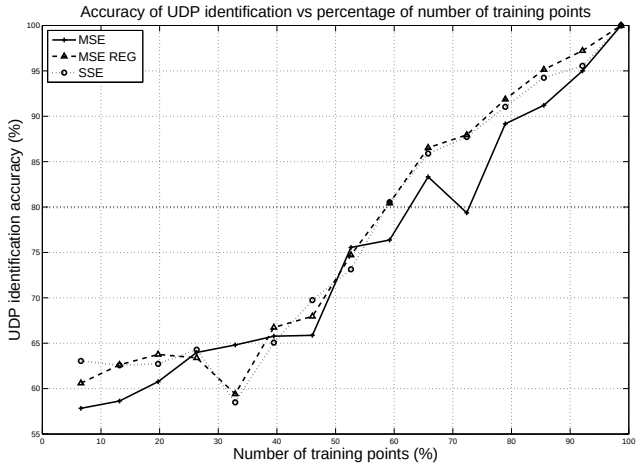

Figure 6.2: Accuracy of UDP identification as a function of number of training points used to train the NNA

propagation parameters of the radio communication MSE with regularization not only performed superior in terms of accuracy but also the convergence time of the network was considerably smaller than the other two. We measured the convergence time of the NNA in terms of epochs to be used to reach a flat cost function plot. In our experiment, MSE and SSE usually needed 50 to 100 epochs to reach the flat plot while MSE with regularization needed fewer epochs, usually in the order of 20 to 40. The target goal of the performance for each cost function is also an important parameter in pattern recognition. Obviously, target goal of MSE cost function is 0. In our experiment we found that performance of 0.1 to 0.11 is desirable for such cost function as performances less than 0.1 causes overfitting of the network and performances more than 0.11 simply do not solve the pattern classification problem. In the case of MSE with regularization, target goal of 0.3 to 0.4 was desirable and SSE worked better with target goals of the order of 17 to 19.

It can also be observed that training the network with few training points results in poor UDP identification. However, even using as few as 10% of total receiver locations results in 60% accuracy in UDP identification. In our research, we chose

to use almost 60% of the total receiver locations corresponding to one transmitter to train the network which results in 80% accuracy in UDP identification.

6.1.2 Generalization of the Network

In another experiment we analyzed the performance of the NNA when generalized to different setup of transmitter and receiver. We used the propagation parameters of all the receiver locations corresponding to the first transmitter as the training set and simulated the UDP identification flag for the other transmitters. Since the scenario between the transmitter locations and receiver locations were completely different, this experiment could lead us to analyze the performance of the network when generalized to other transmitter locations and/or other buildings with similar interior characteristics. The experiment prove to be 75% accurate in predicting the UDP conditions when a completely different set of measurement in a similar indoor environment was used to train the network. It implies that the training phase of NNA can be conducted once and be used for different locations of the transmitter. The results of the experiment is reported in Table 6.2.

Table 6.2: Generalization of UDP Identification

Training Set	**Simulation Set**	Mean of Accuracy	Standard Deviation of Accuracy
Tx_1	Tx_2	73.68%	5.95%
Tx_1	Tx_3	77.31%	11.15%
Tx_2	Tx_1	71.31%	3.76%
Tx_2	Tx_3	67.88%	3.30%
Tx_3	Tx_1	74.20%	2.88%
Tx_3	Tx_2	77.36%	4.49%

6.2 Simulation and Results of Localization using ToA measurement

In 2-D localization, knowledge of three accurate distance measurements from three known reference points (RPs) will be sufficient to accurately locate the mobile terminal with the help of trilateration. An important parameter affecting the performance of the localization system is the number of the RPs used for localization. In this study we consider two different scenarios with two and three RPs. The localization algorithm is described in Section 5.1.1

6.2.1 Localization Scenario and Effects of Mitigation

To emphasize on the importance and significance of the NNA assisted identification of UDP condition, Fig. 6.3 describes localization with only two known RPs in the presence of multipath and blockage (dashed line). The setup was similar to the setup described in sections 5.3.1 and 5.3.2. The RMSE value of localization error is found to be 8.42 m.

Next we examine the UDP identification and mitigation the error associated with such conditions. Identifying the UDP scenarios with the aid of NNA gives us an edge to mitigate the ranging associated with the profile. For this purpose, we selected an NNA with feed-forward backdrop type and Levenberg-Marquardt algorithm. The NNA consisted of two layers with 10 neurons and 1 neuron, respectively. The output function of the hidden layer, i.e. the layer with 10 neurons, was adjusted to hyperbolic tangent sigmoid transfer function while the output function, i.e. $g(n) = \frac{2}{1+e^{-2n}} - 1$ of the second layer was linear transfer function, i.e. $f(n) = n$. The cost function to minimize was considered to be the MSE function described in Eqn. 6.3. After training the network with few extracted metrics of the frequency-

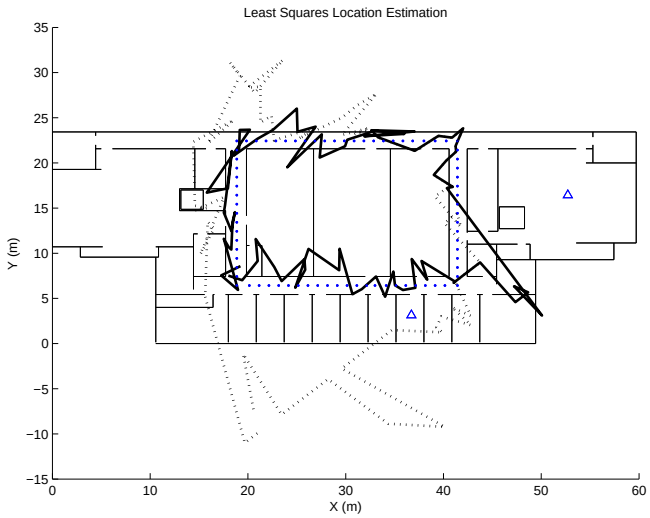

Figure 6.3: Localization error in sample indoor environment for two RPs

domain measurements of the sample receiver locations, we simulated the network with extracted metrics from channel profiles with unknown UDP identification flag. We used to outputs of the simulation as an UDP identification flag. If the output for a specific location was 0, we used the obtained d_{FDP} of the channel profile for localization. However, if the output of the NNA was 1, we considered the channel profile as UDP and mitigated the respective d_{FDP} prior to using it for localization. In order to mitigate the range estimate we subtracted a correction value from d_{FDP}. Since the exact value of the error is not known, the statistics of the ranging error [Ala06b] in such conditions can be used to remedy the distance estimate. A correction value can be subtracted from the observed estimated ranging reading

$$\begin{aligned} \tau_{DP} &\simeq \tau_{FDP} - \varepsilon_{\tau} \\ d_{DP_i} &\simeq d_{FDP_i} - \varepsilon_{d} \end{aligned} \tag{6.4}$$

Mitigating the distance measurement of the antenna pair and employing the idea on the previous scenario results in enhanced localization error observed by

each receiver location and greatly improves the accuracy of the localization system. Figure 6.3 illustrates the results (solid line). It can be observed that identifying the UDP condition and mitigating the ranging error associated with such receiver locations, greatly improves the localization error observed in UDP receiver locations.

The RMSE value of the ranging error has also improved by 60% and has dropped to $3.53\,m$. Although, employing two RPs limits the efficiency of the localization algorithm, as the minimum number of RPs for accurate two-dimensional positioning is three, but it can be observed that the NNA assisted identification of UDP conditions has improved the accuracy of the localization system. However, the identification is not certain for all the receiver locations and occasionally identifies some DDP profiles as UDP and unintentionally subtracts a correction value from their estimated ToA which will result in accuracy degradation at some receiver locations. Nevertheless, as Fig. 6.3 illustrates, the identification/mitigation algorithm can enhance the accuracy of the localization algorithm majority of the time. Figure 6.4 compares the CDF of localization error associated with each scenario. Again, it can be observed that, although, localization error has increased at certain receiver locations, on average it has helped the algorithm to identify the UDP conditions and mitigate their ranging measurement to obtain a more accurate location estimation.

To further analyze the effects of UDP identification, we set up another experiment with the same scenario but with three RPs. Intuitively, the addition of the third RP to the previous scenarios had to enhance the performance of the localization system and algorithm. Figure 6.5 explains the details of the receiver locations and transmitter locations, i.e. RPs.

Similar to the previous experiment, we initially trained the NNA with extracted metrics from respective channel profiles, from frequency-domain measurement, for few receiver locations with their pre-known UDP identification flag and then consid-

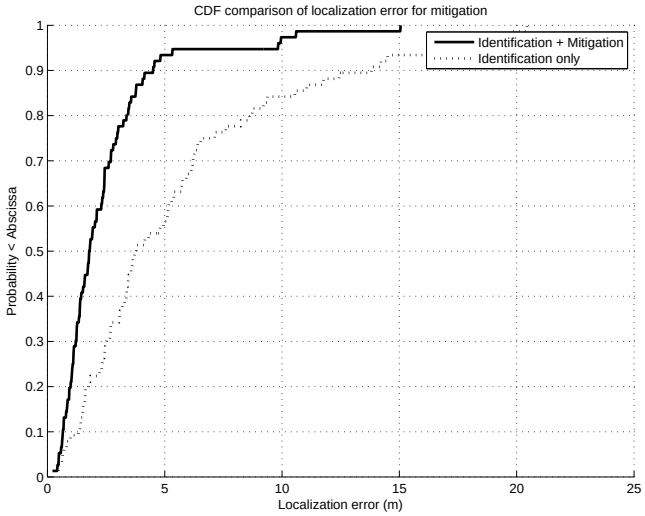

Figure 6.4: CDF of localization error for the sample indoor environment for two RPs

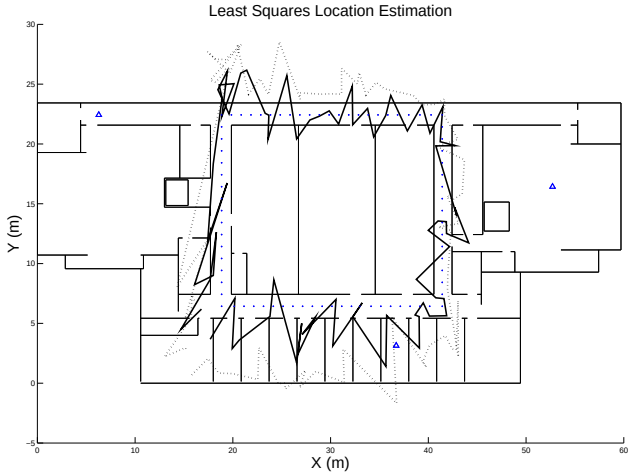

Figure 6.5: Localization error in sample indoor environment for three RPs

ered the rest of the receiver locations as unknown input for the NNA and let NNA simulate them for UDP identification. Based on the simulation, if the output of the NNA was 0 we used the respective d_{FDP} for localization while we mitigated the d_{FDP} for the channel profiles under UDP condition by subtracting a correction value and then use them for localization. Figure 6.5 explains the results of the experiment and it can be observed that indeed the addition of the third RP has helped the accuracy of the localization algorithm. Comparing the dashed line to the case with two RPs, shows that the accuracy of the system has improved. Similar comparison can be observed for the solid line where UDP identification and mitigation has been considered. It can also be seen that identification of the UDP conditions and mitigating the ranging error associated with such channel profiles can improve the accuracy of the system. The RMSE value of error for the case of three RPs and traditional localization algorithm, i.e. without UDP identification and mitigation, was $4.94\,m$ which compared to the case with two RPs, i.e. RMSE of $8.42\,m$ shows 60% improvement. Adding UDP identification method and mitigating the ranging error drops the RMSE value to $2.31\,m$ which is another 50% of improvement. Overall, the RMSE value of localization error can be reduced from $8.42\,m$ to $2.31\,m$. Figure 6.6 compares the CDF of localization error for the three RPs experiment for traditional algorithm and UDP identification and mitigation cases. It can be observed that identification of UDP spots greatly enhance the quality of the localization system.

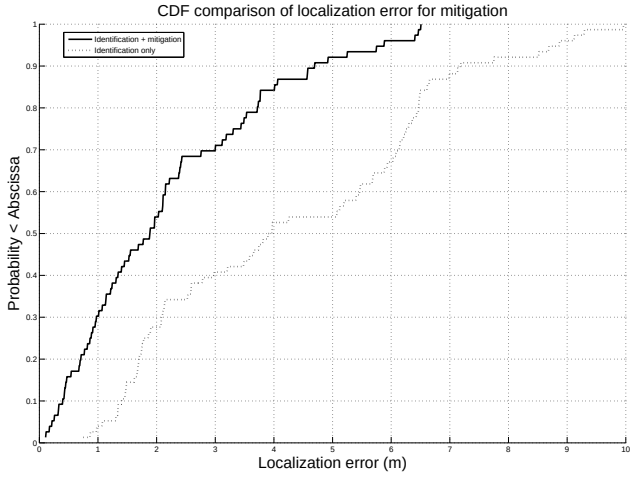

Figure 6.6: CDF of localization error for the sample indoor environment for three RPs

Chapter 7

Conclusions and Future Work

This chapter summarizes the contributions of the research presented in this dissertation and suggests directions for future work.

7.1 Contributions

This dissertation studies two major open problem in the field of indoor localization, specifically ToA-based indoor localization systems.

7.1.1 Modeling the Dynamic Behavior of the Direct Path Component

In the first contribution of this dissertation, we presented a novel application of a Markov chain for modeling the dynamic behavior of the ranging error in a typical indoor localization application which assists us in the design and performance evaluation of tracking capabilities of such systems. The parameters of the Markov model and exponential waiting times were obtained from analytical derivation based on real UWB measurement previously conducted on the 3^{rd} floor of the $AKLabs$. The parameters of distributions of ranging error observed in each Markov state were extracted from real-time frequency-domain wideband measurements as well as empirical data obtained from 14000 channel impulse responses on the 3^{rd} floor of the

AK Labs at WPI. We extended to results to include the spatial correlation of ranging error to previously observed ranging error values in the same state by considering the autocorrelation function of the ranging error for different states. The results of simulation for the dynamic behavior of ranging error using the Markov chain were shown to provide close agreement with the results of empirical data. The results of this contribution has been published in *IEEE Communications Letters*, *EURASIP Journal on Advances in Signal Processing*, *IEEE Wireless Communications Magazine*, *Bechtel Telecommunications Technical Journal*, *IEEE Wireless Communications and Networking Conference*, and *IEEE Vehicular Technology Conference*.

7.1.2 UDP Identification

In the second contribution of this dissertation we introduced two different methodologies to identify the UDP condition and mitigate the large ranging errors associated with it. We proposed the use of power and time metrics from the received channel profile to obtain the likelihood functions for binary hypothesis testing. Comparing the outcome of the hypothesis tests to a certain threshold determines if a receiver is in DDP or UDP condition. In addition to the binary hypothesis tests, the aforementioned metrics can be used to train a NNA for the classification problem. Once trained, the NNA can accurately identify the UDP conditions. Once such condition with large ranging error is identified, the ranging error associated with it can be mitigated according to the statistics of the ranging error observed in such conditions and the accuracy of the localization algorithm can be reasonably improved. The results of this research effort were published in *International Journal of Wireless Information Networks*, *IEEE Global Communications Conference*, and *IEEE International Symposium on Personal, Indoor, and Mobile Radio Communications*.

7.1.3 Other Contributions

In addition to the major contributions described above the following are other contributions of this dissertation mainly focused on the small details of the proposed algorithms and models.

- In addition to conducting real-time frequency-domain wideband measurement and simulating the CIR using RT to obtain the channel profile, we compared the results of measurement and RT in terms of total power and ranging error. The preliminary results illustrated that the addition of metallic details of the floor plan of the building under study could improve the comparative results of total power and ranging error.

- Previous research categorizes the receiver locations in an indoor environment into LoS/NLoS conditions. Recent studies revealed that NLoS condition can be further broken down into DDP/UDP conditions in which the condition depends on the presence or absence of the DP component. It has also been shown that NC class of receive location exists in indoor environment. We further classify the UDP conditions into NUDP and SUDP conditions based on the geometry of the building and type of ranging error and present comprehensive receiver location classification.

7.2 Future Research Directions

The dynamic model for the behavior of the DP component and algorithms to identify the UDP conditions proposed in this dissertation can be further investigated and generalized. The following are some future steps that can be performed to improve the overall quality of the indoor localization systems.

7.2.1 Comprehensive Dynamic Model for MPCs

The dynamic model proposed in this dissertation focuses mainly on the DP component and its dynamic behavior. The model can be generalized to include all the multipath components and their dynamic behavior. The model can assign a birth/death process, a two state Markov chain, to model the behavior of MPCs as they appear and disappear in the channel profile. The rates of appearance and disappearance can be analytically derived and modeled and then verified by simulation.

7.2.2 UDP Identification Generalization

To further improve the accuracy of the UDP identification algorithm, we can improve the accuracy of the binary hypothesis tests by investigating several channel propagation parameters. For example, the other moments of the time-characteristics of the channel, other power metrics, and frequency-domain characteristics can be examined and employed in binary hypothesis testing.

In order to improve the accuracy of the NNA algorithm, we can employ a larger set of metrics and construct a larger database as the input of the NNA. In that case, NNA can identify the pattern of the UDP occurrence more efficiently. The mitigation process can further be improved by adopting several mitigation techniques as well. The combination of the two steps can enhance both the accuracy of the UDP identification and localization system.

Appendix A

Ray Tracing and Measurement Channel Profile Comparison - Original Floor Plan

The point to point comparison of the RT channel profiles with measurement channel profile for the 10 point corridor scenario.

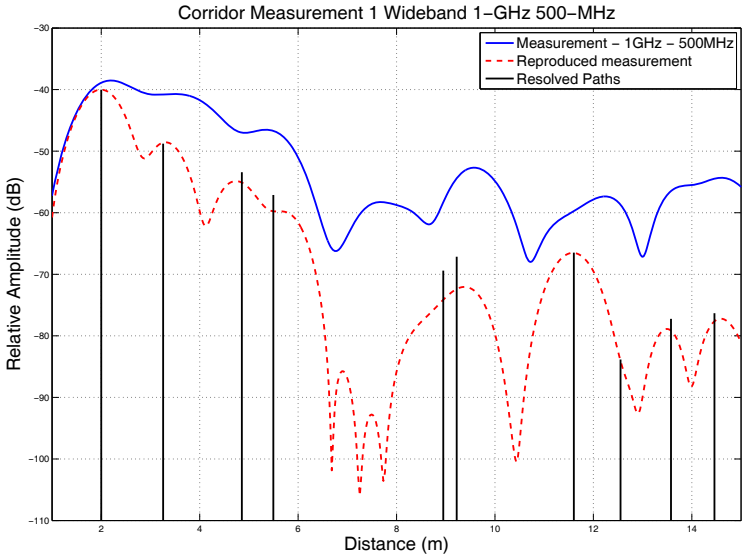

Figure A.1: Comparison of the channel profiles obtained from measurement and RT - Original floor plan without adjustments of the door and metallic shelf - Point 1

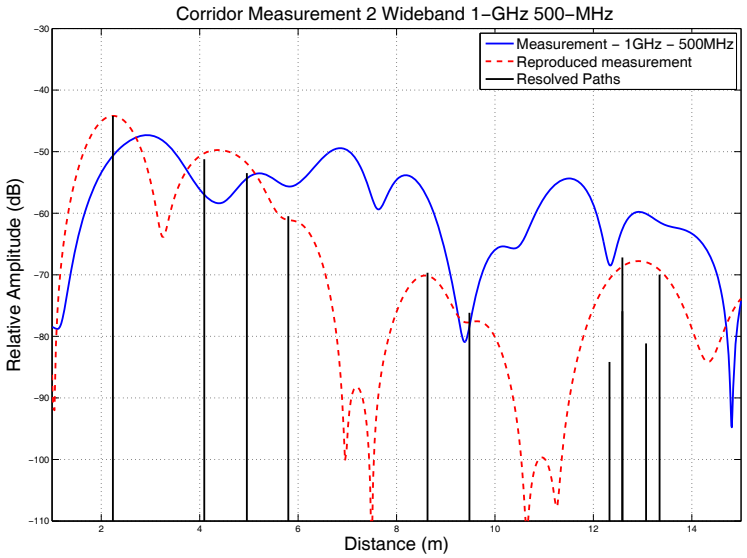

Figure A.2: Comparison of the channel profiles obtained from measurement and RT - Original floor plan without adjustments of the door and metallic shelf - Point 2

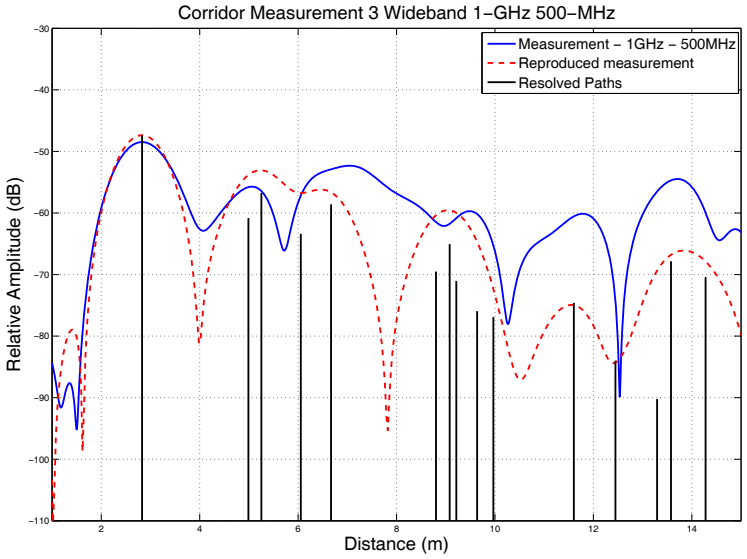

Figure A.3: Comparison of the channel profiles obtained from measurement and RT - Original floor plan without adjustments of the door and metallic shelf - Point 3

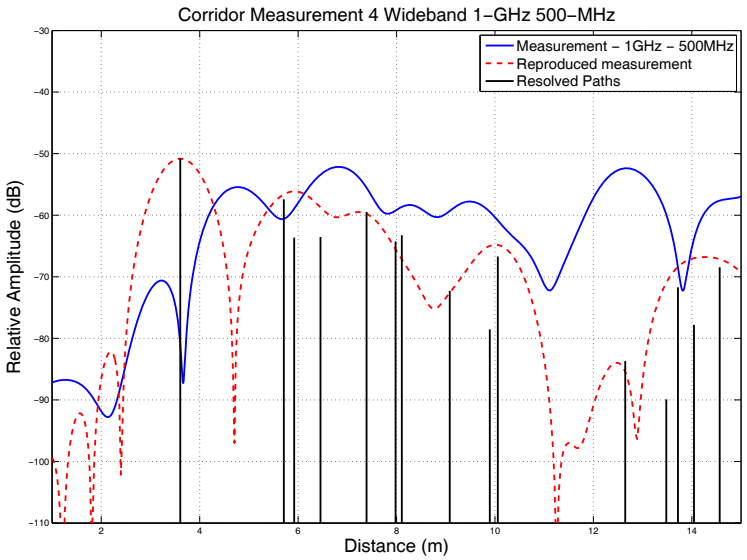

Figure A.4: Comparison of the channel profiles obtained from measurement and RT - Original floor plan without adjustments of the door and metallic shelf - Point 4

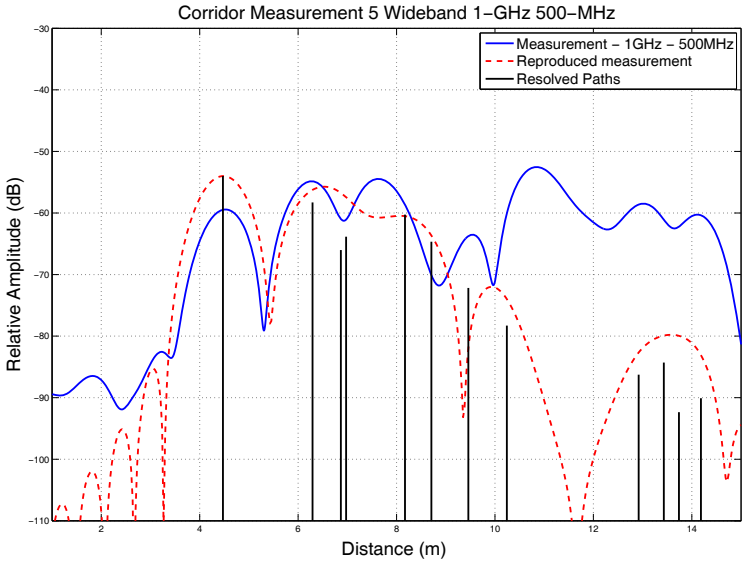

Figure A.5: Comparison of the channel profiles obtained from measurement and RT - Original floor plan without adjustments of the door and metallic shelf - Point 5

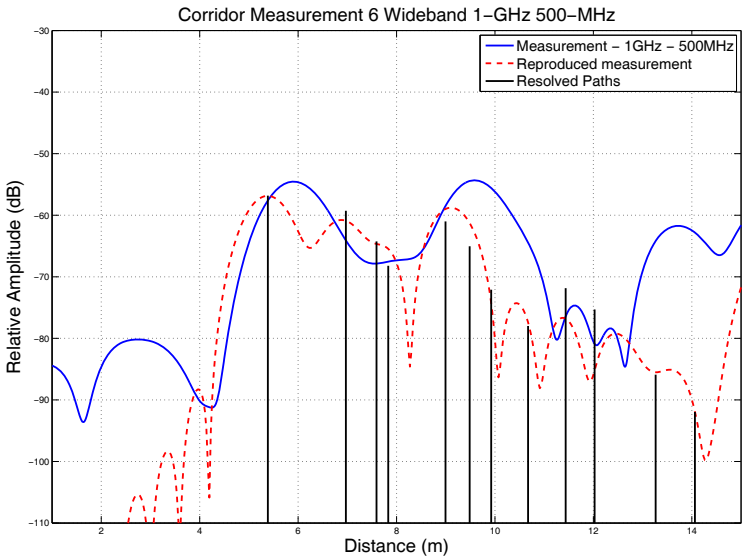

Figure A.6: Comparison of the channel profiles obtained from measurement and RT - Original floor plan without adjustments of the door and metallic shelf - Point 6

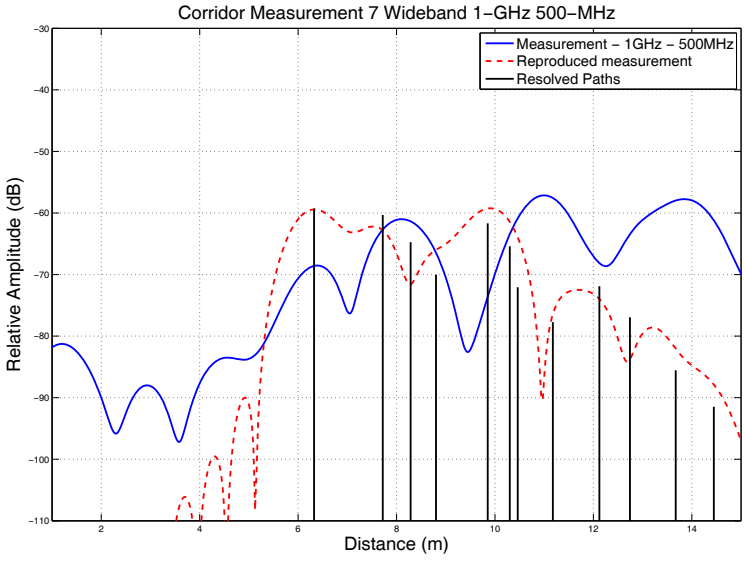

Figure A.7: Comparison of the channel profiles obtained from measurement and RT - Original floor plan without adjustments of the door and metallic shelf - Point 7

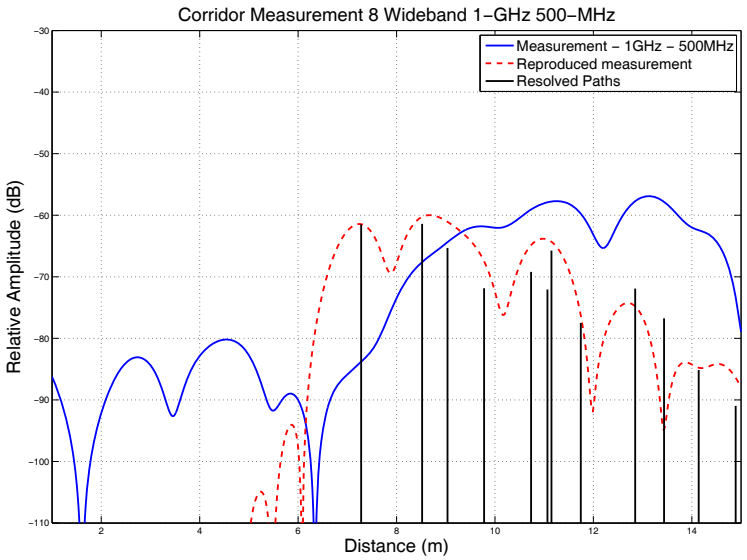

Figure A.8: Comparison of the channel profiles obtained from measurement and RT - Original floor plan without adjustments of the door and metallic shelf - Point 8

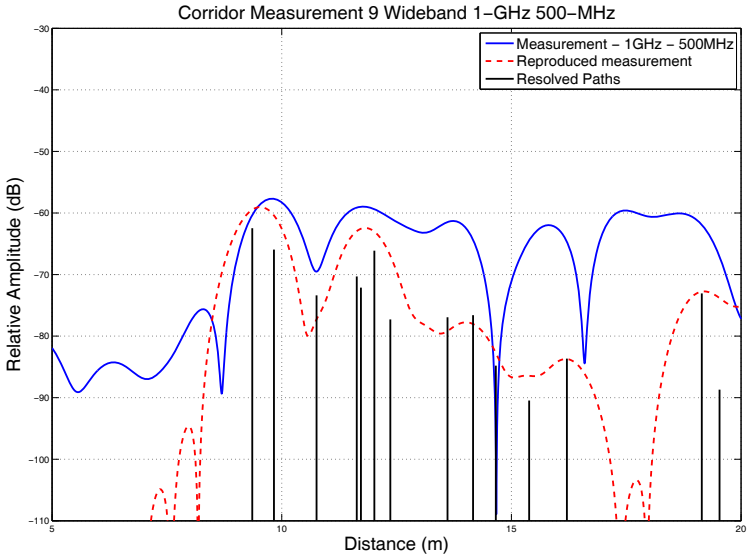

Figure A.9: Comparison of the channel profiles obtained from measurement and RT - Original floor plan without adjustments of the door and metallic shelf - Point 9

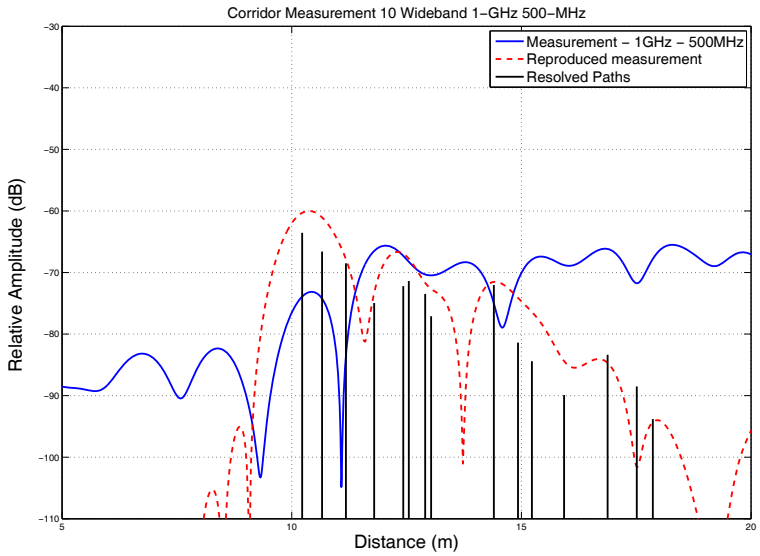

Figure A.10: Comparison of the channel profiles obtained from measurement and RT - Original floor plan without adjustments of the door and metallic shelf - Point 10

Appendix B

Ray Tracing and Measurement Channel Profile Comparison - Modified Floor Plan

In the original floor plan the locations of the metallic door behind the transmitter and the metallic shelf was not adjusted. After adjusting these parameters in the floor plan used in the RT software we repeated the same scenario and compared the channel profiles obtained from measurement and RT.

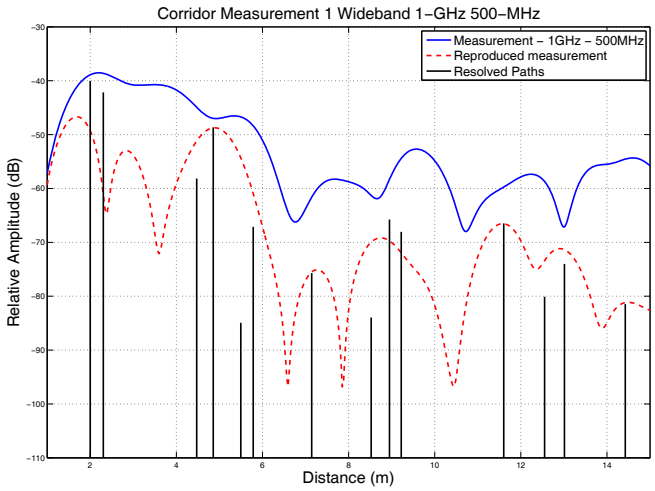

Figure B.1: Comparison of the channel profiles obtained from measurement and RT - Revised floor plan with adjustments of the door and metallic shelf - Point 1

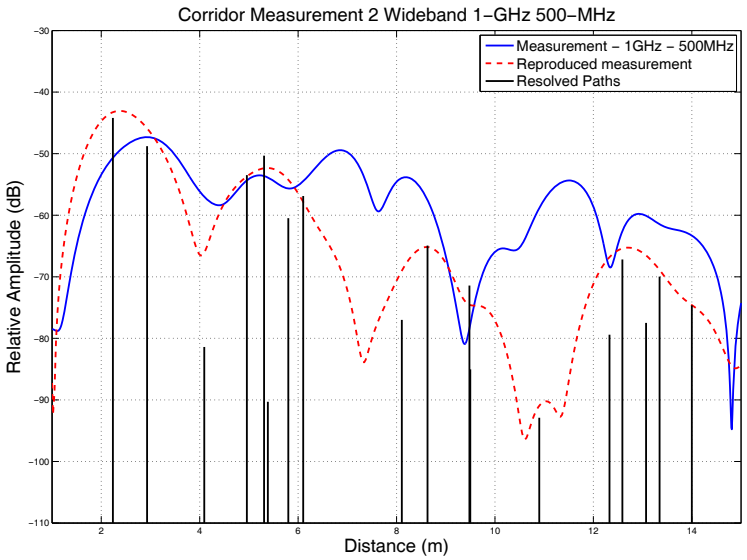

Figure B.2: Comparison of the channel profiles obtained from measurement and RT - Revised floor plan with adjustments of the door and metallic shelf - Point 2

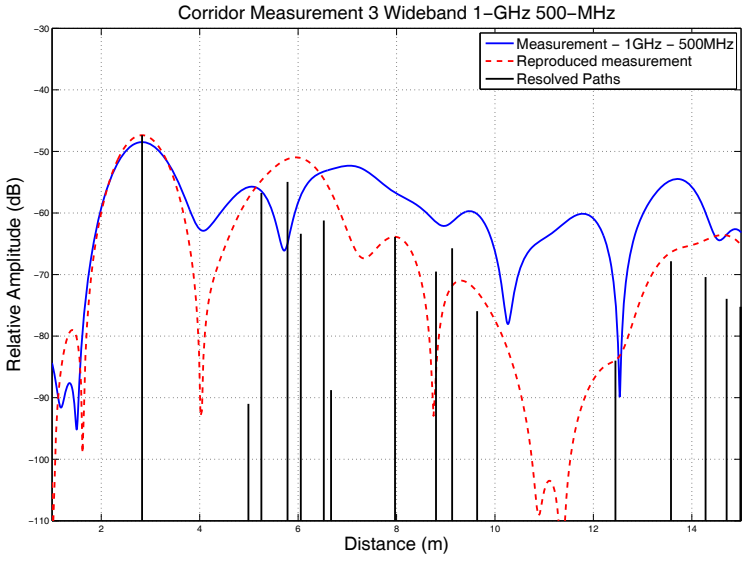

Figure B.3: Comparison of the channel profiles obtained from measurement and RT - Revised floor plan with adjustments of the door and metallic shelf - Point 3

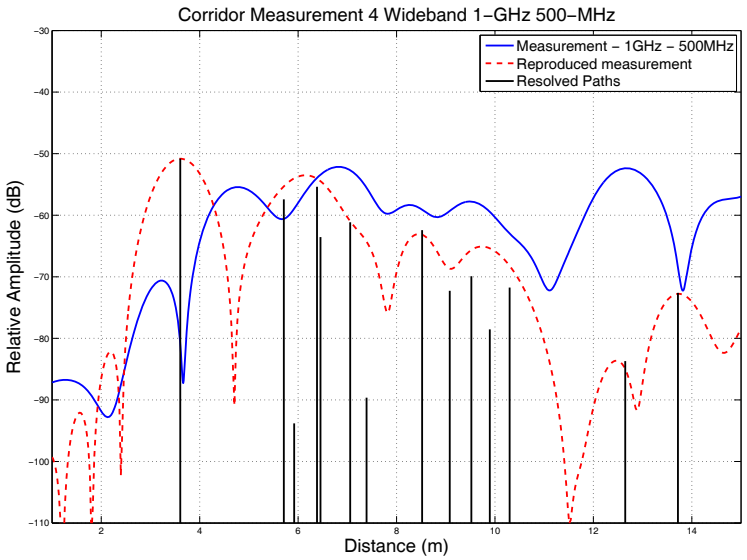

Figure B.4: Comparison of the channel profiles obtained from measurement and RT - Revised floor plan with adjustments of the door and metallic shelf - Point 4

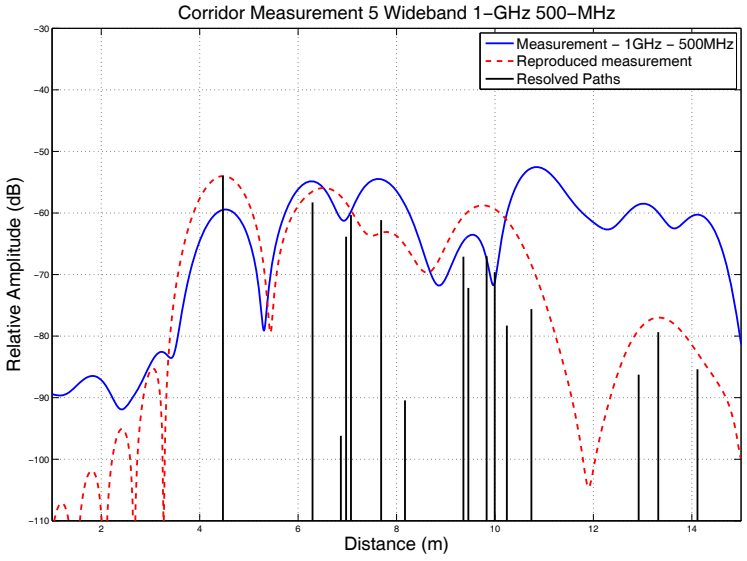

Figure B.5: Comparison of the channel profiles obtained from measurement and RT - Revised floor plan with adjustments of the door and metallic shelf - Point 5

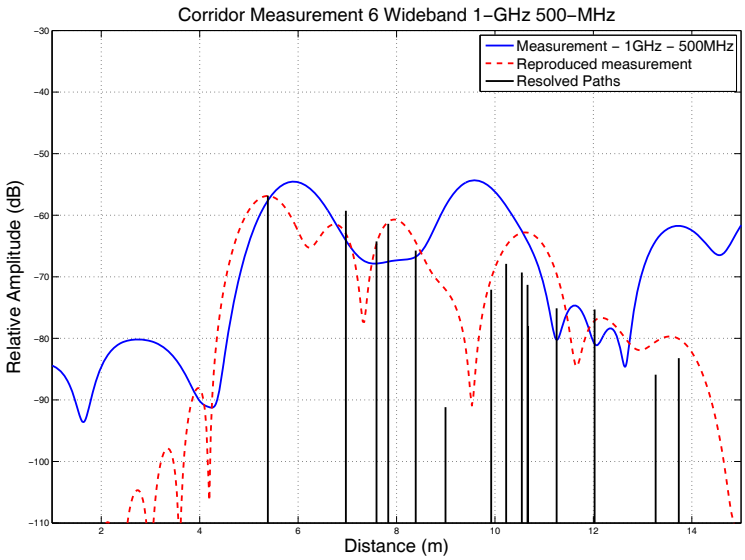

Figure B.6: Comparison of the channel profiles obtained from measurement and RT - Revised floor plan with adjustments of the door and metallic shelf - Point 6

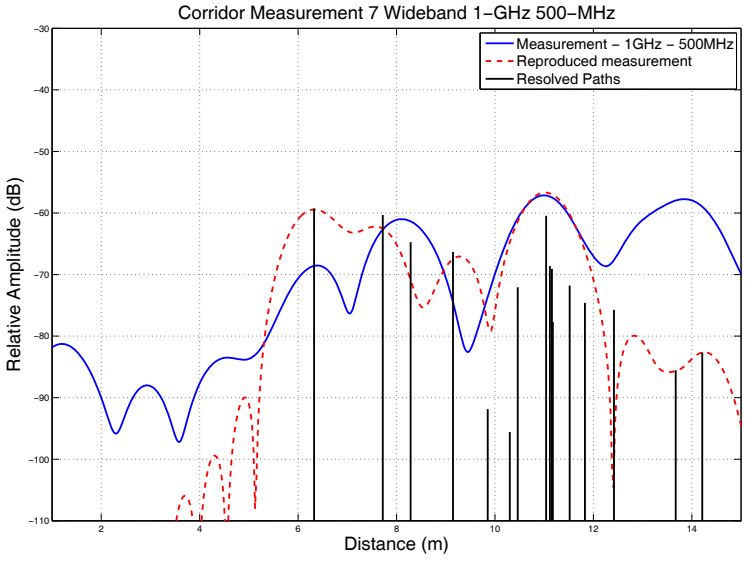

Figure B.7: Comparison of the channel profiles obtained from measurement and RT - Revised floor plan with adjustments of the door and metallic shelf - Point 7

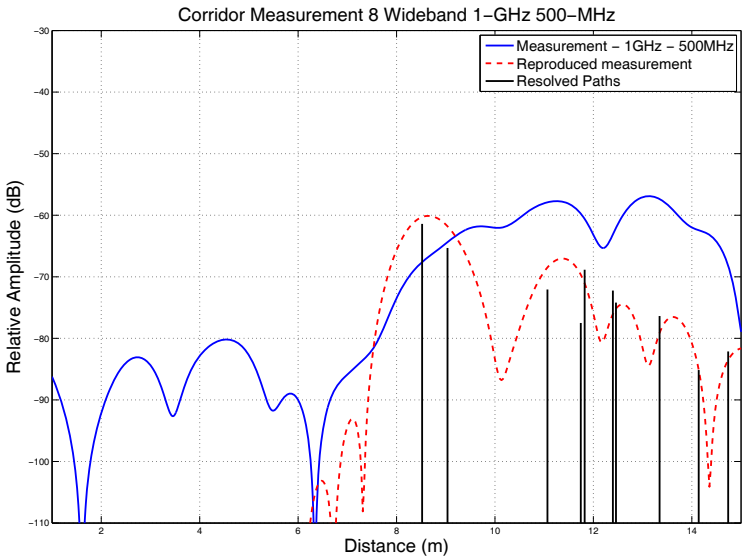

Figure B.8: Comparison of the channel profiles obtained from measurement and RT - Revised floor plan with adjustments of the door and metallic shelf - Point 8

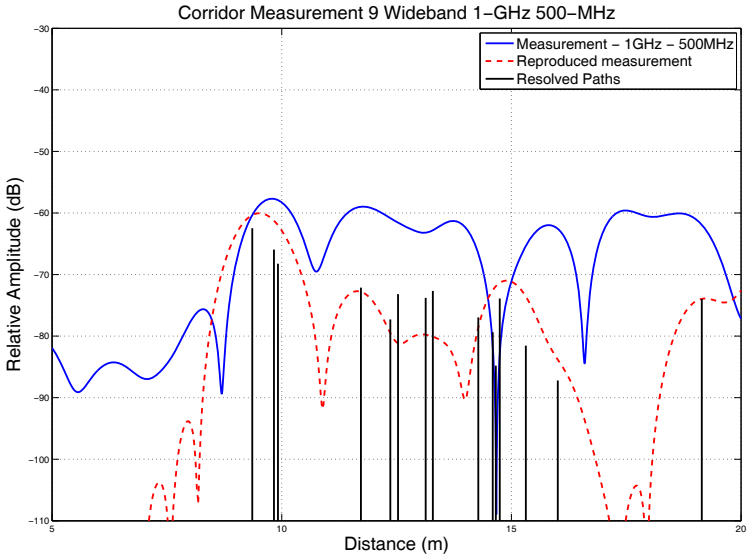

Figure B.9: Comparison of the channel profiles obtained from measurement and RT - Revised floor plan with adjustments of the door and metallic shelf - Point 9

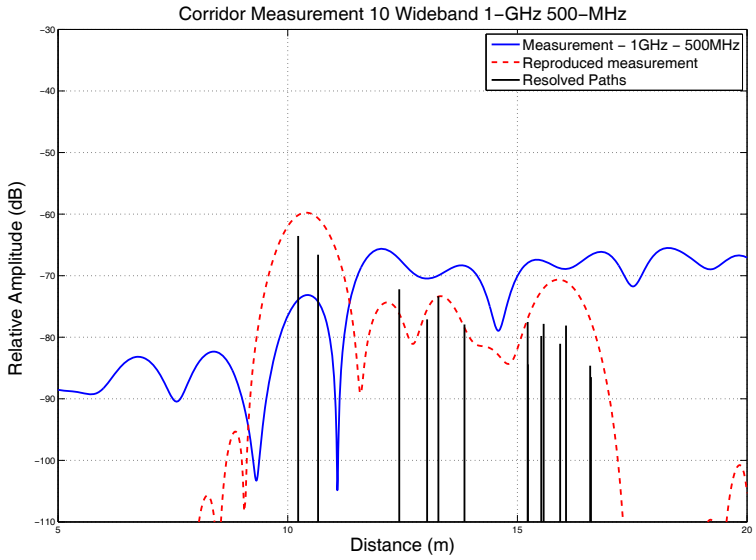

Figure B.10: Comparison of the channel profiles obtained from measurement and RT - Revised floor plan with adjustments of the door and metallic shelf - Point 10

Appendix C

Ray Tracing and Measurement Channel Profile Comparison - UWB Measurement

We then shift our focus to compare the channel profiles obtained from UWB measurement system with RT channel profiles to obtain better accuracy in resolving the MPCs and mitigating ranging error.

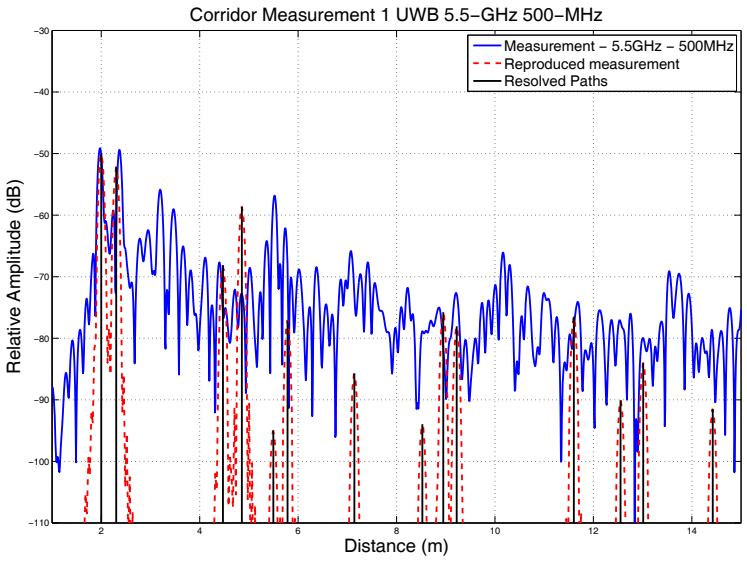

Figure C.1: Comparison of the channel profiles obtained from UWB measurement and RT - Revised floor plan with adjustments of the door and metallic shelf - Point 1

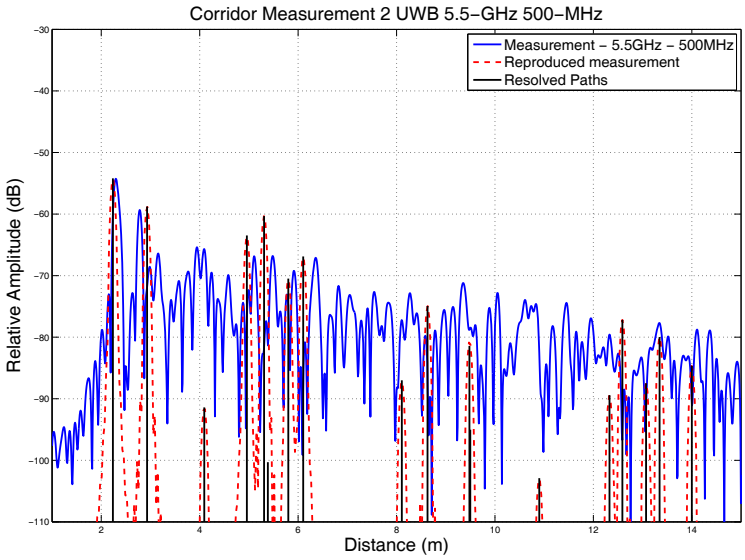

Figure C.2: Comparison of the channel profiles obtained from UWB measurement and RT - Revised floor plan with adjustments of the door and metallic shelf - Point 2

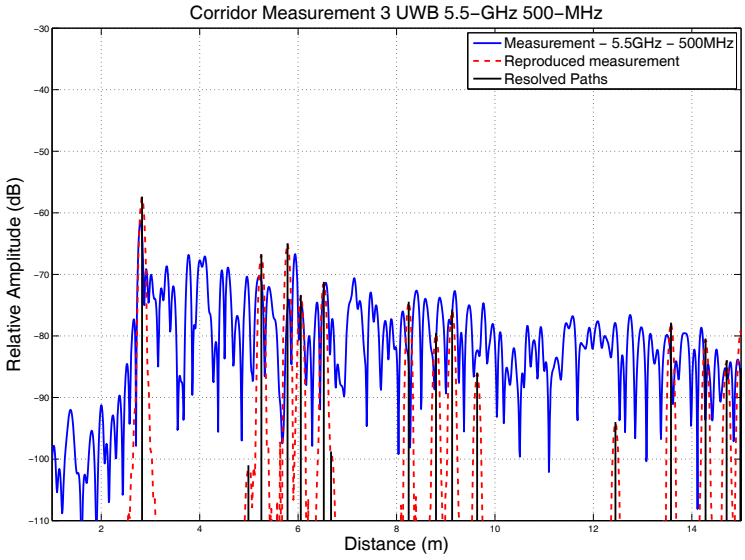

Figure C.3: Comparison of the channel profiles obtained from UWB measurement and RT - Revised floor plan with adjustments of the door and metallic shelf - Point 3

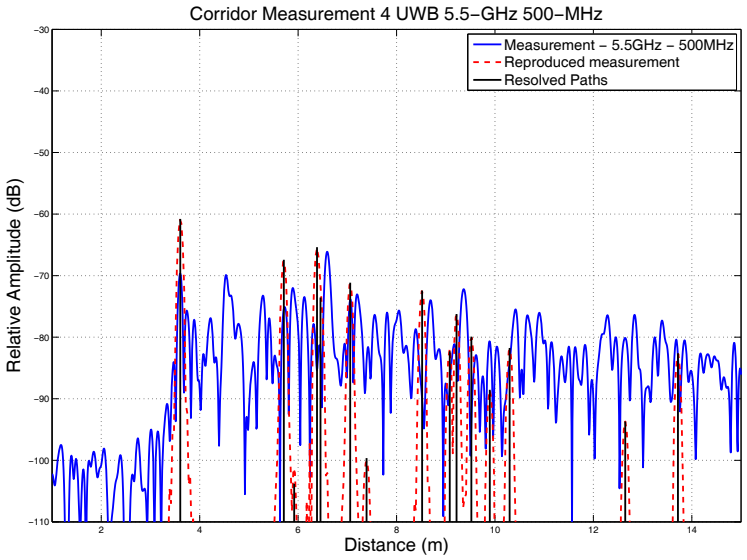

Figure C.4: Comparison of the channel profiles obtained from UWB measurement and RT - Revised floor plan with adjustments of the door and metallic shelf - Point 4

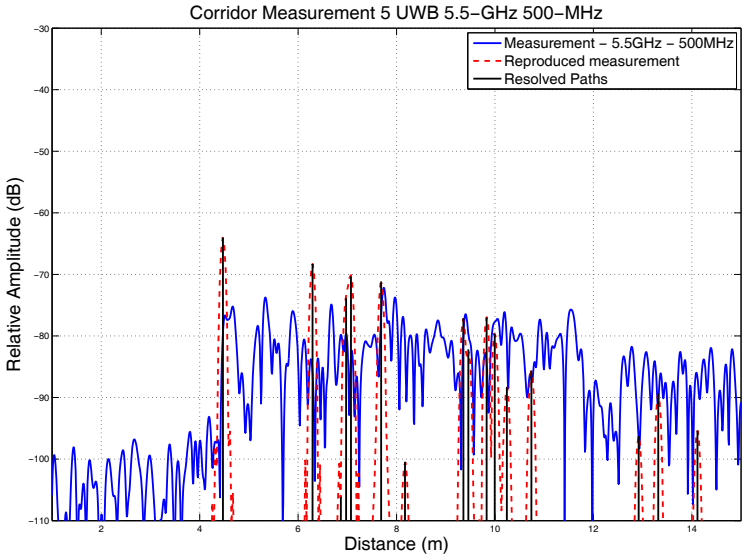

Figure C.5: Comparison of the channel profiles obtained from UWB measurement and RT - Revised floor plan with adjustments of the door and metallic shelf - Point 5

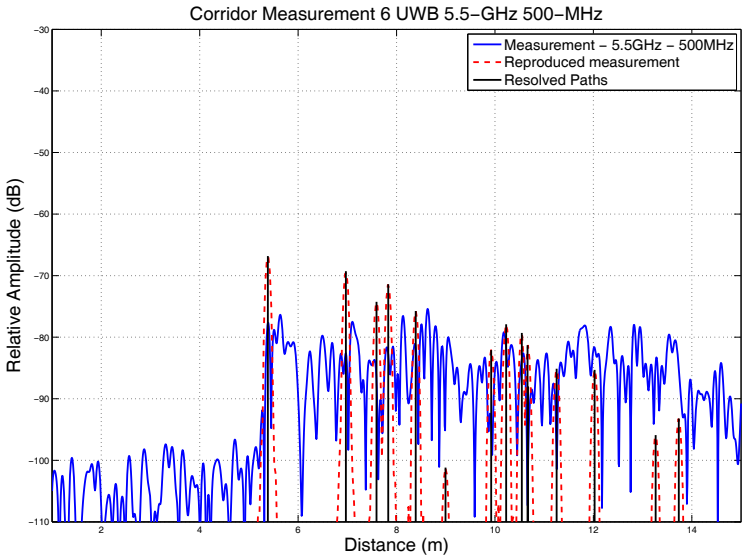

Figure C.6: Comparison of the channel profiles obtained from UWB measurement and RT - Revised floor plan with adjustments of the door and metallic shelf - Point 6

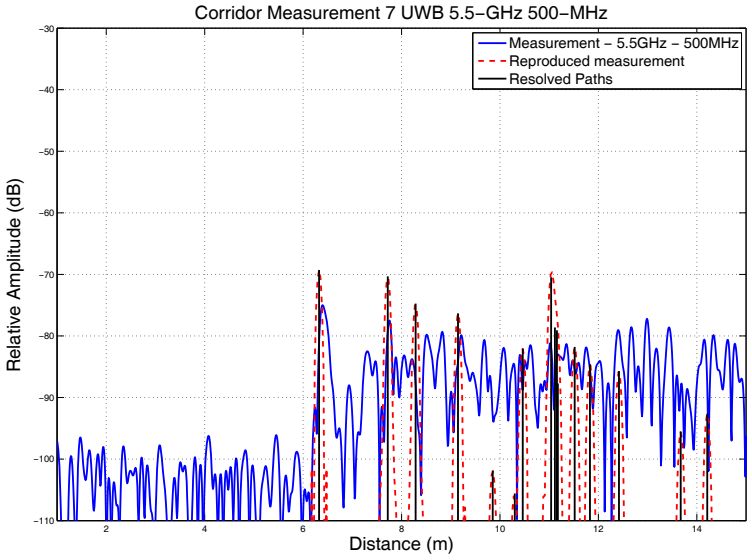

Figure C.7: Comparison of the channel profiles obtained from UWB measurement and RT - Revised floor plan with adjustments of the door and metallic shelf - Point 7

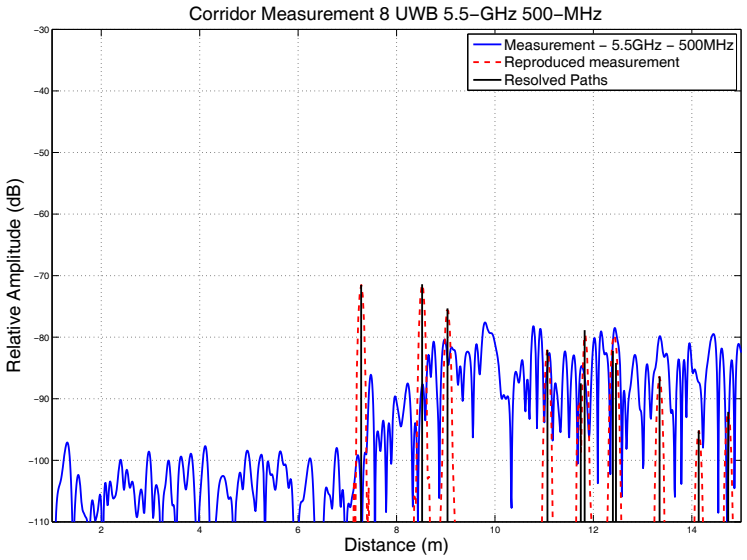

Figure C.8: Comparison of the channel profiles obtained from UWB measurement and RT - Revised floor plan with adjustments of the door and metallic shelf - Point 8

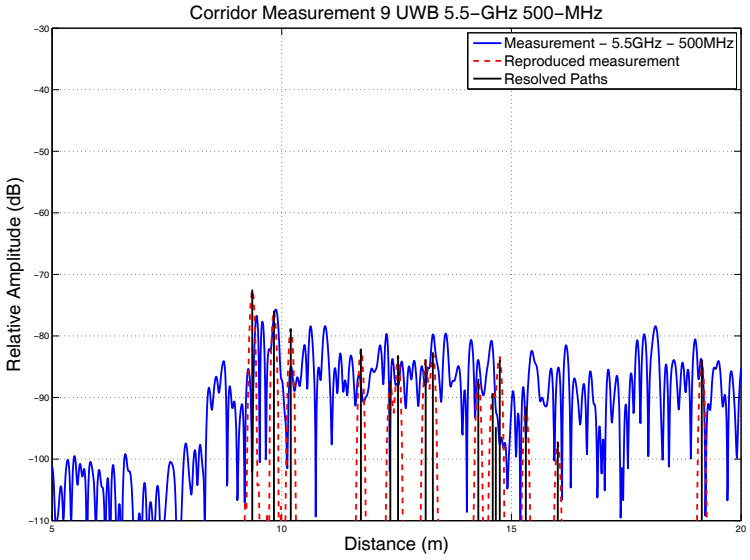

Figure C.9: Comparison of the channel profiles obtained from UWB measurement and RT - Revised floor plan with adjustments of the door and metallic shelf - Point 9

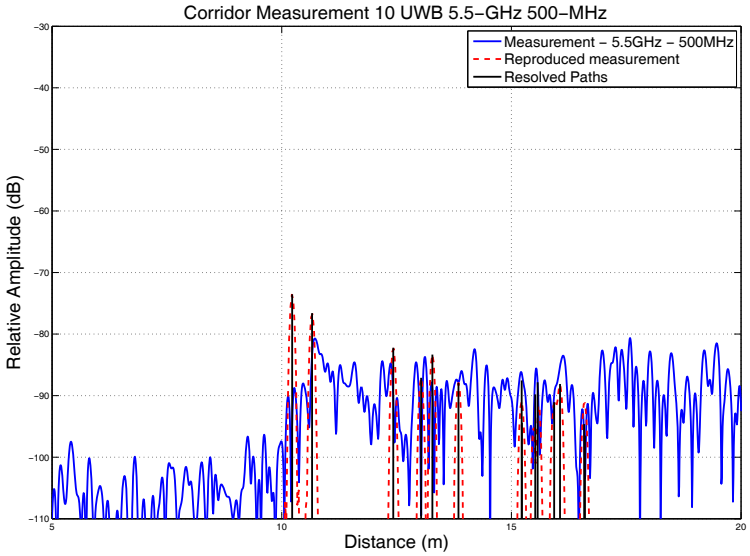

Figure C.10: Comparison of the channel profiles obtained from UWB measurement and RT - Revised floor plan with adjustments of the door and metallic shelf - Point 10

References

[Ala03] Bardia Alavi & Kaveh Pahlavan, "Modeling of the Distance Error for Indoor Geolocation". *In IEEE Wireless Communications and Networking Conference, WCNC*, vol. 1, pp. 668–672, March 2003. 56, 57, 86

[Ala05] ———, "Analysis of Undetected Direct Path in Time of Arrival Based UWB Indoor Geolocation". *In IEEE Vehicular Technology Conference*, vol. 4, pp. 2627– 2631, 2005. 53

[Ala06a] Bardia Alavi, *Distance Measurement Error Modeling for Time-of-Arrival Based Indoor Geolocation*. Ph.D. thesis, Worcester Polytechnic Institute, 2006. 2, 3, 9, 10, 11, 17, 46, 50, 51, 52, 53, 55, 62, 87

[Ala06b] Bardia Alavi & Kaveh Pahlavan, "Modeling of the Distance Measure Error using UWB Indoor Radio Measurement". *In IEEE Communication Letter*, **vol. 10, no. 4**, pp. 275–277, April 2006. 2, 11, 50, 56, 63, 79, 106, 120

[Als04] Nayef Ali Alsindi & Kaveh Pahlavan, "Performance of TOA Estimation Algorithms in Different Indoor Multipath Conditions". *In IEEE Wireless Communications and Networking Conference, WCNC*, pp. 495–500, March 2004. 53

[Als07a] Nayef Ali Alsindi, Bardia Alavi, & Kaveh Pahlavan, "Measurement and Modeling of UWB TOA-based Ranging in Indoor Multipath Environments", June 2007, submitted to IEEE Transactions on Vehicular Technology. 56, 59, 87

[Als07b] ———, "Spatial Characteristics of UWB TOA-based Ranging in Indoor Multipath Environments". *In IEEE International Symposium on Personal Indoor and Mobile Radio Communications, PIMRC*, September 2007. 56, 59, 87

[And93] Harry R. Anderson, "A Ray-Tracing Propagation: Model for Digital Broadcast Systems in Urban Areas". *In IEEE Transactions on Broadcasting*, **vol. 39, no. 3**, pp. 309–317, September 1993. 16

[Bah00a] Paramvir Bahl & Venkata N. Padmanabhan, "RADAR: An in-Building RF-Based User Location and Tracking System". *In Proceedings of IEEE INFOCOM Conference*, vol. 2, pp. 775–784, March 2000. 2

[Bah00b] Paramvir Bahl, Venkata N. Padmanabhan, & Anand Balachandran, "Enhancements to the RADAR User Location and Tracking System". *Tech. Rep. MSR-TR-00-12*, Microsoft Research Laboratory, February 2000. 2

[Bat02] Roberto Battiti, Alessandro Villani, & Thang Le Nhat, "Neural Network Models for Intelligent Networks: Deriving the Location from Signal Patterns". *In Autonomous Intelligent Networks and Systems Symposium*, 2002. 14

[Ben98] Stephen E. Bensley & Behnaam Aazhang, "Maximum Likelihood Synchronization of a Single User for Code-Divistion Multiple Access Com-

munication Systems". *In IEEE Transactions of Communications*, **vol. 46, no. 3**, pp. 392–399, March 1998. 73

[Bur02] Kenneth P. Burnham & David R. Anderson, *Model Selection and Multimodel Inference: A Practical Information-Theoretic Approach*. 2nd edn., New York: Springer, 2002. 59, 60

[Cas02] Dajana Cassioli, Moe Z. Win, & Andreas F. Molisch, "The Ultra-Wide Bandwidth Indoor Channel: from Statistical Model to Simulations". *In IEEE Transactions on Signal Processing*, **vol. 20**, August 2002. 4, 11, 62

[Che99] Pi-Chun Chen, "A Non-Line-of-Sight Error Mitigation Algorithm in Location Estimation". *In IEEE Wireless Communications and Networking Conference, WCNC*, vol. 1, pp. 316–320, September 1999. 2

[Con05] Li Cong & Weihua Zhuang, "Non Line-of-Sight Error Mitigation in Mobile Location". *In IEEE Transactions on Wireless Communications*, **vol. 4, no. 2**, pp. 1536–1276, March 2005. 12

[Dav68] William C. Davidon, "Variance Algorithm for Minimization". *In Computer Journal*, **vol. 10**, 1968. 87

[Ded05] George Dedes & Andrew G. Dempster, "Indoor GPS positioning: Challenges and Opportunities". *In IEEE 62nd Vehicular Technology Conf.*, pp. 412–415, September 2005. 1

[Dem07] Howard Demuth, Mark Beale, & Martin Hogan, "Neural Network Toolbox, User's Guide", 2007, URL http://www.mathworks.com/access/helpdesk/help/pdf_doc/nnet/nnet.pdf. 113, 114, 115

[Den04] Benoit Denis & Norbert Daniele, "NLOS Ranging Error Mitigation in a Distributed Positioning Algorithm for Indoor UWB Ad-Hoc Networks". *In IEEE International Workshop on Wireless Ad-Hoc Networks, IWWAN*, pp. 356–360, May-June 2004. 11, 50, 56, 57, 86

[Eka07] Ekahau, "Ekahau Positioning Engine", 2007, URL http://www.ekahau.com. 116

[Fal06] Chiara Falsi, Davide Dardari, Lorenzo Mucchi, & Moe Z. Win, "Time of Arrival Estimation for UWB Localizers in Realistic Environments". *In EURASIP Journal on Applied Signal Processing*, **vol. 2006**, 2006. 3, 11

[Fon01] Robert J. Fontana, "Advances in Ultrawideband Indoor Geolocation Systems". *In Third Workshop on WLAN*, September 2001. 2

[Gez03] Sinan Gezici, Hisashi Kobayashi, & H. Vincent Poor, "Nonparametric Non Line-of-Sight Identification". *In IEEE Vehicular Technology Conference*, vol. 4, pp. 2544–2548, 2003. 12

[Gez05] Sinan Gezici, Zhi Tian, Georgios B. Giannakis, Hisashi Kobayashi, Andreas F. Molisch, H. Vincent Poor, & Zafer Sahinoglu, "Localization via Ultra-Wideband Radios". *In IEEE Signal Processing Magazine*, **vol. 22, no. 4**, pp. 54–69, 2005. 3, 11

[Gha04] Saeed S. Ghassemzadeh, Rittwik Jana, Christopher W. Rice, William Turin, & Vahid Tarokh, "Measurement and Modeling of an Ultra-Wide Bandwidth Indoor Channel". *In IEEE Transactions of Communications*, **vol. 52, no. 10**, pp. 1786–1796, October 2004. 11

[Gha05] Saeed S. Ghassemzadeh, L. J. Greenstein, A. Kavčič, T. Sveinsson, & Vahid Tarokh, "UWB Delay Profile Models for Residential and Commercial Indoor Environments". *In IEEE Transactions on Vehicular Technology*, **vol. 54, no. 4**, pp. 1235–1244, July 2005. 11, 56

[Guv05] Isamil Guvenc & Zafer Sahinoglu, "Threshold Selection for UWB TOA Estimation Based on Kurtosis Analysis". *In IEEE Communications Letters*, **vol. 9, no. 12**, pp. 1025–1027, December 2005. 49

[Guv07a] Ismail Guvenc, Chia-Chin Chong, & Fujio Watanabe, "Joint TOA Estimation and Localization Technique for UWB Sensor Network Applications". *In IEEE Vehicular Technology Conference, VTC*, pp. 1574–1578, April 2007. 49, 53

[Guv07b] ———, "NLOS Identification and Mitigation for UWB Localization Systems". *In IEEE Wireless Communications and Networking Conference, WCNC*, pp. 1571–1576, March 2007. 12

[Hah04] Dirk Hahnel, Wolfram Burgard, Dieter Fox, Ken Fishkin, & Matthai Philipose, "Mapping and Localization with RFID TEchnology". *In IEEE International Conference of Robotics and Automation (ICRA 2004)*, vol. 1, pp. 1015–1020, April-May 2004. 2

[Has92] Homayoun Hashemi & David Tholl, "Analysis of the RMS delay spread of indoor radio propagation channels". *In IEEE International Conference on Communciations*, vol. 2, pp. 875 – 881, 1992. 89

[Has93a] Homayoun Hashemi, "Impulse Response Modeling of Indoor Radio Propagation Channels". *In IEEE Journal on Selected Areas in Communications*, **vol. 11, no. 7**, pp. 967–978, September 1993. 10

[Has93b] ———, "The Indoor Radio Propagation Channel". *In Proceedings of IEEE*, **vol. 81, no. 7**, pp. 943–968, July 1993. 10

[Hei06] Mohammad Heidari & Kaveh Pahlavan, "A Model for Dynamic Behavior of Ranging Errors in TOA-Based Indoor Geolocation Systems". *In IEEE Vehicular Technology Conference*, pp. 1–5, 2006. 66, 79

[Hei07a] Mohammad Heidari, Ferit Ozan Akgül, Nayef Ali Alsindi, & Kaveh Pahlavan, "Neural Network Assisted Identification of the Absence of Direct Path in Indoor Localization". *In IEEE Global Communications Conference, PIMRC*, pp. 387–392, November 2007. 89, 92, 94, 96, 98, 101, 102, 112, 113

[Hei07b] Mohammad Heidari, Ferit Ozan Akgül, & Kaveh Pahlavan, "Identification of the Absence of Direct Path in Indoor Localization Systems". *In IEEE Personal, Indoor and Mobile Radio Communications, PIMRC*, pp. 1–6, September 2007. 89, 91, 93, 94, 98, 100, 103, 104

[Hei07c] Mohammad Heidari & Kaveh Pahlavan, "A Markov Model for Dynamic Behavior of ToA-Based Ranging in Indoor Localization". *In EURASIP, European Journal on Advances in Signal Processing*, 2007. 86, 87

[Hei07d] ———, "A New Statistical Model for the Behavior of Ranging Errors in TOA-Based Indoor Localization". *In IEEE Wireless Communications and Networking Conference*, 2007. 55

[Hei08a] Mohammad Heidari, Ferit Ozan Akgül, Nayef Alsindi, & Kaveh Pahlavan, "Identification of the Absence of Direct Path in ToA-Based Indoor Localization Systems". *In International Journal of Wireless*

Information Networks - PIMRC Special Issue, 2008, submitted. 89, 91, 93, 94, 98, 100, 103, 104

[Hei08b] Mohammad Heidari, Nayef Alsindi, & Kaveh Pahlavan, "UDP Identification and Error Mitigation in ToA-Based Indoor Localization Systems using Neural Network Architecture". *In IEEE Transactions on Wireless Communications*, 2008, submitted. 89, 92, 94, 96, 98, 101, 102, 112, 113

[Hol92] Timothy J. Holt, Kaveh Pahlavan, & Jin-Fa Lee, "A Graphical Indoor Radio Channel Simulator using 2D Ray Tracing". *In IEEE Personal, Indoor, and Mobile Radio Communications, PIMRC*, pp. 411–416, October 1992. 17, 106

[How90] Steve J. Howard & Kaveh Pahlavan, "Measurement and Analysis of the indoor Radio Channel in the Frequency Domain". *In IEEE Transactions on Intrumentation and Measurement*, **vol. 39, no. 5**, pp. 751–755, October 1990. 21

[Jai01] Rahul Jain, Anuj Puri, & Raja Sengupta, "Geographical Routing using Partial Information for Wireless Ad Hoc Networks". *In IEEE Personal Communications Magazine*, **vol. 8, no. 1**, pp. 48–57, February 2001. 2

[Jen01] Patric Jensfelt, *Approaches to Mobile Robot Localization in Indoor Environments*. Ph.D. thesis, Royal Institute of Technology, Stockholm, Sweden, 2001. 2

[Jo06] Yung-Hoon Jo, Joon-Yong Lee, Dong-Heon Ha, & Shin-Hoo Kang, "Accuracy Enhancement for UWB Indoor Positioning using Ray

Tracing". *In IEEE Position, Location, and Navigation Symposium, ION*, pp. 565–568, April 2006. 56, 59, 87

[Kan06] Muzaffer Kanaan, Mohammad Heidari, Ferit Ozan Akgül, & Kaveh Pahlavan, "Technical Aspects of Localization in Indoor Wireless Networks". *In Bechtel Telecommunications Technical Journal*, **vol. 5, no. 1**, pp. 47–58, December 2006. 6, 94

[Kap96] Elliott D. Kaplan, *Understanding GPS: Principles and Applications*. 1st edn., Boston: Artech House, 1996. 1

[Kar07] Johan Karedal, Shurjeel Wyne, Peter Almers, Fredrik Tufvesson, & Andreas F. Molisch, "A Measurement-Based Statistical Model for Industrial Ultra-Wideband Channels". *In IEEE Transactions on Wireless Communications*, **vol. 6, no. 8**, pp. 3028–3037, August 2007. 50

[Ko98] Young-Bae Ko & Nitin H. Vaidya, "Location-Aided Routing (LAR) in Mobile Ad Hoc Networks". *In Proceedings of ACM/IEEE International Conference on Mobile Computing and Networking (MobiCom 1998)*, October 1998. 2

[Kri99] Prashant Krishnamurthy & Kaveh Pahlavan, "Distribution of Range Error and Radio Channel Modeling for Indoor Geolocation Applicaions". *In IEEE International Symposium on Personal Indoor and Mobile Radio Communications, PIMRC*, September 1999. 2

[Kro97] Jeffrey L. Krolik & Richard H. Anderson, "Maximum Likelihood Coordinate Registration for Over-the-Horizon Radar". *In IEEE Transactions on Signal Processing*, **vol. 45, no. 4**, pp. 945–959, April 1997. 12

[Lad04] Andrew M. Ladd, Kostas E. Berkis, Algis P. Rudys, Dan S. Wallach, & Lydia E. Kavraki, "On the Feasability of Using Wireless Ethernet for Indoor Localization". *In IEEE Transactions on Robotics and Automation*, **vol. 20, no. 3**, pp. 555–559, June 2004. 12

[LG94] Albert Leon-Garcia, *Probablity and Random Processes for Electrical Engineering*. 2nd edn., Boston: Addison Wesley, 1994. 66, 70

[Mar05] Sheri Markose & Amadeo Alentorn, "The Generalized Extreme Value (GEV) Distribution, Implied Tail Index and Option Pricing". *Economics Discussion Papers 594*, University of Essex, Department of Economics, Apr. 2005, available at http://ideas.repec.org/p/esx/essedp/594.html. 59

[McK05] Mark L. McKelvin, Mitchel L. Williams, & Nina. M. Berry, "Integrated Radio Frequency Identification and Wireless Sensor Network Architecture for Automated Inventory Management and Tracking Applications". *In Proceedings of 2005 Conference on Diversity in Computing, TAPIA*, 2005. 2

[Mol96] Andreas F. Molisch, "Statistical Properties of the RMS Delay-Spread of Mobile Radio Channels with Independent Rayleigh-Fading Paths". *In IEEE Transactions on Vehicular Technology*, **vol. 45, no. 1**, pp. 201–204, February 1996. 89

[Mol03] Andreas F. Molisch, Jeffrey R. Foerster, & Marcus Pendergrass, "Channel Models for Ultrawideband Personal Area Networks". *In IEEE Wireless Communications*, **vol. 10, no. 6**, pp. 14–21, December 2003. 4, 11, 62

[Mol05] Andreas F. Molisch, "Ultrawideband Propagation Channel-Theory, Measurement, and Modeling". *In IEEE Transactions on Vehicular Technology*, **vol. 54, no. 5**, pp. 1528–1545, September 2005. 62

[Mol06] Andreas F. Molisch, Kannan Balakrishnan, Dajana Cassioli, Chia-Chin Chong, Shahriar Emami, Andrew Fort, Johan Karedal, Juergen Kunisch, Hans Schantz, & Kazimierz Siwiak, "A Comprehensive Standardized Model for Ultrawideband Propagation Channels". *In IEEE Transactions on Antennas and Propagation*, **vol. 54, no. 11**, pp. 3151–3166, November 2006. 3, 50

[Mor07] Carlo Morelli, Monica Nicoli, Vittorio Rampa, & Umberto Spagnolini, "Hidden Markov Models for Radio Localization in Mixed LOS/NLOS Conditions". *In IEEE Transactions on Signal Processing*, **vol. 55, no. 4**, pp. 1525–1542, April 2007. 12, 56

[Mos03] Randolph L. Moses, Dushyanth Krishnamurthy, & Robert M. Patterson, "A Self-Localization Method for Wireless Sensor Networks". *In EURASIP Journal on Applied Signal Processing*, **vol. 2003, no. 4**, pp. 348–358, 2003. 3

[Ner06] Chahè Nerguizian, Charles Despins, & Sofiéne Affés, "Geolocation in Mines with an Impulse Response Fingerprinting Technique and Neural Networks". *In IEEE Transactions on Wireless Communications*, **vol. 5, no. 3**, pp. 603–611, March 2006. 14

[Pah98] Kaveh Pahlavan, Prashant Krishnamurthy, & Jacques Beneat, "Wideband Radio Propagation Modeling for Indoor Geolocation

Applications". *In IEEE Communication Magazine*, **vol. 36, no. 4**, pp. 60–65, April 1998. 2, 45, 50

[Pah00] Kaveh Pahlavan, Prashant Krishnamurthy, Ahmad Hatami, M. Ylianttila, J. Makela, R. Pichna, & J. Vallsröm, "Handoff in Hybrid Mobile Data Networks". *In IEEE Personal Communications Magazine*, **vol. 7, no. 2**, pp. 34–47, April 2000. 2

[Pah05] Kaveh Pahlavan & Allen H. Levesque, *Wireless Information Networks*. 2nd edn., New York: John Wiley & Sons, Inc., 2005. 2, 4, 17

[Pah06] Kaveh Pahlavan, Ferit Ozan Akgül, Mohammad Heidari, Ahmad Hatami, John M. Elwell, & Robert D. Tingley, "Indoor Geolocation in the Absence of Direct Path". *In IEEE Wireless Communications Magazine*, **vol. 13, no. 6**, pp. 50–58, December 2006. 3, 5, 7, 8, 10, 49, 76, 86

[Pat03] Neil Patwari, Matt Perkins Alfred O. Hero III, Neiyer S. Correal, & Robert J. O'Dea, "Relative Location Estimation in Wireless Sensor Networks". *In IEEE Transactions on Signal Processing*, **vol. 51, no. 8**, pp. 2137–2148, 2003. 3

[Poo97] H. Vincent Poor & Xiaodong Wang, "Code Aided Interference Suppression for DS-CDMA Communications - Part II: Parallel Blind Adaptive Implementations". *In IEEE Transactions of Communications*, **vol. 45, no. 9**, pp. 1112–1122, September 1997. 73

[Rap90] Theodore S. Rappaport, Scott Y. Seidel, & Rajendra Singh, "900-MHz Multipath Propagation Measurements for US Digital Cellu-

lar Radiotelephone". *In IEEE Transactions on Vehicular Technology*, **vol. 39, no. 2**, pp. 132–139, May 1990. 89

[Rap91] Theodore S. Rappaport, Scott Y. Seidel, & Koichiro Takamizawa, "Statistical Channel Impulse Response Models for Factory and Open Plan Building Radio Communication System Design". *In IEEE Transactions of Communications*, **vol. 39, no. 5**, pp. 794–807, May 1991. 10

[Roo02a] Teemu Roos, Petri Myllymaki, & Henry Tirri, "A Statistical Modeling Approach to Location Estimation". *In IEEE Transactions on Mobile Computing*, **vol. 1, no. 1**, pp. 59–69, January-March 2002. 2

[Roo02b] Teemu Roos, Petri Myllymaki, Henry Tirri, Pauli Miskangas, & Juha Sievanen, "A Probabilistic Approach to WLAN User Location Estimation". *In International Journal of Wireless Information Networks*, **vol. 9, no. 3**, pp. 155–164, July 2002. 2

[Ryd06] Mats Rydstrm, Andreu Urruela, Erik G. Strm, & Arne Svensson, "Autonomous Positioning Techniques Based on Cramr-Rao Lower Bound Analysis". *In EURASIP Journal on Applied Signal Processing*, **vol. 2006**, pp. 1–10, 2006. 3

[Sal87] Adel A. Saleh & Reinaldo A. Valenzuela, "A Statistical Model for Indoor Multipath Propagation". *In IEEE journal on Selected Areas in Communications*, **vol. 5, no. 2**, pp. 128–137, Februrary 1987. 10

[Say98] Ali H. Sayed, Alireza Tarighat, & Nima Khajehnouri, "Network-Based Wireless Location". *In IEEE Signal Processing Magazine*, **vol. 22, no. 4**, pp. 24–40, May 1998. 2

[Say03] Ali H. Sayed, *Fundamentals of Adaptive Filtering*. 1st edn., Newyork: John Wiley and Sons, 2003. 73

[Sma02] Asim Smailagic & David Kogan, "Location Sensing and Privacy in a Context-aware Computing Environment". *In IEEE Wireless Communications Magazine*, **vol. 9, no. 5**, pp. 10–17, October 2002. 2

[Tar06] Zunnoor Tarique, Wasim Q. Malik, & David J. Edwards, "Ranging in a Dense Multipath Environment Using an UWB Radio Link". *In IEE Electronic Letters*, **vol. 42, no. 2**, pp. 100–102, January 2006. 3

[Ven07] Swaroop Venkatesh & R. Michael Buehrer, "NLOS Mitigation Using Linear Programming in Ultrawideband Location-Aware Networks". *In IEEE Transactions on Vehicular Technology*, **vol. 56, no. 5**, pp. 3182–3198, September 2007. 12

[War97] Andy Ward, Alan Jones, & Andy Hopper, "A New Location Technique for the Active Office". *In IEEE Personal Communications Magazine*, **vol. 4, no. 5**, pp. 42–47, October 1997. 2

[Wer98] Jay Werb & Colin Lanzl, "Designing a Positioning System for Finding Things and People Indoors". *In IEEE Spectrum Magazine*, **vol. 35, no. 9**, pp. 71–78, September 1998. 2